

THREE DIMENSIONAL FINITE DIFFERENCE TIME DOMAIN
SIMULATIONS ON HARMONIC MOTION MICROWAVE DOPPLER
IMAGING METHOD USING REALISTIC TISSUE MODELS

A THESIS SUBMITTED TO
THE GRADUATE SCHOOL OF NATURAL AND APPLIED SCIENCES
OF
MIDDLE EAST TECHNICAL UNIVERSITY

BY

FİKRET TATAR

IN PARTIAL FULFILLMENT OF THE REQUIREMENTS
FOR
THE DEGREE OF MASTER OF SCIENCE
IN
ELECTRICAL AND ELECTRONICS ENGINEERING

SEPTEMBER 2019

Approval of the thesis:

**THREE DIMENSIONAL FINITE DIFFERENCE TIME DOMAIN
SIMULATIONS ON HARMONIC MOTION MICROWAVE DOPPLER
IMAGING METHOD USING REALISTIC TISSUE MODELS**

submitted by FİKRET TATAR in partial fulfillment of the requirements for the degree of **Master of Science in Electrical and Electronics Engineering Department, Middle East Technical University** by,

Prof. Dr. Halil Kalıpçılar
Dean, Graduate School of **Natural and Applied Sciences**

Prof. Dr. İlkay Ulusoy
Head of Department, **Electrical and Electronics Eng.**

Prof. Dr. Nevzat Güneri Gençer
Supervisor, **Electrical and Electronics Eng., METU**

Dr. Can Barış Top
Co-Supervisor, **ASELSAN Research Center, ASELSAN A.Ş.**

Examining Committee Members:

Prof. Dr. Murat Eyüboğlu
Electrical and Electronics Eng., METU

Prof. Dr. Nevzat Güneri Gençer
Electrical and Electronics Eng., METU

Prof. Dr. İlkay Ulusoy
Electrical and Electronics Eng., METU

Assoc. Prof. Dr. Yeşim Serinağaoğlu
Electrical and Electronics Eng., METU

Assist. Prof. Dr. Emine Ülkü Sarıtaş
Electrical and Electronics Eng., Bilkent University

Date: 16.09.2019

I hereby declare that all information in this document has been obtained and presented in accordance with academic rules and ethical conduct. I also declare that, as required by these rules and conduct, I have fully cited and referenced all material and results that are not original to this work.

Name, Surname: Fikret Tatar

Signature:

ABSTRACT

THREE DIMENSIONAL FINITE DIFFERENCE TIME DOMAIN SIMULATIONS ON HARMONIC MOTION MICROWAVE DOPPLER IMAGING METHOD USING REALISTIC TISSUE MODELS

Tatar, Fikret

Master of Science, Electrical and Electronics Engineering

Supervisor: Prof. Dr. Nevzat Güneri Gençer

Co-Supervisor: Dr. Can Barış Top

September 2019, 96 pages

Imaging of electromagnetic and elastic properties of the breast tissue can be used to identify cancerous regions in the dense fibro glandular breast tissue at the early stage. Numerical simulations are useful in predicting the performance of the imaging method. In Harmonic Motion Microwave Doppler Imaging Method (HMMDI), tissue is vibrated locally, microwave signals illuminate the tissue and the back scattered Doppler signal component is used to form images. In this thesis, forward problem of HMMDI method is solved with various numerical tissue models using the 3-D (Three dimensional) Finite Difference Time Domain (FDTD) method. In the forward problem solution, mechanical and electromagnetic problems are examined separately. In the mechanical problem, the acoustic radiation force of amplitude modulated focused ultrasound waves is used to produce local vibrations inside the tissue. According to mechanical simulation results, displacement values in tumor region are smaller compared to the breast tissue region as expected and increasing frequency decreases the displacement values. In electromagnetic problem, transmitter antenna sends a monochromatic signal during focused ultrasound excitation, and a receiver antenna is used to receive the amplitude and phase modulated reflected signal.

In the forward problem calculations, computation speed is an important issue since a large number of iterations (>1000) is needed in the FDTD solution. In this thesis, the forward problem is solved with parallel programming in Matlab. 19 times acceleration is achieved when GPU is employed compared to CPU case.

Using the developed simulation tools, the received HMMDI signal is analyzed using three types of breast tissue models. Firstly, tumor inside a homogenous breast tissue problem is solved. The received Doppler signal amplitude increases in the tumor region in this case. In the second type, a tumor is located inside the fibro glandular tissue. Tumor and fibro glandular tissue have the same electrical properties but their mechanical properties are different. The received Doppler amplitude decreases in tumor region, since tumor is stiffer. In the third case, a tumor in realistic breast tissue model is tested. Simulations are run with and without the tumor in the breast tissue. The results show that the Doppler signal levels change in the tumor region by 0.5 to 2 dB, compared to the case without the tumor. The difference in the Doppler signal amplitude increase with decreasing mechanical vibration frequency. In conclusion, the tumor is detectable in all cases.

Keywords: Microwave Imaging, Finite Difference Time Domain Method, Parallel Programming, Breast Cancer

ÖZ

HARMONİK HAREKETLİ MİKRODALGA DOPPLER GÖRÜNTÜLEME METODU ÜZERİNDE REALİSTİK DOKU MODELLERİ KULLANILARAK YAPILAN ÜÇ BOYUTLU ZAMANDA SONLU FARKLAR METODU SİMÜLASYONLARI

Tatar, Fikret
Yüksek Lisans, Elektrik ve Elektronik Mühendisliği
Tez Danışmanı: Prof. Dr. Nevzat Güneri Gençer
Ortak Tez Danışmanı: Dr. Can Barış Top

Eylül 2019, 96 sayfa

Meme dokusunun elektromanyetik ve elastik özelliklerinin görüntülenmesi, erken evrede yoğun fibro glandüler meme dokusunda kanserli bölgeleri tanımlamak için kullanılabilir. Sayısal simülasyonlar görüntüleme yönteminin performansını öngörmeye faydalıdır. Harmonik Hareketli Mikrodalga Doppler Görüntüleme Metodu'nda (HMMDI) doku lokal olarak titreştirilir, mikrodalga sinyalleri dokuyu aydınlatır ve geri dağılmış Doppler sinyal bileşeni görüntüleri oluşturmak için kullanılır. Bu tezde HMMDI yönteminin ileri problemi, 3-D (Üç boyutlu) Zamanda Sonlu Farklar Metodu (FDTD) kullanılarak çeşitli sayısal doku modelleriyle çözülmüştür. İleri problem çözümünde mekanik ve elektromanyetik problemler ayrı ayrı incelenmiştir. Mekanik problemde, genlik modülasyonlu odaklanmış ultrason dalgalarının akustik radyasyon kuvveti doku içinde yerel titreşimler üretmek için kullanılır. Mekanik simülasyon sonuçlarına göre tümör bölgesindeki yer değiştirme değerleri beklenildiği gibi göğüs dokusu bölgesine göre daha küçüktür ve artan frekansın yer değiştirme değerlerini azalttığı gözlemlenmiştir. Elektromanyetik problemde, odaklanmış ultrason uyarımı sırasında verici anteni monokromatik bir

sinyal gönderir ve genlik ve faz modülasyonlu yansıyan sinyali almak için bir alıcı anten kullanılır.

İleri problem hesaplamalarında, FDTD çözümünde çok sayıda tekrarlama (>1000) ihtiyaç duyulduğundan hesaplama hızı önemli bir konudur. Bu tezde ileri problem Matlab'da paralel programlama yöntemleri ile çözülmüştür. CPU kullanımına kıyasla GPU kullanıldığında 19 kat hızlanma elde edilmiştir.

Geliştirilen simülasyon araçlarını kullanarak alınan HMMDI sinyali üç tip meme dokusu modeli üzerinde analiz edildi. İlk olarak, homojen bir meme dokusundaki tümör problemi çözüldü. Alınan Doppler sinyal genliği bu durumda tümör bölgesinde artmıştır. İkinci doku tipi örneğinde fibro glandüler içindeki tümör tespit edilmeye çalışılmıştır. Tümör ve fibro glandüler doku aynı elektriksel özelliklere sahiptir ancak mekanik özellikleri farklıdır. Tümör bölgesi daha sert olduğu için alınan Doppler genliği bu bölgede azalır. Üçüncü durumda gerçekçi meme dokusu modelinde tümör tespit edilmeye çalışılmıştır. Simülasyonlar meme dokusunda tümör varken ve yokken tekrarlanmıştır. Sonuçlar Doppler sinyal seviyelerinin tümör bölgesinde tümörsüz duruma göre 0.5 ile 2 dB değiştiğini göstermektedir. Doppler sinyal genliğindeki fark mekanik titreşim frekansı azaldığında artmıştır. Sonuç olarak tüm durumlarda tümör tespit edilmiştir.

Anahtar Kelimeler: Mikrodalga Görüntüleme, Zamanda Sonlu Farklar Metodu, Paralel Programlama, Göğüs Kanseri

To my wife Sevcan and my mom

ACKNOWLEDGEMENTS

First of all, I would like to thank my thesis advisor Prof. Dr. Nevzat Güneri GENÇER for his valuable guidance, support and patience during my studies. He gave me a great chance to study in the field I want. His understanding was very important to me when I needed it most.

Special thanks to Dr. Can Barış TOP, my co-advisor, for his helps at any time. He always leads to me every time I am despaired. Thanks to his sincerity and endless support, I have completed many difficult steps. His achievements have always been wonderful examples for me.

I am also grateful to Ümit İRGİN. He is the best friend in last times of my thesis studies. We solved lots of problems together. His guidance was one of my saviors.

I would like to thank my friend and colleagues Mehmet KÜPELİ, Damla ALPTEKİN, Hüseyin YANKI, Akın DALKILIÇ, Özkan ŞAHİN for their support and advices.

I am grateful to ASELSAN A.Ş. for all facilities it offers me during my thesis studies.

This study was made possible by the grant of The Scientific and Technological Research Council of Turkey (TÜBİTAK), through the main project number 114E036. I would like to personally thank TÜBİTAK for its support on my research, as well as its continuous support for all researchers in Turkey.

My endless thanks goes to my biggest supporter, my wife Sevcan. She is my wonderful chance in my life. I would like to thank with the sincerest feelings to her endless love and support that has always inspired me.

Last but not least, my special thanks are for my parents, my sister Şeyma and my brother Erdinç. They have always been my supporter throughout of my life. I am proud of all of them.

TABLE OF CONTENTS

ABSTRACT	v
ÖZ	vii
ACKNOWLEDGEMENTS	x
TABLE OF CONTENTS	xii
LIST OF TABLES	xiv
LIST OF FIGURES.....	xv
LIST OF ABBREVIATIONS	xxi
CHAPTERS	
1. INTRODUCTION	1
1.1. Harmonic Motion Microwave Doppler Imaging Method	1
1.2. Numerical Solutions of the Forward Problem.....	3
1.3. Increasing Speed of Computation Rate	4
1.4. Scope of the Thesis.....	5
1.5. Thesis Organization.....	6
2. HMMDI WITH NUMERICAL METHODS.....	7
2.1. HMMDI Method.....	7
2.1.1. Generation of Harmonic Motion.....	8
2.1.2. Analytical Formulation for the Forward Problem of HMMDI.....	9
2.2. Mechanical FDTD	12
2.2.1. Introduction of Mechanical FDTD	12
2.2.2. Equations of Mechanical FDTD	13
2.2.3. Results of Mechanical FDTD	19

2.3. Electromagnetic FDTD	22
2.3.1. Introduction of Electromagnetic FDTD	22
2.3.2. Equations of Electromagnetic FDTD	23
2.4. Conclusion	28
3. PARALLEL PROGRAMMING USING MATLAB FOR THE HMMDI FORWARD PROBLEM	29
3.1. Introduction	29
3.2. Increasing Computation Rate with HMMDI	31
3.2.1. Vectorization	31
3.2.2. Using GPU Arrays.....	33
3.2.3. Using arrayfun Command	36
3.2.4. Effect of parfor Command	38
3.3. Conclusion	39
4. IMPLEMENTATION OF HMMDI FOR DIFFERENT BREAST MODELS	41
4.1. Tumor Inside Homogenous Fat Model	41
4.2. Tumor Inside Homogeneous Fibro Glandular Tissue in Fat	49
4.3. Tumor Inside Realistic Tissue Model	58
4.4. Conclusions.....	80
5. CONCLUSIONS AND FUTURE WORK.....	81
REFERENCES	85
6. APPENDICES.....	89
A. Equations of Electromagnetic 3-D FDTD.....	89
B. CPML Equations	93

LIST OF TABLES

TABLES

Table 2.1. Parameters of the velocity-stress relations	13
Table 2.2. Parameters of the stress-strain relationships.....	14
Table 2.3. Parameters of discrete form of the stress-strain equations	17
Table 2.4. Parameters of the intensity profile.....	18
Table 2.5. Parameters of the mechanical simulations.....	19
Table 3.1. Vectorized loop parameters	32
Table 3.2. Simulation times for vectorized and normal code	33
Table 3.3. Properties of Tesla K20 GPU card [30].....	34
Table 3.4. Comparison of vectorized code in GPU and CPU	35
Table 3.5. Comparison of arrayfun and vectroized code in CPU and GPU.....	37
Table 3.6. Final results with parfor.....	38
Table 4.1. Parameters of the homogenous simulation geometry (Figure 4.1).....	42
Table 4.2. Mechanical simulation parameters of second simulation.....	46
Table 4.3. Electrical properties of the mediums used in the simulation geometry (Figure 4.8) [10].....	50
Table 4.4. Elasticity parameters of tumor in fibro glandular tissue simulation.....	51
Table 4.5. Breast phantom types according to ACR	59
Table 6.1. Parameters of the Maxwell equations.....	89
Table 6.2. Parameters of discrete form of the 3-D FDTD equations.....	92
Table 6.3. Parameters of the CPML equations	96

LIST OF FIGURES

FIGURES

Figure 1.1. Side view of breast [2].	1
Figure 2.1. Demonstration of the Harmonic Motion Microwave Doppler Imaging Method [16].	7
Figure 2.2. Lorentz reciprocity theorem implementation of the HMMDI [10].	10
Figure 2.3. Mechanical simulation geometry for Matlab and COMSOL comparison	20
Figure 2.4. Mechanical simulation results obtained by the developed FDTD code and the COMSOL software. Figure 2.3 shows the simulation geometry. Modulation frequencies are 30 Hz and 100 Hz. Displacement values at the ultrasound focus point ($z=40$ mm) are plotted between 5 msec and 30 msec.	21
Figure 2.5. Yee grid representation [26].	23
Figure 2.6. FDTD cells with showing E_z , E_y and H_x fields on yz plane [10]. Colorful cells are special area.	25
Figure 3.1. Serial programming diagram [28]. Problem is divided into instructions which are shown as t_1 to t_N . Instructions enter the processor in series.	30
Figure 3.2. Parallel programming diagram [28]. The problem is divided into instructions which are shown as t_1 to t_N . Instructions enter the processors in parallel.	31
Figure 3.3. The difference between CPU and GPU [13]. Squares in CPU and GPU represents the cores. CPU has 2 cores but GPU has multiple cores.	33
Figure 3.4. Comparison of vectorized code in GPU and CPU. Simulation times are shown as a function of iteration number.	35
Figure 3.5. Comparison of arrayfun and vectorized code in GPU and CPU. Simulation times are shown as a function of iteration number.	37
Figure 3.6. Numerical solution procedure of the HMMDI	38

Figure 4.1. Homogenous simulation geometry [11].	42
Figure 4.2. Electromagnetic simulation results obtained by the developed FDTD code for tumor inside homogenous fat model. Figure 4.1 shows the simulation geometry. Scattered signal and Doppler component values are plotted as a function of tumor depth between 0 mm and 50 mm.	44
Figure 4.3. Simulation geometry of tumor model inside homogenous fat model. Polarization of antennas is different from Figure 4.1. The antennas are oil filled and settled into the water. 2 mm glass layer exists under the antennas. Tissue is fat and tumor is in 30 mm depth.	45
Figure 4.4. Force distribution of the transducer for tumor model in homogenous tissue model case	46
Figure 4.5. Mechanical simulation results obtained by the developed FDTD code. Figure 4.3 shows the simulation geometry. Modulation frequency is 35 Hz. Maximum displacement values at the focal point of the FUS are plotted for scan points in y direction between -16 mm and 16 mm.	47
Figure 4.6. Electromagnetic simulation results obtained by the developed FDTD code for tumor inside homogenous fat model. Figure 4.3 shows the simulation geometry. Received Doppler signal amplitude values are plotted according to the scan points in y direction between -16 mm and 16 mm.	48
Figure 4.7. Received Doppler signal amplitude as a function of the distance between the ultrasound focus and tumor center ($z=30$ mm).	49
Figure 4.8. Tumor in fibro glandular tissue simulation geometry [16].	50
Figure 4.9. Mechanical simulation results for tumor inside fibro glandular tissue in fat. Figure 4.8 shows the simulation geometry. Modulation frequency is 15 Hz. Maximum and minimum displacement values at the focal point of the FUS are plotted for scan points in y direction between -16 mm and 16 mm.	52
Figure 4.10. The received Doppler signal versus scan position in y direction. Electromagnetic simulation results when a tumor is in the fibro glandular tissue (Figure 4.8). The modulation frequency is 15 Hz.	53

Figure 4.11. Mechanical simulation results for tumor inside fibro glandular tissue in fat. Figure 4.8 shows the simulation geometry but the tumor is shifted by 4 mm in $-y$ direction. Modulation frequency is 15 Hz. Maximum and minimum displacement values at the focal point of the FUS are plotted for scan points in y direction between -16 mm and 16 mm.	54
Figure 4.12. Electromagnetic simulation results for tumor inside fibro glandular tissue in fat. Figure 4.8 shows the simulation geometry but the tumor is shifted by 4 mm in $-y$ direction. Modulation frequency is 15 Hz. Received Doppler signal amplitude values are plotted for scan points in y direction between -16 mm and 16 mm.	55
Figure 4.13. Received Doppler signal amplitude when the tumor is displaced by 4 mm in the $-y$ axis. The antennas are shifted to restore the symmetry.	56
Figure 4.14. Displacement values when the tumor is displaced by 10 mm in the $-y$ axis.	57
Figure 4.15. Electromagnetic simulation of tumor displaced by 10 mm in the $-y$ axis and antennas are shifted.	58
Figure 4.16. Realistic tissue simulation model based on Class III type of phantom data according to ACR.	59
Figure 4.17. Maximum displacement values calculated when there is no tumor in the breast model. Maximum displacement values are also calculated when there is tumor in the middle (Modulation frequency $f=15$ Hz).	60
Figure 4.18. Maximum displacement values calculated when there is no tumor in the breast model. Maximum displacement values are also calculated when there is tumor in the middle (Modulation frequency $f=20$ Hz).	61
Figure 4.19. Maximum displacement values calculated when there is no tumor in the breast model. Maximum displacement values are also calculated when there is tumor in the middle (Modulation frequency $f=30$ Hz).	62
Figure 4.20. The relative permittivity distribution in the $x=75$ mm cross section of the Class III realistic breast tissue model [20]. The portion of the model used in the	

simulations is shown in the rectangular region. Tumor is shown as dark square region in the middle. 63

Figure 4.21. The relative permittivity distribution in the $y=81.5$ mm cross section of the Class III realistic breast tissue model [20]. The portion of the model used in the simulations is shown in the rectangular region. Tumor is shown as dark square region in the middle. 64

Figure 4.22. The relative permittivity distribution in the $z=59$ mm cross section of the Class III realistic breast tissue model [20]. The portion of the model used in the simulations is shown in the rectangular region. Tumor is shown as dark square region in the middle. 65

Figure 4.23. Electromagnetic simulation results for tumor inside real breast tissue for Class III. Figure 4.16 shows the simulation geometry. Modulation frequency is 15 Hz. Received Doppler signal amplitude values are plotted for scan points in x direction between -8 mm and 8 mm. 66

Figure 4.24. Electromagnetic simulation results for tumor inside real breast tissue for Class III. Figure 4.16 shows the simulation geometry. Modulation frequency is 20 Hz. Received Doppler signal amplitude values are plotted for scan points in x direction between -8 mm and 8 mm. 66

Figure 4.25. Electromagnetic simulation results for tumor inside real breast tissue for Class III. Figure 4.16 shows the simulation geometry. Modulation frequency is 30 Hz. Received Doppler signal amplitude values are plotted for scan points in x direction between -8 mm and 8 mm. 67

Figure 4.26. Electromagnetic simulation results for tumor inside real breast tissue for Class III. Modulation frequency is 15 Hz. Tumor region is shown with arrows. Doppler signal difference between tumor is absent and tumor is present are plotted for scan points in x direction between -8 mm and 8 mm together with y direction between -8 mm and 8 mm. 68

Figure 4.27. Electromagnetic simulation results for tumor inside real breast tissue for Class III. Modulation frequency is 30 Hz. Tumor region is shown with arrows. Doppler signal difference between tumor is absent and tumor is present are plotted

for scan points in x direction between -8 mm and 8 mm together with y direction between -8 mm and 8 mm.....	68
Figure 4.28. The relative permittivity distribution in the x=54.5 mm cross section of the Class IV realistic breast tissue model [20]. The portion of the model used in the simulations is shown in the rectangular region. Tumor is shown as dark square region in the middle.	70
Figure 4.29. The relative permittivity distribution in the y=74.5 mm cross section of the Class IV realistic breast tissue model [20]. The portion of the model used in the simulations is shown in the rectangular region. Tumor is shown as dark square region in the middle.	71
Figure 4.30. The relative permittivity distribution in the z=67.5 mm cross section of the Class IV realistic breast tissue model [20]. The portion of the model used in the simulations is shown in the rectangular region. Tumor is shown as dark square region in the middle.	72
Figure 4.31. Electromagnetic simulation results for tumor inside real breast tissue for Class IV. Figure 4.16 shows the simulation geometry. Modulation frequency is 15 Hz. Received Doppler signal amplitude values are plotted for scan points in x direction between -8 mm and 8 mm.....	73
Figure 4.32. Electromagnetic simulation results for tumor inside real breast tissue for Class IV. Figure 4.16 shows the simulation geometry. Modulation frequency is 30 Hz. Received Doppler signal amplitude values are plotted for scan points in x direction between -8 mm and 8 mm.....	74
Figure 4.33. The relative permittivity distribution in the x=69.5 mm cross section of the Class II realistic breast tissue model [20]. The portion of the model used in the simulations is shown in the rectangular region. Tumor is shown as dark square region in the middle.	75
Figure 4.34. The relative permittivity distribution in the y=72.5 mm cross section of the Class II realistic breast tissue model [20]. The portion of the model used in the simulations is shown in the rectangular region. Tumor is shown as dark square region in the middle.	76

Figure 4.35. The relative permittivity distribution in the $z=75.5$ mm cross section of the Class II realistic breast tissue model [20]. The portion of the model used in the simulations is shown in the rectangular region. Tumor is shown as dark square region in the middle. 77

Figure 4.36. Electromagnetic simulation results for tumor inside real breast tissue for Class II. Figure 4.16 shows the simulation geometry. Modulation frequency is 15 Hz. Received Doppler signal amplitude values are plotted for scan points in x direction between -8 mm and 8 mm. 78

Figure 4.37. Electromagnetic simulation results for tumor inside real breast tissue for Class II. Figure 4.16 shows the simulation geometry. Modulation frequency is 30 Hz. Received Doppler signal amplitude values are plotted for scan points in x direction between -8 mm and 8 mm. 79

LIST OF ABBREVIATIONS

HMMDI	Harmonic Motion Microwave Doppler Imaging
FDTD	Finite Difference Time Domain
3-D	Three Dimensional
CPML	Convolutional Perfectly Matched Layer
FUS	Focused Ultrasound
GPU	Graphic Processing Unit
CPU	Central Processing Unit
ACR	American College of Radiology
HIFU	High Intensity Focused Ultrasound
METU	Middle East Technical University
TX	Transmitter
RX	Receiver
UWCEM	University of Wisconsin Cross-Disciplinary Electromagnetics Laboratory

CHAPTER 1

INTRODUCTION

1.1. Harmonic Motion Microwave Doppler Imaging Method

According to the research conducted in 2018, breast cancer is the second common cancer type after the lung cancer in the world [1]. Because of this reason, a large number of research studies are made for early diagnosis of breast cancer. Mammography is the first common diagnostic method applied to detect breast cancer. Mammography is a method that uses low-dose x-rays to screen the breast, however, this method has some disadvantages because of the tissues in the breast structure. Generally, breast has three kinds of tissue. These are fat, glandular (Lobules, duct) and connective tissues which are shown in Figure 1.1.

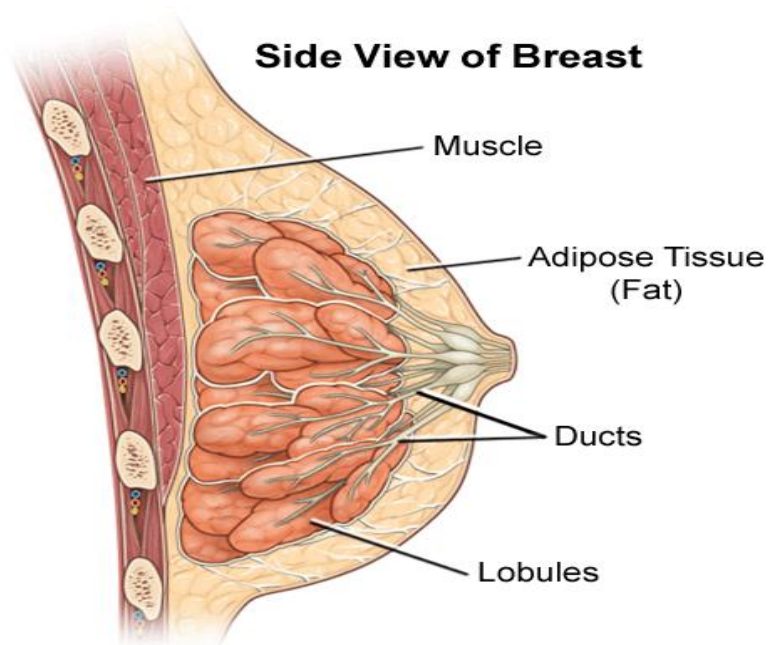


Figure 1.1. Side view of breast [2].

The difficulty for mammography is that the amount of the glandular tissue can vary for different people. When a tumor exists in the glandular tissues or lobules, it is difficult to distinguish it from the healthy tissue since tumor has low adipose content as lobules and ducts. In addition, some women with sensitive breasts may feel discomfort while mammogram device squeezes the breast. Although mammogram uses low-dose x-ray, it is not applied to pregnant women [3].

An alternative technique that is proposed to detect breast tumor is microwave imaging technique [4]. In the microwave imaging technique, a transmitter antenna transmits electromagnetic signals to the breast, then the reflected signals are collected by the receiver antennas. Reflected data contains information about electrical properties of the medium (permittivity, permeability, conductivity etc.) which identifies the materials inside [5]. This method may not exactly applicable for breast tumor detection because the electrical properties of tumor and fibro glandular is similar to each other [6].

Another alternative method for detecting tumor in the breast tissue is to apply remote palpation methods [7]. In these methods, tumor existence is decided by using mechanical properties of the tissues. Focused ultrasound which causes various displacements in the breast tissues is applied. Displacement maps are inversely proportional to the stiffness of the material. Stiffer region of tissue has less displacement than the whole region [8]. The Young's Modulus is the elasticity parameter determining the stiffness of the tissue. According to studies, the Young's modulus of tumor cells is 3-13 times bigger than the normal breast cells', so this method is a way to get information about the tumor, since it is stiffer than the fibro glandular tissue [9].

Harmonic Motion Microwave Doppler Imaging (HMMDI) method offers a combined approach that aims to use electrical and elastic properties of tissue for diagnosis [10]. In this method, the electromagnetic signal is transmitted to the tissue and the scattered signal is detected as in the microwave imaging method. At the

same time, focused ultrasound is used and a local vibration is induced on the tissue as in the remote palpation method. This vibration changes phase and amplitude of the back scattered signal. Tissue types can be distinguished according to phase and amplitude differences between the transmitted and received signals. Since both electrical and elastic parameters are involved in this method, displacement amount and dielectric properties can change the received signal characteristics [10].

Forward problem of the HMMDI method consists of these steps: Electromagnetic signal is sent via transmitter port and vibration is induced using focused ultrasound inside the tissue, finally the scattered signal is obtained from the receiver port and the data is analyzed. This thesis aims to develop improved numerical methods to efficiently solve the forward problem of the HMMDI method.

1.2. Numerical Solutions of the Forward Problem

Electromagnetic and mechanical problems are solved with numerical methods for the HMMDI forward problem. Three dimensional Finite Difference Time Domain (3-D FDTD) technique is used to get the electromagnetic solution of the forward problem. All experimental domain is simulated in the Matlab environment. 3-D domain is discretized in all directions and FDTD update equations are applied in this method. Convolutional Perfectly Matched Layer (CPML) method is applied to the update equations to diminish reflections from the numerical boundary. All layers are surrounded with CPML cells to block reflections from all dimensions. In addition, antenna ports are terminated in the simulations, since open-ended waveguides are used in the setup. The ports are terminated with the characteristic impedance of waveguides which is found analytically at the excitation frequency. A monochrome signal is applied from waveguide ports. Displacement in each cell caused by the focused ultrasound affects the electromagnetic equations. To include the effects of the displacements which are in the order of micrometers, sub-cell method is used

[11]. In this method, the FDTD update equations are altered for the cells at the focal region of the ultrasound.

Mechanical problem is also solved with the 3-D mechanical FDTD method. The same simulation domain as electromagnetic solution is used according to mechanical properties of the experimental domain. 3-D update equations are created according to stress-strain relationships. Focused ultrasound is included as a distributed force to these update equations. The velocity in each cell is calculated with these equations and displacement in each cell is calculated by using the velocity expression. This displacement data is used as an input into the electromagnetic problem. Mechanical problem is also solved in Matlab domain.

1.3. Increasing Speed of Computation Rate

One important problem about the FDTD method is the computation speed. In the FDTD method, the equations are solved iteratively and large numbers of iterations are required to obtain a better solution. The number of iterations is in the order of thousands. Both mechanical and electromagnetic solutions are produced with the 3-D update equations for the HMMDI method. Since raster scanning is used to detect the tumor, all of these computations must be repeated at each scan point. Normally for a standard scanning process, significant time on the order of hours is required to get a full numerical solution [10]. To shorten the simulation time, parallel programming techniques in Matlab are studied and applied in this thesis.

The main idea of parallel programming is to use multiple processors to complete the operation. Today's computers have multiple cores and each individual core is capable of running in parallel with the other cores. Whenever tasks are separate, each processor can work on its section independently [12]. Although the computers have multiple processors which can work at the same time, the graphic cards also can run parallel operations. These cards have many GPUs (Graphic Processing Units) which can work as a processor individually. Graphic cards can include core

numbers above a hundred, that's why parallel programming is more successful with GPUs than CPUs (Central Processing Units) [13]. In this thesis, the speed rate is increased dramatically by using parallel programming algorithm in Matlab.

1.4. Scope of the Thesis

In this thesis, the numerical solution procedure of the HMMDI forward problem is explained. Electromagnetic and mechanical analysis with several examples are presented. In addition, the numerical computation time is reduced using parallel computing methods. Solution procedures of these problems and acceleration methods are explained step by step. The scope of this thesis is outlined and listed as follows:

- Implementation of mechanical 3-D FDTD equations in Matlab,
- Validation of the mechanical simulator with COMSOL Multiphysics solutions,
- Implementation of the electromagnetic 3-D FDTD equations in Matlab,
- Applications of the CPML method to the electromagnetic 3-D FDTD equations,
- Application of the sub-cell method in the electromagnetic 3-D FDTD equations,
- Using parallel programming methods in Matlab to accelerate the numerical computations,
- Examining the feasibility of the HMMDI method with breast tissue models.

1.5. Thesis Organization

The organization of the thesis is as follows:

In Chapter 2, firstly, the solution of HMMDI method is explained in detail. Secondly, mechanical solution procedure is explained. The equations and parameters of the mechanical solution are presented. The simulation results are compared with the results obtained by a commercial software (COMSOL Multiphysics). Finally, electromagnetic solution of the forward problem is introduced. 3-D update equations with the CPML is explained in this section. In addition, sub-cell method is included and change in the update equations is explained.

In Chapter 3, the parallel programming methods are introduced. Methods with Matlab parallel programming library functions are implemented and compared to each other. Application of 3-D FDTD equations to parallel programming algorithm is defined. GPU performance is analyzed according to this algorithm.

In Chapter 4, the simulation domain of HMMDI method is introduced. Forward problem is solved by using the developed electromagnetic and mechanical numerical solvers. Breast models with different electrical and mechanical properties including tumor are examined with HMMDI method.

In Chapter 5, conclusion of the study is given together with possible future studies.

CHAPTER 2

HMMDI WITH NUMERICAL METHODS

2.1. HMMDI Method

HMMDI method has been proposed and developed by the researchers in the Bioelectromagnetism Research Group of Middle East Technical University (METU) [10], [14], [15]. The ultimate goal of the HMMDI method is to image mechanical and electrical properties of tissue. Figure 2.1 shows the basic components of the data acquisition system. In HMMDI, an electromagnetic signal is transmitted to the tissue from a transmitter antenna while focused ultrasound creates focal vibrations. The change in phase due to vibrations is detected using a receiver antenna. The change in amplitude is not significant since the vibrations are too small compared to the electromagnetic wavelength.

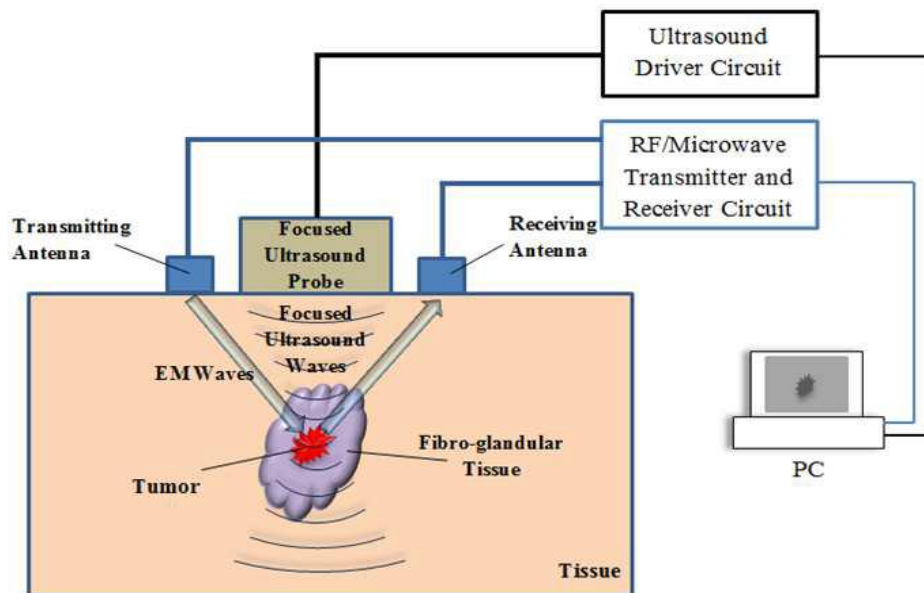


Figure 2.1. Demonstration of the Harmonic Motion Microwave Doppler Imaging Method [16].

2.1.1. Generation of Harmonic Motion

Low frequency harmonic motion is generated by a focused ultrasound transducer (FUS) driven with an amplitude modulated signal. Whenever the resulting radiation force (acoustic radiation force) is applied to the tissue, a unidirectional force affects the tissue by causing momentum transfer from acoustic signal to medium [17]. The corresponding force equation is as follows:

$$F = \frac{2\alpha I}{C_s} \quad 2-1$$

where F ($\text{kg/s}^2\text{cm}^2$) is the force per unit volume, α ($1/\text{m}$) is the absorption constant, I (W/cm^2) is the average intensity of the acoustic beam, and C_s (m/s) is the speed of ultrasound. The ultrasound transducer creates a time varying pressure at the focus point, which can be expressed as

$$P(t) = P_0 \cos(\Delta\omega/2t) \cos(\omega_u t + \phi) \quad 2-2$$

where P_0 is the amplitude of the pressure wave, $\Delta\omega/2$ is the modulation frequency and ω_u is the carrier frequency. The short-term average intensity of the beam is:

$$I = \frac{P_0^2}{4\rho C_s} (1 + \cos(\Delta\omega t)) \quad 2-3$$

where ρ is the density of the medium.

The tissue elasticity parameters Young's Modulus (E) and Poisson's ratio (ν) are related to the maximum displacement caused by the radiation force [18]:

$$E = \frac{2(1-\nu)^2 F r_b}{X_0 A} \quad 2-4$$

where r_b is the radius of the beam, A is the cross sectional area and X_0 is the maximum displacement of the tissue.

When the force is in a sinusoidal form (i.e., $F(t) = F_0 \cos(\Delta\omega t)$) the displaced local tissue can be modelled as a circular piston and the displacement of this tissue is expressed as:

$$X(t) = \frac{F_0 \cos(\Delta\omega t)}{\Delta\omega Z} = X_0 \cos(\Delta\omega t + \varphi) \quad 2-5$$

where φ is the phase change and Z is the mechanical impedance of the tissue.

2.1.2. Analytical Formulation for the Forward Problem of HMMDI

To calculate the received signal, a number of steps are implemented. Firstly, the electromagnetic forward problem is solved for a homogenous body with the tumor which has different electrical properties from the homogenous medium. Secondly, the effect of the vibration due to the focused ultrasound is analyzed. If the diameter of the tumor is much smaller than electromagnetic signal wavelength, the polarization density can be described as [19]:

$$\vec{P} = \frac{3\varepsilon_b(\varepsilon_t - \varepsilon_b)}{\varepsilon_t + 2\varepsilon_b} \varepsilon_0 \vec{E}_{inc} \quad 2-6$$

where ε_0 is free space permittivity, ε_t is relative permittivity of the tumor, ε_b is relative permittivity of the medium and \vec{E}_{inc} is the incident electric field on the tumor. The wavelength through the tissue is:

$$\lambda_b = \frac{2\pi c}{\omega \sqrt{\varepsilon_b}} \quad 2-7$$

In the forward problem, tumor is modeled with polarization current density $\vec{J} = j\omega\vec{P}$. By using the Lorentz reciprocity theorem (Equation 2-8) the received signal is calculated:

$$\int_{Tumor\ Volume} (\vec{E}_1 \cdot \vec{J}_2) dV = \int_{Waveguide\ surface} [\vec{E}_2 \cdot \vec{J}_1 - \vec{H}_2 \cdot \vec{M}_1] dS \quad 2-8$$

where \vec{J}_2 is the electric current density vector of the tumor, \vec{E}_2 is the electric field, \vec{H}_2 is the magnetic field occurred by this current density. In the reciprocal problem, \vec{E}_1 and \vec{H}_1 are the electric and magnetic fields at the receiving antenna. \vec{J}_1 is the electric current source density and \vec{M}_1 is the magnetic current source density on the waveguide surface.

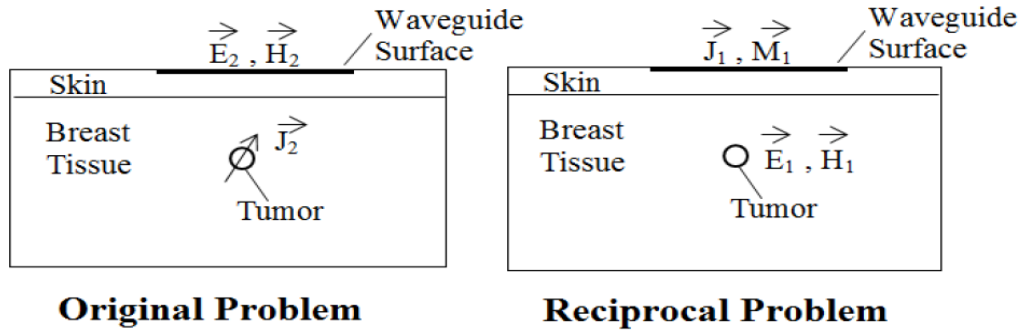


Figure 2.2. Lorentz reciprocity theorem implementation of the HMMDI [10].

To calculate the mutual admittance of the dipole and receiving antenna the Lorentz equation is multiplied with voltages of the transmitting and receiving antennas. Then the equation becomes:

$$Y_{21t} = \frac{1}{|V_1||V_2|} \int_{Tumor\ Volume} (\vec{E}_1 \cdot \vec{J}_2) dV = \frac{2}{ab} j\omega\epsilon_0 \frac{3\epsilon_b(\epsilon_t - \epsilon_b)}{\epsilon_t + 2\epsilon_b} \vec{E}_{inc} \cdot \vec{E}_1 v \quad 2-9$$

where V_1 and V_2 are the voltages of the transmitter and the receiver waveguide fields and v is the volume of the tumor.

The coupling s parameter due to tumor can be calculated from:

$$S_{21t} = -2 \frac{Y_{21t}/Y_0}{(1+Y_{11}/Y_0)^2 - Y_{21t}/Y_0^2} \quad Y_0 = \frac{1}{120\pi} \sqrt{\epsilon_w} \frac{\lambda_w}{\lambda_g} \quad 2-10$$

where ϵ_w is the relative dielectric constant of the waveguide material, λ_w is the wavelength of the same material and λ_g is the guided wavelength of the filling material.

In the HMMDI method, vibration changes phase and amplitude of the scattered signal. To analyze the vibration effect in the received signal, a continuous wave microwave signal, which can be represented as $S_{TX}(t) = A \cos(w_m t)$ is injected into the tissue from the transmitter antenna. Then, the received signal at the receiver port can be described as [10]:

$$S_{RX}(t) = B[1 + M \sin(\Delta w t)] \cos \left(w_m t + \frac{4\pi R}{\lambda} + K \sin(\Delta w t) + \phi \right) \quad 2-11$$

where B is the magnitude of the received signal without vibration, R is the distance between antennas and focal region, w_m is the frequency of the microwave signal, Δw is the vibration frequency of the tissue, M is the change in the amplitude and K is the change in the phase.

Since the displacement is in the order of micrometers, which is very small compared to the microwave wavelength, amplitude modulation parameter M is much smaller than 1, so it can be neglected. In addition, $K \ll 1$. Also, the cosine term can be expressed in the following form:

$$\begin{aligned} \cos \left(w_m t + \frac{4\pi R}{\lambda} + K \sin(\Delta w t) + \phi \right) &= \cos \left(w_m t + \frac{4\pi R}{\lambda} + \phi \right) \cdot \cos(K \sin(\Delta w t)) - \\ \sin \left(w_m t + \frac{4\pi R}{\lambda} + \phi \right) &\cdot \sin(K \sin(\Delta w t)) \end{aligned} \quad 2-12$$

$\cos(K \sin(\Delta w t)) \approx 1$ and $\sin(K \sin(\Delta w t)) = K \sin(\Delta w t)$ since $K \ll 1$

Then the cosine term becomes:

$$\cos\left(w_m t + \frac{4\pi R}{\lambda} + K\sin(\Delta w t) + \phi\right) = \cos\left(w_m t + \frac{4\pi R}{\lambda} + \phi\right) - \sin\left(w_m t + \frac{4\pi R}{\lambda} + \phi\right) \cdot K\sin(\Delta w t) \quad 2-13$$

Finally, the scattered signal can be written as:

$$S_{RX}(t) = B \left\{ \cos\left(w_m t + \frac{4\pi R}{\lambda} + \phi\right) + \frac{K}{2} \cos\left(w_m t - \Delta w t + \frac{4\pi R}{\lambda} + \phi\right) - \frac{K}{2} \cos\left(w_m t + \Delta w t + \frac{4\pi R}{\lambda} + \phi\right) \right\} \quad 2-14$$

$w_m + \Delta w$ and $w_m - \Delta w$ are the main frequency components. In addition, w_m is the other frequency component which is practically very small according to clutter and leakage. The scattered signal can be down converted and filtered according to Δw frequency since it is known.

2.2. Mechanical FDTD

2.2.1. Introduction of Mechanical FDTD

In the mechanical part of the problem, focused ultrasound is applied to the tissue in order to produce local vibrations. These local vibrations cause phase modulation in the received signal of the HMMDI system. This modulation induces a Doppler shift by an amount of harmonic motion frequency of the vibrating region. The amplitude of the tissue displacement (vibration) data is the input for the electromagnetic simulation to calculate the amplitude of the received Doppler component. In this study, the velocity stress-strain equations are solved with the FDTD method to calculate the displacement in 3-D. With the help of these equations velocity components and displacement values are calculated. These displacement values are the outputs of the mechanical simulation and inputs of the electromagnetic simulations. In the mechanical model, elastic properties are important. The amount

of displacement changes according to the tissue type, size of the medium, ultrasound intensity and frequency.

2.2.2. Equations of Mechanical FDTD

For the mechanical FDTD model, 3-D staggered grid implementation which is studied by Yamogida and Etgen [20] is used. The velocity-stress equations are as follows [21]:

$$\frac{\partial v_x}{\partial t} = \frac{1}{\rho} \left(\frac{\partial \tau_{xx}}{\partial x} + \frac{\partial \tau_{xy}}{\partial y} + \frac{\partial \tau_{xz}}{\partial z} + f_x \right) \quad 2-15$$

$$\frac{\partial v_y}{\partial t} = \frac{1}{\rho} \left(\frac{\partial \tau_{xy}}{\partial x} + \frac{\partial \tau_{yy}}{\partial y} + \frac{\partial \tau_{yz}}{\partial z} + f_y \right) \quad 2-16$$

$$\frac{\partial v_z}{\partial t} = \frac{1}{\rho} \left(\frac{\partial \tau_{xz}}{\partial x} + \frac{\partial \tau_{yz}}{\partial y} + \frac{\partial \tau_{zz}}{\partial z} + f_z \right) \quad 2-17$$

Table 2.1 presents the parameters used in the velocity-stress equations:

Table 2.1. *Parameters of the velocity-stress relations*

v_x, v_y, v_z	Velocity components
$\tau_{xx}, \tau_{xy}, \tau_{xz}, \tau_{yy}, \tau_{yz}, \tau_{zz}$	Stress components
f_x, f_y, f_z	Load components
ρ	Density of the medium

The stress-strain equations are as follows [21]:

$$\frac{\partial \tau_{xx}}{\partial t} = (\lambda + 2\mu) \frac{\partial v_x}{\partial x} + \lambda \left(\frac{\partial v_y}{\partial y} + \frac{\partial v_z}{\partial z} \right) \quad 2-18$$

$$\frac{\partial \tau_{yy}}{\partial t} = (\lambda + 2\mu) \frac{\partial v_y}{\partial y} + \lambda \left(\frac{\partial v_x}{\partial x} + \frac{\partial v_z}{\partial z} \right) \quad 2-19$$

$$\frac{\partial \tau_{zz}}{\partial t} = (\lambda + 2\mu) \frac{\partial v_z}{\partial z} + \lambda \left(\frac{\partial v_x}{\partial x} + \frac{\partial v_y}{\partial y} \right) \quad 2-20$$

$$\frac{\partial \tau_{xy}}{\partial t} = \mu \left(\frac{\partial v_x}{\partial y} + \frac{\partial v_y}{\partial x} \right) \quad 2-21$$

$$\frac{\partial \tau_{xz}}{\partial t} = \mu \left(\frac{\partial v_x}{\partial z} + \frac{\partial v_z}{\partial x} \right) \quad 2-22$$

$$\frac{\partial \tau_{yz}}{\partial t} = \mu \left(\frac{\partial v_y}{\partial z} + \frac{\partial v_z}{\partial y} \right) \quad 2-23$$

The parameters used in the stress-strain equations are given in Table 2.2.

Table 2.2. *Parameters of the stress-strain relationships*

v_x, v_y, v_z	Velocity components
$\tau_{xx}, \tau_{xy}, \tau_{xz}, \tau_{yy}, \tau_{yz}, \tau_{zz}$	Stress components
λ	First Lamè coefficient
μ	Second Lamè coefficient

These equations can be written in discrete form as follows:

$$v_{x_{i+1/2,j,k}}^{n+1/2} = v_{x_{i+1/2,j,k}}^{n-1/2} + \frac{\Delta t}{2} \left(\frac{1}{\rho_{i+1,j,k}} + \frac{1}{\rho_{i,j,k}} \right) \left(\frac{\tau_{xx_{i+1,j,k}}^n - \tau_{xx_{i,j,k}}^n}{\Delta x} + \frac{\tau_{xy_{i+1/2,j+1,k}}^n - \tau_{xy_{i+1/2,j,k}}^n}{\Delta y} + \frac{\tau_{xz_{i+1/2,j,k+1}}^n - \tau_{xz_{i+1/2,j,k}}^n}{\Delta z} + f_{x_{i+\frac{1}{2},j,k}} \cdot \right. \quad 2-24$$

stimulus)

$$v_{y_{i,j+1/2,k}}^{n+1/2} = v_{y_{i,j+1/2,k}}^{n-1/2} + \frac{\Delta t}{2} \left(\frac{1}{\rho_{i,j+1,k}} + \frac{1}{\rho_{i,j,k}} \right) \left(\frac{\tau_{xy_{i+1,j+1/2,k}}^n - \tau_{xy_{i,j+1/2,k}}^n}{\Delta x} + \frac{\tau_{yy_{i,j+1,k}}^n - \tau_{yy_{i,j,k}}^n}{\Delta y} + \frac{\tau_{yz_{i,j+1/2,k+1}}^n - \tau_{yz_{i,j+1/2,k}}^n}{\Delta z} + f_{y_{i,j+1/2,k}} \cdot \right. \quad 2-25$$

stimulus)

$$v_{z_{i,j,k+1/2}}^{n+1/2} = v_{z_{i,j,k+1/2}}^{n-1/2} + \frac{\Delta t}{2} \left(\frac{1}{\rho_{i,j,k+1}} + \frac{1}{\rho_{i,j,k}} \right) \left(\frac{\tau_{xz_{i+1,j,k+1/2}}^n - \tau_{xz_{i,j,k+1/2}}^n}{\Delta x} + \frac{\tau_{yz_{i,j+1,k+1/2}}^n - \tau_{yz_{i,j,k+1/2}}^n}{\Delta y} + \frac{\tau_{zz_{i,j,k+1}}^n - \tau_{zz_{i,j,k}}^n}{\Delta z} + f_{z_{i,j,k+1/2}} \cdot \right. \quad 2-26$$

stimulus)

$$\tau_{xx_{i,j,k}}^{n+1} = \tau_{xx_{i,j,k}}^n + \Delta t \left[\left(\lambda_{i,j,k} + 2\mu_{i,j,k} \right) \frac{v_{x_{i+\frac{1}{2},j,k}}^{n+\frac{1}{2}} - v_{x_{i-\frac{1}{2},j,k}}^{n+\frac{1}{2}}}{\Delta x} + \lambda_{i,j,k} \left(\frac{v_{y_{i,j+\frac{1}{2},k}}^{n+\frac{1}{2}} - v_{y_{i,j-\frac{1}{2},k}}^{n+\frac{1}{2}}}{\Delta y} + \frac{v_{z_{i,j,k+\frac{1}{2}}}^{n+\frac{1}{2}} - v_{z_{i,j,k-\frac{1}{2}}}^{n+\frac{1}{2}}}{\Delta z} \right) \right] \quad 2-27$$

$$\tau_{yy}^{n+1}_{i,j,k} = \tau_{yy}^n_{i,j,k} + \Delta t \left[(\lambda_{i,j,k} + 2\mu_{i,j,k}) \frac{v_{y,i,j+\frac{1}{2},k}^{n+\frac{1}{2}} - v_{y,i,j-\frac{1}{2},k}^{n+\frac{1}{2}}}{\Delta y} + \lambda_{i,j,k} \left(\frac{v_{x,i+\frac{1}{2},j,k}^{n+\frac{1}{2}} - v_{x,i-\frac{1}{2},j,k}^{n+\frac{1}{2}}}{\Delta x} + \frac{v_{z,i,j,k+\frac{1}{2}}^{n+\frac{1}{2}} - v_{z,i,j,k-\frac{1}{2}}^{n+\frac{1}{2}}}{\Delta z} \right) \right] \quad 2-28$$

$$\tau_{zz}^{n+1}_{i,j,k} = \tau_{zz}^n_{i,j,k} + \Delta t \left[(\lambda_{i,j,k} + 2\mu_{i,j,k}) \frac{v_{z,i,j,k+\frac{1}{2}}^{n+1/2} - v_{z,i,j,k-\frac{1}{2}}^{n+1/2}}{\Delta y} + \lambda_{i,j,k} \left(\frac{v_{x,i+1/2,j,k}^{n+1/2} - v_{x,i-1/2,j,k}^{n+1/2}}{\Delta x} + \frac{v_{y,i,j+1/2,k}^{n+1/2} - v_{y,i,j-1/2,k}^{n+1/2}}{\Delta y} \right) \right] \quad 2-29$$

$$\tau_{xy}^{n+1}_{i+\frac{1}{2},j+\frac{1}{2},k} = \tau_{xy}^n_{i+\frac{1}{2},j+\frac{1}{2},k} + \Delta t \left\{ \left[\frac{1}{4} \left(\frac{1}{\mu_{i,j,k}} + \frac{1}{\mu_{i+1,j,k}} + \frac{1}{\mu_{i,j+1,k}} + \frac{1}{\mu_{i+1,j+1,k}} \right) \right]^{-1} \left[\frac{v_{x,i+\frac{1}{2},j+1,k}^{n+\frac{1}{2}} - v_{x,i+\frac{1}{2},j,k}^{n+\frac{1}{2}}}{\Delta y} + \frac{v_{y,i+1,j+\frac{1}{2},k}^{n+\frac{1}{2}} - v_{y,i,j+\frac{1}{2},k}^{n+\frac{1}{2}}}{\Delta x} \right] \right\} \quad 2-30$$

$$\tau_{xz}^{n+1}_{i+1/2,j,k+1/2} = \tau_{xz}^n_{i+1/2,j,k+1/2} + \Delta t \left\{ \left[\frac{1}{4} \left(\frac{1}{\mu_{i,j,k}} + \frac{1}{\mu_{i+1,j,k}} + \frac{1}{\mu_{i,j,k+1}} + \frac{1}{\mu_{i+1,j,k+1}} \right) \right]^{-1} \left[\frac{v_{x,i+1/2,j,k+1}^{n+1/2} - v_{x,i+1/2,j,k}^{n+1/2}}{\Delta z} + \frac{v_{z,i+1,j,k+1/2}^{n+1/2} - v_{z,i,j,k+1/2}^{n+1/2}}{\Delta x} \right] \right\} \quad 2-31$$

$$\tau_{yz}^{n+1} = \tau_{yz}^n + \Delta t \left\{ \left[\frac{1}{4} \left(\frac{1}{\mu_{i,j,k}} + \frac{1}{\mu_{i,j+1,k}} + \frac{1}{\mu_{i,j,k+1}} + \frac{1}{\mu_{i,j+1,k+1}} \right) \right]^{-1} \left[\frac{v_{y_{i,j+1/2,k+1}}^{n+1/2} - v_{y_{i,j+1/2,k}}^{n+1/2}}{\Delta z} + \frac{v_{z_{i,j+1,k+1/2}}^{n+1/2} - v_{z_{i,j,k+1/2}}^{n+1/2}}{\Delta y} \right] \right\} \quad 2-32$$

The parameters used in the stress-strain discrete form equations are given in Table 2.3.

Table 2.3. Parameters of discrete form of the stress-strain equations

v_x, v_y, v_z	Velocity components
$\tau_{xx}, \tau_{xy}, \tau_{xz}, \tau_{yy}, \tau_{yz}, \tau_{zz}$	Stress components
λ	First Lamè coefficient
μ	Second Lamè coefficient
i, j, k	Numbers of subspace parts in the x, y, z planes
Δt	Change in time
n	Time parameter
$\Delta x, \Delta y, \Delta z$	Displacement in x, y, z planes
ρ	Density parameter
f_x, f_y, f_z	Load components
Stimulus	Sinusoidal source

The ultrasound transducer is assumed to emit a Gaussian beam with an intensity profile defined as follows:

$$I = \frac{I_0 A_1}{B_g} e^{-2A_1 \left(\frac{r}{a}\right)^2} e^{-2\alpha z} \quad 2-33$$

$$A_1(z) = \frac{B_g}{\frac{B_g^2 z^2}{\left(\frac{k_a a^2}{2}\right)^2} + \left(1 - \frac{z}{z_f}\right)^2} \quad 2-34$$

The parameters used in the Gaussian beam expression is given in Table 2.4.

Table 2.4. *Parameters of the intensity profile*

B_g	Gaussian coefficient
z_f	Focal length of the transducer
k_a	Acoustic wavenumber
a	Transducer radius
α	Acoustic attenuation constant
r	Distance between interested point and focal point of the ultrasound

Load components which are f_x , f_y and f_z are defined from as follows:

$$f = \frac{2\alpha I}{C_s} \quad 2-35$$

where f ($\text{kg/s}^2\text{cm}^2$) is the force per unit volume, α ($1/\text{m}$) is the absorption constant, I (W/cm^2) is the average intensity of the acoustic beam, C_s (m/s) is the speed of ultrasound.

Stimulus is taken as a sinusoidal source and it is assumed to be applied to the tissue with different frequency.

2.2.3. Results of Mechanical FDTD

Mechanical FDTD simulations are performed by using Matlab in all of the simulations for HMMDI. To be sure that the simulations works right, the same mechanical problem is solved with COMSOL Multiphysics program. Figure 2.3 shows a 80 mm x 80 mm x 80 mm cube that represents the breast tissue model. A tumor model of size 3 mm x 3 mm x 3 mm exists in the middle of the breast tissue model. The other mechanical simulation parameters are shown in Table 2.5.

Table 2.5. *Parameters of the mechanical simulations*

Speed of ultrasound in fat	1450 m/s
Focal length of the transducer	0.041 m
Frequency	3 MHz
Radius of the transducer	0.01 m
Intensity of the beam at the focus	204.6
Young's Constant in breast tissue	5 kPa
Young's Constant in tumor	20 kPa
Time step	$2.5 \cdot 10^{-6}$ s

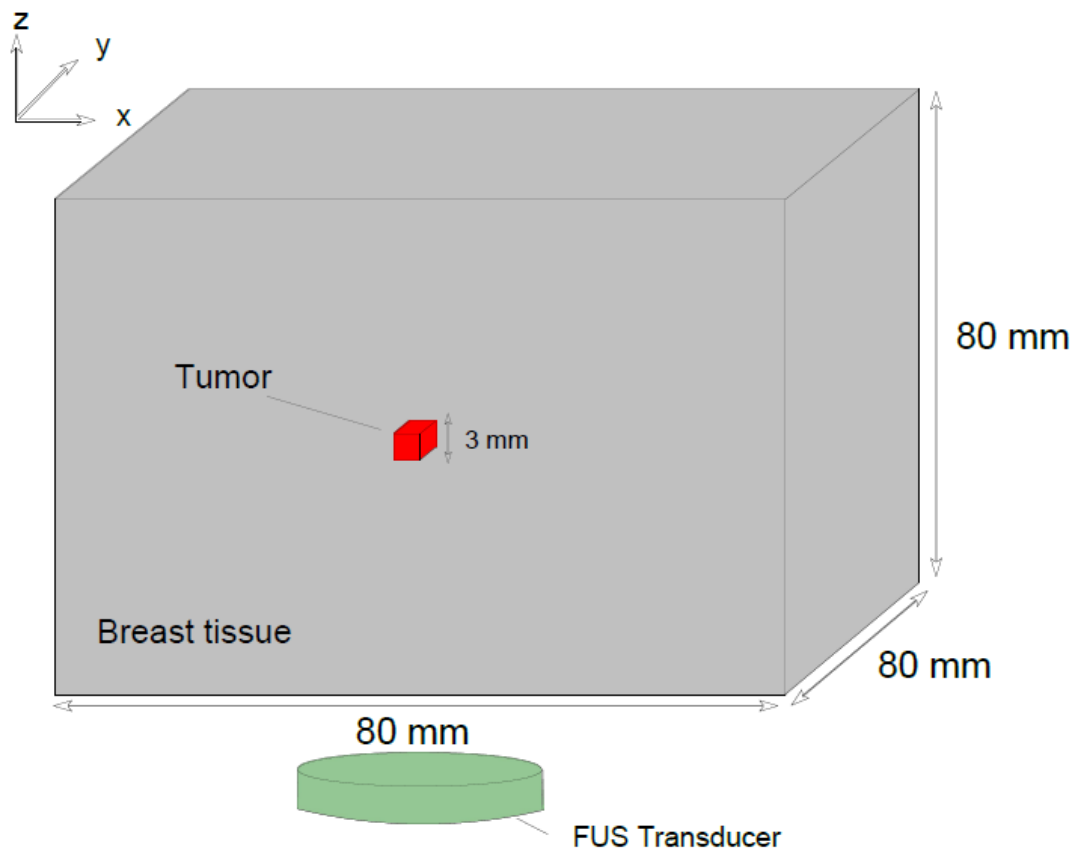


Figure 2.3. Mechanical simulation geometry for Matlab and COMSOL comparison

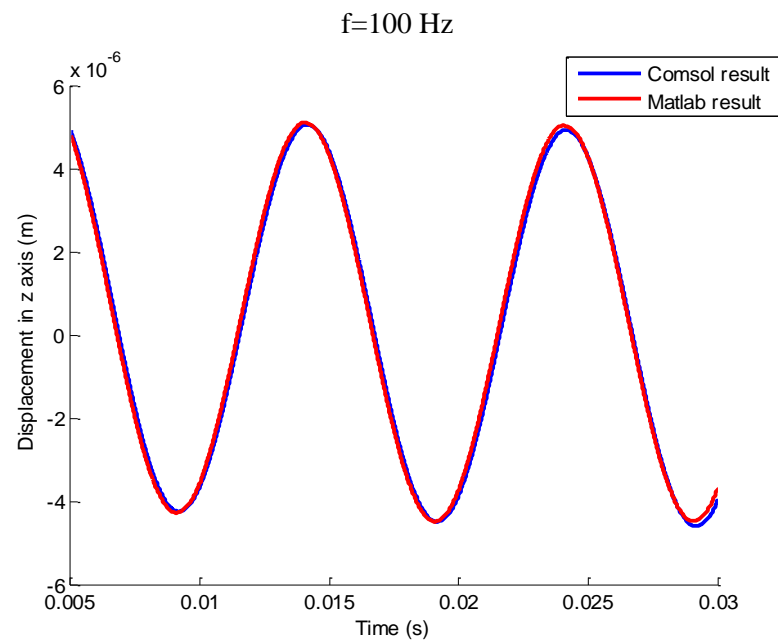
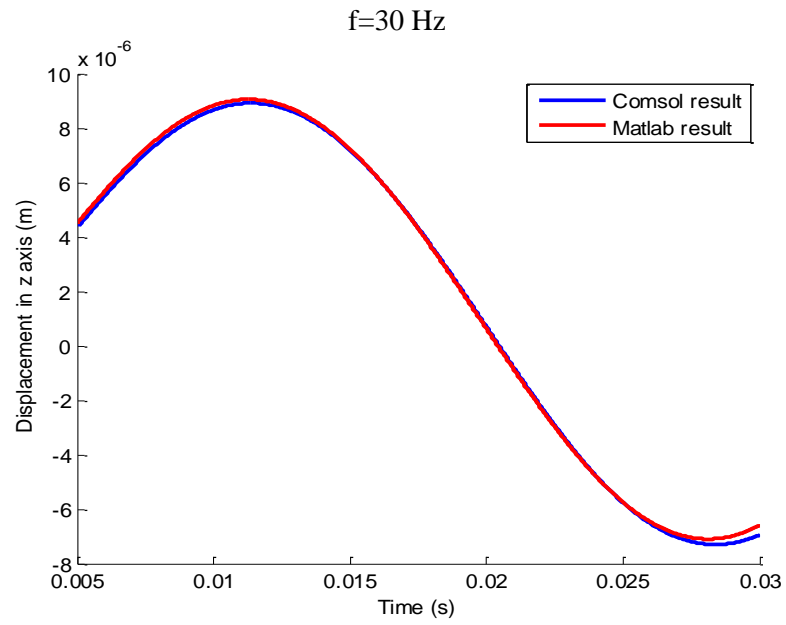


Figure 2.4. Mechanical simulation results obtained by the developed FDTD code and the COMSOL software. Figure 2.3 shows the simulation geometry. Modulation frequencies are 30 Hz and 100 Hz. Displacement values at the ultrasound focus point ($z=40$ mm) are plotted between 5 msec and 30 msec.

The modulation frequency is taken as 30 Hz in the first simulation. The displacement values in the middle of the tumor are saved and analyzed. The same simulation is performed using the developed Matlab code and COMSOL software. Figure 2.4 shows the time variation of the displacement at the ultrasound focus point obtained by using 3-D FDTD code and the COMSOL software. In the graphic, maximum values in the first period are compared. The maximum value of the Matlab result is 1.5% higher than the maximum value of the COMSOL result. The results show good agreement.

Second simulation is made with the same body and source geometry (Figure 2.3) but using a different (100 Hz) modulation frequency. In Figure 2.4, maximum values in the first period are compared. The maximum value of the Matlab result is 0.8% higher than the maximum value of the COMSOL result. The results show good agreement. In addition, increasing frequency decreases displacement values according to comparison of two results.

2.3. Electromagnetic FDTD

2.3.1. Introduction of Electromagnetic FDTD

FDTD method is one of the most preferred method for solving the electromagnetic problems. The method is easy to implement to 3-D inhomogeneous media. There are many applications of using FDTD in dielectrics, antennas, human body exposed to radiation, micro strip circuits, etc. [22]. Since the breast tissue is an inhomogeneous medium, FDTD method is a good choice to solve the forward problem of HMMDI. In addition, memory requirements of this method are less demanding compared to the other methods, like Method of Moments and Finite Element Method.

2.3.2. Equations of Electromagnetic FDTD

In FDTD method, Maxwell's equations are solved by taking the differential form of electrical and magnetic fields which are discretized in time and space. Yee grid method is used to discretize the fields in time and space for 3-D problems [23].

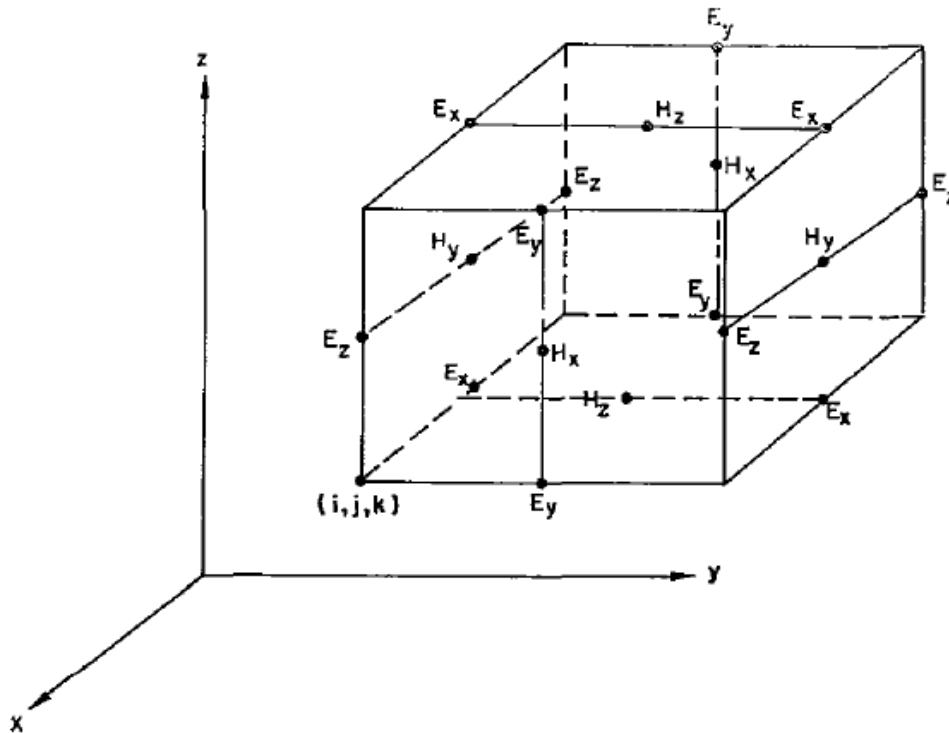


Figure 2.5. Yee grid representation [26].

In the Yee grid, at the edge centers of the cube the electric fields, at the face center of the cube the magnetic field, at the cube center the electric permittivity and conductivity and at the cube corners the magnetic permeability and magnetic loss are defined. FDTD equations are derived from Maxwell equations. Derivation of 3-D FDTD equations can be seen in Appendices A.

In the FDTD method, reflections can occur at the boundaries of the medium. Absorbing boundary conditions should be applied to prevent these reflections. These boundary conditions simulate infinite space boundaries, and therefore the reflections occur at minimum level. Perfectly matched layer method is one of the most preferable absorbing boundary condition method, since it can be used in linear, nonlinear, homogeneous, inhomogeneous and anisotropic domains [24]. To increase the absorbing effect, this method is improved by the help of recursive convolution method, stretched coordinate formulation and complex frequency shifted tensor coefficients. This method is named as Convolutional Perfectly Matched Layer (CPML) method. The biggest advantage of CPML is that the method is independent of the medium type without any modifications [25]. The equations derived in [24] can be seen in Appendices B.

In the HMMDI method, since focused ultrasound is induced inside the medium, local vibrations occur causing small displacements in the tissue cells. These displacements are very small, in the order of microns. To solve the effect of small displacements in the FDTD method, sub-cell method is introduced for thin material sheets [27]. In this method, firstly the special region which includes vibrating cells is determined. The direction of these special cells is according to ultrasound force radiating direction. In the HMMDI method, focused ultrasound radiates in the z direction, so thin sheets are settled perpendicular to z plane which is xy plane. The FDTD update equations are changed in these thin sheet regions [10].

Electric field equations are obtained from the Maxwell equations:

$$\oint \vec{H} \cdot d\vec{l} = \iint \left(\epsilon \frac{\partial \vec{E}}{\partial t} + \sigma \vec{E} \right) \cdot d\vec{S} \quad 2-36$$

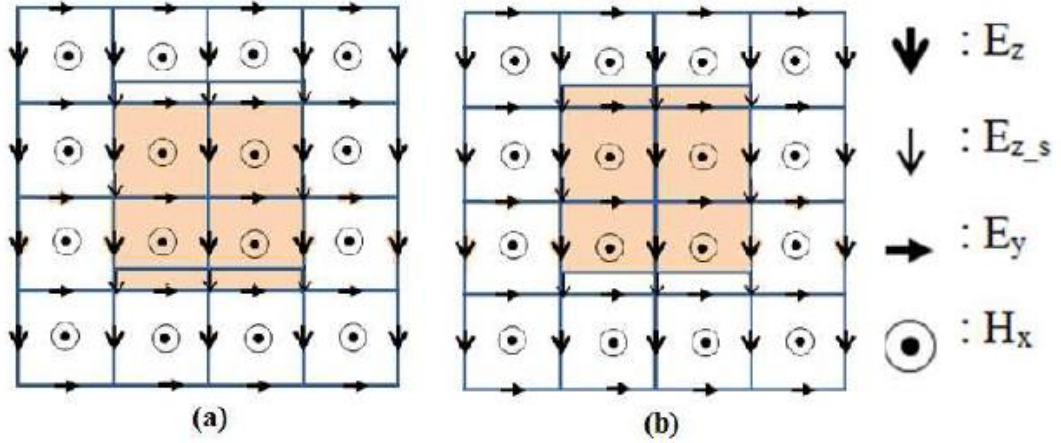


Figure 2.6. FDTD cells with showing E_z , E_y and H_x fields on yz plane [10]. Colorful cells are special area.

In equation 2-36, when left side of the Maxwell equation is solved, it is assumed that magnetic fields are constant in the related line integral, also the surface integrals in the right side of the equation are being solved by assuming that electric fields are constant in the related area of the integration. E_x update equation is changed, since some part of the neighbor of E_y fields which are H_z and H_y exists in the rectangular path surrounding the E_y node. Average media parameters are used. The equation is:

$$\begin{aligned}
 E_x^{q+1} \left[m + \frac{1}{2}, n, p \right] &= CA_d E_x^q \left[m + \frac{1}{2}, n, p \right] \\
 &+ CB_d \left\{ \frac{1}{\Delta y} \left\{ H_z^{q+\frac{1}{2}} \left[m + \frac{1}{2}, n + \frac{1}{2}, p \right] - H_z^{q+\frac{1}{2}} \left[m + \frac{1}{2}, n - \frac{1}{2}, p \right] \right\} \right. \\
 &\left. - \frac{1}{\Delta z} \left\{ H_y^{q+\frac{1}{2}} \left[m + \frac{1}{2}, n, p + \frac{1}{2} \right] - H_y^{q+\frac{1}{2}} \left[m + \frac{1}{2}, n, p - \frac{1}{2} \right] \right\} \right\}
 \end{aligned} \tag{2-37}$$

where

$$CA_d = \frac{1 - \frac{\sigma_d \Delta t}{2\epsilon_d}}{1 + \frac{\sigma_d \Delta t}{2\epsilon_d}} \quad CB_d = \frac{\frac{\Delta t}{\epsilon_d}}{1 + \frac{\sigma_d \Delta t}{2\epsilon_d}} \quad \text{and}$$

$$\sigma_d(m, n, p) = \sigma(m, n, p) \frac{\Delta z - d(m, n, p)}{\Delta z} + \frac{\sigma(m, n, p + 1)d(m, n, p)}{\Delta z}$$

$$\epsilon_d(m, n, p) = \epsilon(m, n, p) \frac{\Delta z - d(m, n, p)}{\Delta z} + \frac{\epsilon(m, n, p + 1)d(m, n, p)}{\Delta z}$$

E_y update equation is changed, since some part of the neighbor of E_y fields which are H_x and H_z exist in the rectangular path surrounding the E_y node. Average media parameters are used. The equation is:

$$\begin{aligned}
E_y^{q+1} \left[m, n + \frac{1}{2}, p \right] &= CA_d E_y^q \left[m, n + \frac{1}{2}, p \right] \\
&+ CB_d \left\{ \left\{ H_x^{q+\frac{1}{2}} \left[m, n + \frac{1}{2}, p + \frac{1}{2} \right] - H_x^{q+\frac{1}{2}} \left[m, n + \frac{1}{2}, p - \frac{1}{2} \right] \right\} \right. \\
&\left. - \left\{ H_z^{q+\frac{1}{2}} \left[m + \frac{1}{2}, n + \frac{1}{2}, p \right] - H_z^{q+\frac{1}{2}} \left[m - \frac{1}{2}, n + \frac{1}{2}, p \right] \right\} \right\}
\end{aligned} \tag{2-38}$$

E_z field is divided into two part which are E_z and E_{zs} fields since E_z field is normal to the boundary and it is not continuous. For E_z field, it is not affected from displacement so equation 6-14 in Appendices A can be used for update equation, however E_{zs} is affected from displacement. Media parameters could be calculated in a different way since the direction of displacement in -z axis. The media parameters replaced with next cell parameter exists in +z axis.

$$\begin{aligned}
E_{zs}^{q+1} \left[m, n, p - \frac{1}{2} \right] &= \frac{1 - \frac{\sigma(m, n, p + \frac{1}{2})\Delta t}{2\epsilon(m, n, p + \frac{1}{2})}}{1 + \frac{\sigma(m, n, p + \frac{1}{2})\Delta t}{2\epsilon(m, n, p + \frac{1}{2})}} E_{zs}^q \left[m, n, p - \frac{1}{2} \right] \\
&+ \frac{1}{1 + \frac{\sigma(m, n, p + \frac{1}{2})\Delta t}{2\epsilon(m, n, p + \frac{1}{2})}} \left\{ \frac{\Delta t}{\epsilon(m, n, p + \frac{1}{2})\Delta x} \left\{ H_y^{q+\frac{1}{2}} \left[m + \frac{1}{2}, n, p \right. \right. \right. \\
&\left. \left. \left. - \frac{1}{2} \right] - H_y^{q+\frac{1}{2}} \left[m - \frac{1}{2}, n, p - \frac{1}{2} \right] \right\} \right. \\
&\left. - \frac{\Delta t}{\epsilon(m, n, p + \frac{1}{2})\Delta y} \left\{ H_x^{q+\frac{1}{2}} \left[m, n + \frac{1}{2}, p - \frac{1}{2} \right] \right. \right. \\
&\left. \left. - H_x^{q+\frac{1}{2}} \left[m, n - \frac{1}{2}, p - \frac{1}{2} \right] \right\} \right\}
\end{aligned} \tag{2-39}$$

Magnetic field equations are obtained from the first Maxwell equation, which is:

$$\oint \vec{E} \cdot d\vec{l} = \iint \left(\mu \frac{\partial \vec{H}}{\partial t} \right) \cdot d\vec{S} \quad 2-40$$

H_x field equation, which is affected from displacement:

$$\begin{aligned} H_x^{q+\frac{1}{2}} \left[m, n + \frac{1}{2}, p + \frac{1}{2} \right] &= \frac{1 - \frac{\sigma \Delta t}{2\mu}}{1 + \frac{\sigma \Delta t}{2\mu}} H_x^{q-\frac{1}{2}} \left[m, n + \frac{1}{2}, p + \frac{1}{2} \right] \\ &+ \frac{1}{1 + \frac{\sigma \Delta t}{2\mu}} \left\{ \frac{\Delta t}{\mu \Delta z} \left\{ E_y^q \left[m, n + \frac{1}{2}, p + 1 \right] - E_y^q \left[m, n + \frac{1}{2}, p \right] \right\} \right. \\ &- \frac{\Delta t}{\mu \Delta y} \frac{\Delta z - d}{\Delta z} \left\{ E_z^q \left[m, n + 1, p + \frac{1}{2} \right] - E_z^q \left[m, n, p + \frac{1}{2} \right] \right\} \\ &\left. - \frac{d}{\Delta z} \frac{\Delta t}{\mu \Delta y} \left\{ E_{zs}^q \left[m, n + 1, p + \frac{1}{2} \right] - E_{zs}^q \left[m, n, p + \frac{1}{2} \right] \right\} \right\} \end{aligned} \quad 2-41$$

Displacement also affects the H_y field equation:

$$\begin{aligned} H_y^{q+\frac{1}{2}} \left[m + \frac{1}{2}, n, p + \frac{1}{2} \right] &= \frac{1 - \frac{\sigma \Delta t}{2\mu}}{1 + \frac{\sigma \Delta t}{2\mu}} H_y^{q-\frac{1}{2}} \left[m + \frac{1}{2}, n, p + \frac{1}{2} \right] \\ &+ \frac{1}{1 + \frac{\sigma \Delta t}{2\mu}} \left\{ \frac{\Delta t}{\mu \Delta x} \frac{\Delta z - d}{\Delta z} \left\{ E_z^q \left[m + 1, n, p + \frac{1}{2} \right] \right. \right. \\ &- E_z^q \left[m, n, p + \frac{1}{2} \right] \left. \right\} \\ &- \frac{\Delta t}{\mu \Delta z} \left\{ E_x^q \left[m + \frac{1}{2}, n, p + 1 \right] - E_x^q \left[m + \frac{1}{2}, n, p \right] \right\} \\ &\left. - \frac{d}{\Delta z} \frac{\Delta t}{\mu \Delta x} \left\{ E_{zs}^q \left[m, n, p + \frac{1}{2} \right] - E_{zs}^q \left[m + 1, n, p + \frac{1}{2} \right] \right\} \right\} \end{aligned} \quad 2-42$$

Since permeability is the same in everywhere, H_z field is not affected from the displacement, so equation 6-11 in Appendices A can be used for update equation.

2.4. Conclusion

In this chapter, the HMMDI method is introduced, and harmonic motion generation of the HMMDI method is explained. Amplitude modulated signal is applied from the focused ultrasound transducer that causes radiation force on the tissue. The effect of this radiation force is analyzed. Then, the problem is modelled analytically. The numerical problem is solved in two stages. Firstly, forward problem is solved for a homogenous body with tumor, then vibration effect is included and the problem is solved again. In the solution procedure reciprocity theorem is used and effect of vibration is included in the equations.

Secondly, mechanical FDTD solutions are described. Mechanical 3-D FDTD equations are extracted by using stress-strain relationships. Then, a simulation domain is created and mechanical equations are studied in Matlab. In addition, same problem is solved with COMSOL Multiphysics. The simulation results are in good agreement, which shows Matlab program works well. According to the results, displacement values decrease in the tumor region, since tumor is stiffer than breast tissue. The results of the simulations repeated for different frequencies show that the displacement values decrease with increasing frequency.

Finally, electromagnetic 3-D FDTD equations are presented. The equations are empowered with CPML and sub-cell methods. To prevent reflection at the boundaries, CPML method is implemented to 3-D FDTD update equations. Furthermore, to observe the effect of vibrations on the received signal, sub-cell method is used. This method solved the effect of small displacement in FDTD method.

CHAPTER 3

PARALLEL PROGRAMMING USING MATLAB FOR THE HMMDI FORWARD PROBLEM

3.1. Introduction

As mentioned in the previous chapters, the HMMDI simulations are implemented with the 3-D FDTD methods for both mechanical and electromagnetic problems. One important problem about the 3-D FDTD solutions is the computation speed since the solutions are obtained iteratively. A number of iterations are made to obtain a solution for only one scanning point. If the number of scanning points increases, thousands of iterations are required yielding a computation time on the order of hours. This section presents methods employed in this thesis study to decrease the computation time.

One of the most important factors in computation acceleration is the hardware performance. Commonly, processors determine this performance. Multi-core processors can be used in parallel to provide a higher speed. Also, some additional hardware except processors play an important role in computation acceleration. The structure of the programming should also be focused on getting maximum efficiency with the available hardware. Programming types are important for this issue. There are two basic programming types, namely, serial and parallel programming [28]. By combining these two basic types of programming, the code can be processed as desired.

In serial programming;

- The problem should be divided into processes that can be solved in series.
- These operations are resolved in succession.

- All transactions are solved on a single processor.
- Only one process can be solved at a time.

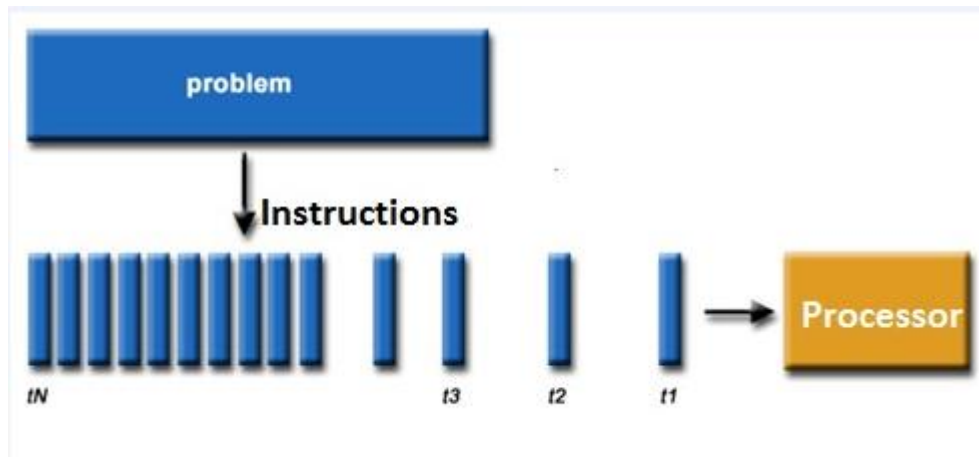


Figure 3.1. Serial programming diagram [28]. Problem is divided into instructions which are shown as t_1 to t_N . Instructions enter the processor in series.

In the simplest sense, parallel programming is the solution of numerical problem using multiple processing resources at the same time. In parallel programming:

- The problem is divided into separate sections so that it can be solved at the same time.
- Each section is divided into series operations.
- These processes are analyzed simultaneously on different processors [28].

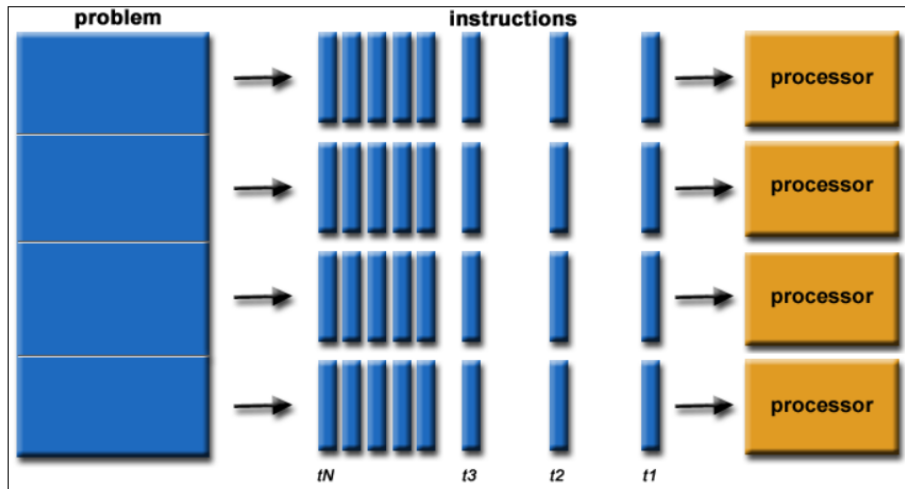


Figure 3.2. Parallel programming diagram [28]. The problem is divided into instructions which are shown as t_1 to t_N . Instructions enter the processors in parallel.

Parallel programming is usually done by 2 different hardware which are multi-core/processor computer and a network of computers. A network of computers is an expensive solution, so it is not used. Multi-processor computers can be used but in addition to multi-processors, there are graphic processing units (GPU) that can be used for parallelization. In the HMMDI simulations, multi-processor computers with GPU is preferred.

3.2. Increasing Computation Rate with HMMDI

To perform the best computation rate, three methods are studied to implement the codes in Matlab domain.

3.2.1. Vectorization

To improve computation speed rate for 3-D FDTD solutions, the first basic method is vectorization. Vectorization is used in Matlab. In general, vectorization methods are the factors that facilitate the writing and processing of a code. According to Matlab, the benefits of vectorization are as follows:

- Appearance: Vectorized mathematical codes are like mathematical expressions found in books. This view makes code very easy to understand.
- Less failure rate: Vectorized codes without loops are shorter. Fewer lines of code have a smaller error rate.
- Performance: Vectorized codes generally run faster than codes with loops [29].

As an example for vectorized code, one of the loop in the HMMDI electromagnetic code is used. The normal code is:

```

for k = 1:Kmax-1
for i = 1:Imax-1
for j = 1:Jmax-1
Hx(i,j,k) = DA * Hx(i,j,k) + DB * ( (Ez(i,j,k) - Ez(i,j+1,k))*den_hy(j)+(Ey(i,j,k+1) - Ey(i,j,k))*den_hz(k));
end
end
end

```

And the vectorized code is:

```

Hx(1:Imax-1,1:Jmax-1,1:Kmax-1)=DA*Hx(1:Imax-1,1:Jmax-1,1:Kmax-1) + DB*(-diff(Ez(1:Imax-1,1:Jmax,1:Kmax-1),1,2).*den_hy(1:Imax-1,1:Jmax-1,1:Kmax-1) + (diff(Ey(1:Imax-1,1:Jmax-1,1:Kmax),1,3).*den_hz(1:Imax-1,1:Jmax-1,1:Kmax-1)));

```

Table 3.1. *Vectorized loop parameters*

Ey	Electric field in y axis
Hx	Magnetic field in x axis
Ez	Electric field in z axis
Imax, Jmax, Kmax	Maximum grid numbers in x, y, z axis
Diff	Matlab function calculating vector difference

As seen in the above example, the code is shorter and easier to understand. In order to analyze the performance, which is more important for HMMDI, homogenous simulation geometry is used. The size of the geometry is 80 mm x 80 mm x 80 mm

and cell size is 1 mm. Based on the FDTD iteration loop, the simulation times are compared. Simulations are run on ASUS laptop which has Intel Core i7-4700HQ CPU @ 2.4 GHz (8 CPUs) processor and 16 GB RAM. The simulation is made for normal code and vectorized code. The results are shown in Table 3.2.

Table 3.2. *Simulation times for vectorized and normal code*

Iteration Number	Normal Code (s)	Vectorized Code (s)
100	262.4	32.4
1000	2526.5	325.5

According to result, vectorized code is approximately 8 times faster than normal code for ASUS laptop. It approves the benefit of vectorization. Furthermore, simulations without GPU will be studied on ASUS Laptop.

3.2.2. Using GPU Arrays

GPU (Graphic Processing Unit) together with CPU (Central Processing Unit) can be used to accelerate the applications in a number of areas, like scientific, engineering, analytics. Normally CPU consists of a few cores which are used in general serial process applications, while GPU has thousands of smaller, more efficient cores designed for simultaneous multiple operations [13].

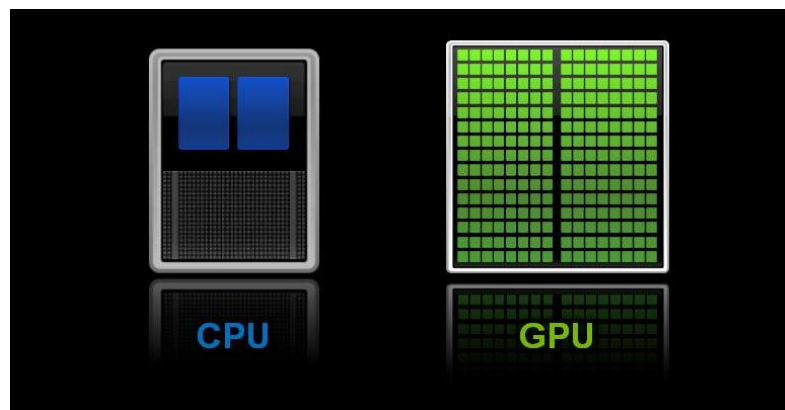


Figure 3.3. The difference between CPU and GPU [13]. Squares in CPU and GPU represents the cores. CPU has 2 cores but GPU has multiple cores.

GPU can be an efficient tool for parallel programming which satisfies higher computation speed rate. The easiest way to use GPU in Matlab is applying *gpuArray* command. *gpuArray* command stores the array in GPU domain. Normally, the defined arrays are placed in CPU domain, whenever this command is used, arrays are transferred from the CPU to GPU domain. If all arrays in the computation loop are transferred to the GPU domain, it increases the computation speed. At the end of the computation, the arrays in the GPU should be transferred to the CPU domain. It takes a few times, in the order seconds. The same example in the previous section is solved in the GPU. All arrays in the loop are transferred from the CPU to GPU domain in the vectorized code. GPU simulation is done in HP Z820 workstation. HP Z820 workstation has Intel Xeon CPU E5-2620 v2 @ 2.1 GHz (24 CPUs) processor and 64 GB RAM. This workstation has also Tesla K20 GPU card [30]. Some properties of Tesla K20 GPU card are shown in Table 3.3.

Table 3.3. *Properties of Tesla K20 GPU card [30].*

Number of CUDA cores	2496
Size	5 GB
Clock Rate	706 KHz
Bandwidth	208 GBps

Table 3.4 shows the simulation times for the simulations performed in GPU and CPU for vectorized code. It is seen that simulation in GPU is approximately 3.5 times faster than simulation in CPU for Matlab. Just only using *gpuArray* command makes big effect on the computation speed for Matlab. It shows the efficiency of using GPU.

Table 3.4. Comparison of vectorized code in GPU and CPU

Iteration number	Vectorized Code in GPU (s)	Vectorized Code in CPU (s)
100	10.4	32.42
1000	88.08	325.57
3000	261.28	950.27
5000	430.3	1509.7

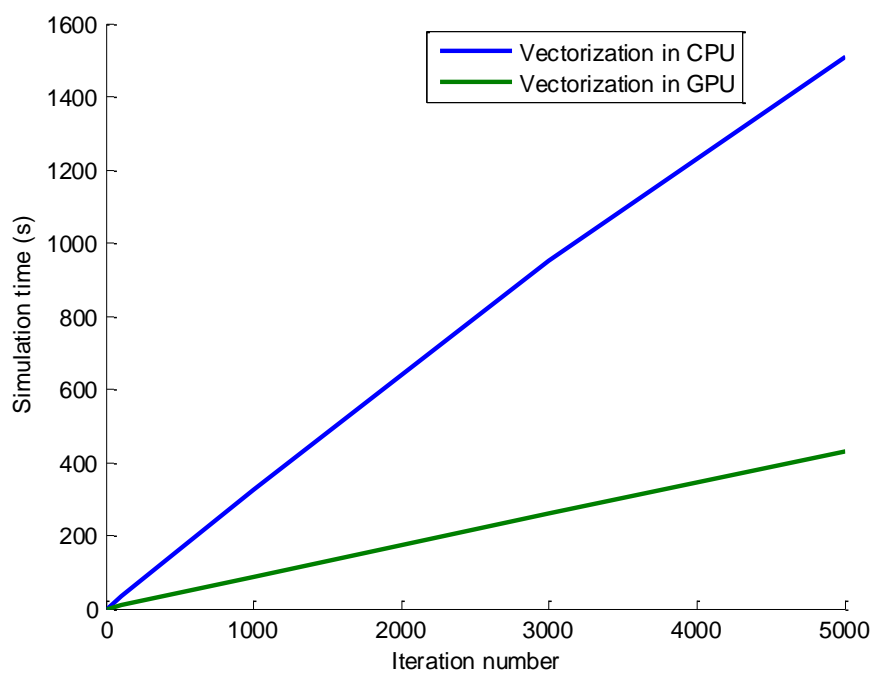


Figure 3.4. Comparison of vectorized code in GPU and CPU. Simulation times are shown as a function of iteration number.

3.2.3. Using `arrayfun` Command

To improve the GPU effect in the computation speed with Matlab, `arrayfun` command is the best alternative. The general definition of this command is as follows: `[A B ...]=arrayfun(FUN,C,D,...)`. This command applies a function represented as FUN to each element of the intended C and D arrays [31]. The resulting arrays are C and D. The important point here is that all inputs must have the same size or should be a scalar input. This command is a convenient option for parallelization because it takes the task of sending elements of the input arrays in a certain order. In addition, if the input arrays are defined in the GPU and the `arrayfun` command is used, FUN function can be applied by different GPU processors. The biggest problem using this command is the size of the inputs which must be the same. In the computational loops of the HMMDI simulations, a number of arrays are used with different array sizes. To benefit the advantages of `arrayfun`, their sizes should be arranged. All arrays in the loop need to reach the maximum dimensional array size in the loop. It is also necessary to shape these matrices in the order they are used in the loop. `arrayfun` command takes entries from matrices in a certain order that cannot be changed, therefore matrices are formed according to the loop structure of the equation and `arrayfun` gets the input in the order required. To reshape the matrices according to desired order, `repmat` command is used. This command copies an array in the desired direction so the array can be used many times in `arrayfun`. The same simulation geometry is solved with `arrayfun`. The simulation results are shown in Table 3.5. This time, both simulations run in GPU domain and the effects of `arrayfun` are observed. `arrayfun` can run the code approximately 2 times faster than the vectorized code in GPU for Matlab. In addition, `arrayfun` solution is 8 times faster than the solution in the CPU domain for Matlab. It is a good improvement for the computation speed.

Table 3.5. Comparison of arrayfun and vectorized code in CPU and GPU.

Iteration number	Vectorized Code in CPU (s)	Vectorized Code in GPU (s)	arrayfun (s)
100	32.42	10.4	10.4
1000	325.57	88.08	51.9
3000	950.27	261.28	140.2
5000	1509.7	430.3	231.6

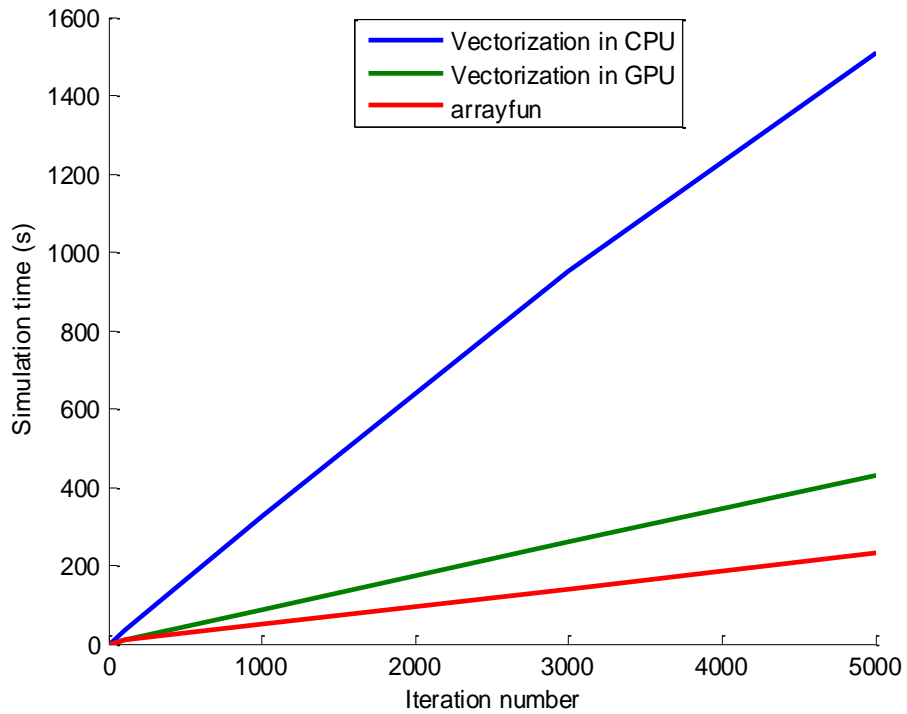


Figure 3.5. Comparison of arrayfun and vectorized code in GPU and CPU. Simulation times are shown as a function of iteration number.

3.2.4. Effect of parfor Command

By the help of *arrayfun*, great improvement in the computation speed is provided but there is still a problem about using the full capacity of Tesla K20. It is a powerful card which has 2496 CUDA cores and 5 GB memory. To use this card more efficiently, a method is advised with the *parfor* command. This command can run more than one function at the same time in Matlab. In HMMDI, lots of scan points should be analyzed to generate imaging data. By using the *parfor* command, same function can be performed for different scan points. This means that the HMMDI electromagnetic solution function solves more than one scan point at the same time. HP Z820 workstation also contains one more GPU card which is Quadro K600. It is not a powerful GPU card but it can be used as an auxiliary worker since lots of point are solved at the same time.

Table 3.6. Final results with *parfor*

Simulation type	1 point scanning	17 points scanning
<i>parfor</i> with <i>arrayfun</i> in GPU	-	1.1 hour
Vectorization in CPU	1.2 hour	20.4 hour

In HMMDI, the solution procedure of electromagnetic FDTD is as shown in Figure 3.6.

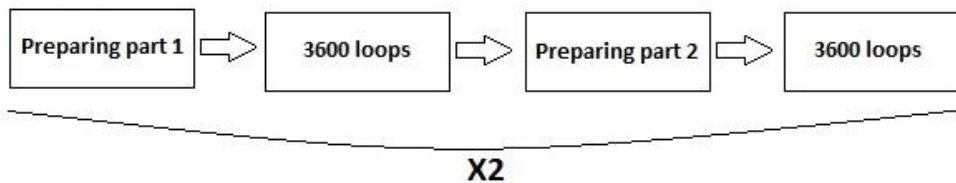


Figure 3.6. Numerical solution procedure of the HMMDI

In the preparation parts, the definition of the variables used in the loops are introduced, consequently, the time required for this process is short, in the order of

seconds. In the HMMDI solution, 4 preparing parts exist, therefore the time used for these parts is not very important. In the Figure 3.6, totally 7200 loops exist and these loops repeat two times. For the simulation of each scanning point, 14400 loops are used. Generally, 17 points scanning is run in the HMMDI examples. According to the results shown in Table 3.6, 17 points scanning by using *parfor* is completed in 1.1 hours, however 1 point scan with the vectorization method in CPU 1.2 hour. To conclude, approximately 19 times acceleration is achieved by using GPU in Matlab.

3.3. Conclusion

In this chapter, simulation time of the HMMDI forward problem is analyzed. Some acceleration techniques are implemented using Matlab functions and the parallel processing toolbox. First technique is vectorization and it can be implemented in the CPU domain. It is shown that it is a good alternative to accelerate the computation without GPU. Secondly, GPU is introduced. GPU has small cores which has capability of doing computations parallel. By using the Matlab library, effective acceleration is achieved. The easiest way is to carry all domains from CPU to GPU by the help of *gpuArray* command. In addition, the acceleration approached higher levels by using the *arrayfun* command. Finally, since in the HMMDI project there is Tesla K20 GPU card, which is very powerful, many scanning points are solved at the same time by using the *parfor* command. It gives an acceleration about 19 times in the Matlab domain.

CHAPTER 4

IMPLEMENTATION OF HMMDI FOR DIFFERENT BREAST MODELS

HMMDI method is studied for different types of breast models: *i*) Homogenous fat model, *ii*) homogeneous fibro-glandular inside fat model, and *iii*) realistic tissue model. For each breast model, mechanical and electromagnetic simulations are run and the resultant data are analyzed. Parallel programming algorithm is used in all electromagnetic simulations.

4.1. Tumor Inside Homogenous Fat Model

To observe the results of the HMMDI method, firstly homogenous simulation geometry (Figure 4.1) is created. TX and RX antennas are water filled ($\epsilon_{rwater} = 77.15$ $\sigma_{water} = 4.41 S/m$). Under the antennas, there is a 2 mm skin layer, and under the skin layer there is homogenous fat tissue model. A tumor model with the size of 3 mm \times 3 mm \times 3 mm is defined in the middle of the tissue model. All electrical properties of the mediums are shown in the figure. CPML boundaries are added to the geometry with a layer thickness of 10 mm at each face to prevent reflections from the boundaries in the simulation. In this simulation, the tumor depth is changed and scattered and Doppler component of the signal are analyzed. Simulation parameters are shown in Table 4.1.

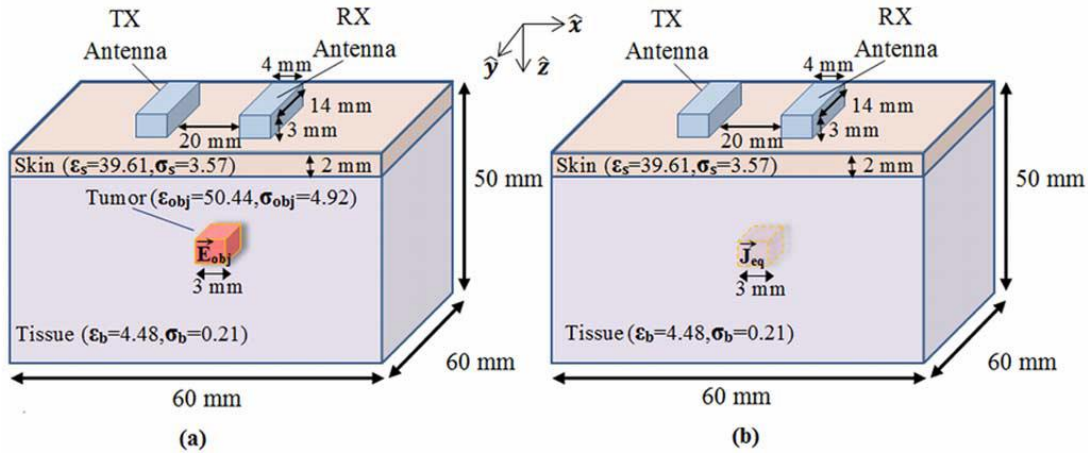


Figure 4.1. Homogenous simulation geometry [11].

Table 4.1. Parameters of the homogenous simulation geometry (Figure 4.1).

Frequency	5 GHz
Size of each cell in x, y, z axis	1 mm
Time step	$1.1050 \cdot 10^{-12}$ s
Number of iterations	3600
Maximum displacement	$10 \cdot 10^{-6}$ m

In electromagnetic simulations, two simulations are made to find the Doppler component of the signal. In the first simulation, the tumor is at its original position (minimum displacement=0 micron). The electric fields in the tumor region is stored at each iteration while the transmitter antenna is radiating. In the second simulation, the targeted area is replaced by its volume equivalent electric current distribution according to *volume equivalence principle*. TX antenna is not radiating since volume equivalent source is used. The volume equivalent current can be calculated from:

$$\vec{J}_{eq} = (\epsilon_{obj} - \epsilon_b) \frac{d\vec{E}_{obj}}{dt} + (\sigma_{obj} - \sigma_b) \vec{E}_{obj} \quad 4-1$$

where \vec{J}_{eq} is the volume equivalent electric current density distribution, ϵ_{obj} and ϵ_b are the permittivity of the tumor and the background tissue, σ_{obj} and σ_b are the

conductivity of the tumor and the background tissue and \vec{E}_{obj} is the stored electric field. The frequency domain signal at RX antenna obtained after the second simulation is divided with the signal transmitted from the TX antenna at the first simulation:

$$S_{RX_main} = \frac{|E_{t2_mindisp}|}{|E_{t1_mindisp}|} \quad 4-2$$

where S_{RX_main} is the amplitude of the main frequency component, $E_{t2_mindisp}$ is the total electric field at the RX antenna for the minimum displaced tissue simulation, $E_{t1_mindisp}$ is total electric field at the TX antenna for the minimum displaced tissue simulation.

To calculate the Doppler component, the same simulations are run for the maximum displacement case. The phase difference between RX signal in the maximum displaced simulation and RX signal in the minimum displaced simulation is calculated. Phase difference is calculated in the frequency domain, so Discrete Time Fourier Transform is used. The Doppler component is calculated with the following formula:

$$S_{RX_Doppler} = \frac{|E_{s2_mindisp}|}{|E_{t1_mindisp}|} \left(\frac{Arg(E_{s2_maxdisp}) - Arg(E_{s2_mindisp})}{2} \right) \quad 4-3$$

where $E_{s2_mindisp}$ is the scattered electric field at the RX port in the minimum displaced simulation, $E_{t1_mindisp}$ is the transmitted signal applied from TX port in the minimum displaced simulation. $Arg(E_{s2_maxdisp}) - Arg(E_{s2_mindisp})$ is the phase difference between the scattered signal at the RX port in the maximum displacement simulation and scattered signal at the RX port in the minimum displacement simulation.

For this simulation, the maximum displacement is assumed to be 10 microns in the tumor region and the minimum displacement is assumed zero in the same region. The results are shown in Figure 4.2. The results are validated with results reported in

[11]. It is observed that, the pattern is the same and a maximum of 5 dB difference exists between the two results.

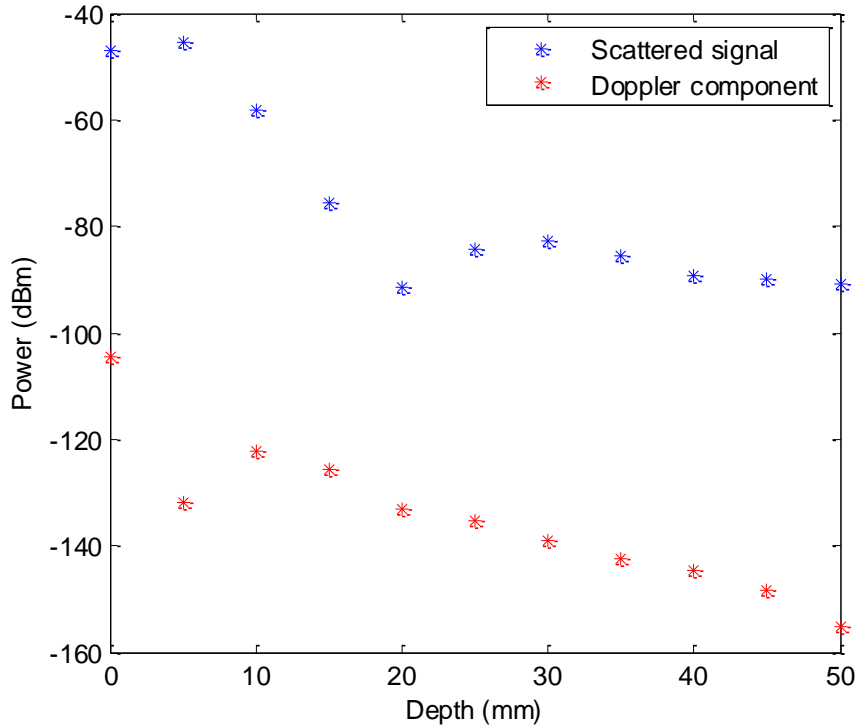


Figure 4.2. Electromagnetic simulation results obtained by the developed FDTD code for tumor inside homogenous fat model. Figure 4.1 shows the simulation geometry. Scattered signal and Doppler component values are plotted as a function of tumor depth between 0 mm and 50 mm.

In the second simulation, the simulation geometry is changed. The antennas are assumed to be oil filled and their polarizations are changed. Also, both antennas are settled into the water. Under the antennas, a 2 mm glass layer exists. Tissue is selected as fat model under the glass. Finally, there is a tumor model in 30 mm depth according to the antennas' bottom surface. Size of the tumor model is 3 mm × 3 mm × 3 mm. FUS Transducer is at the bottom of the simulation domain. 10 cells of CPML region exists in three dimensions. The simulation geometry is shown in Figure 4.3.

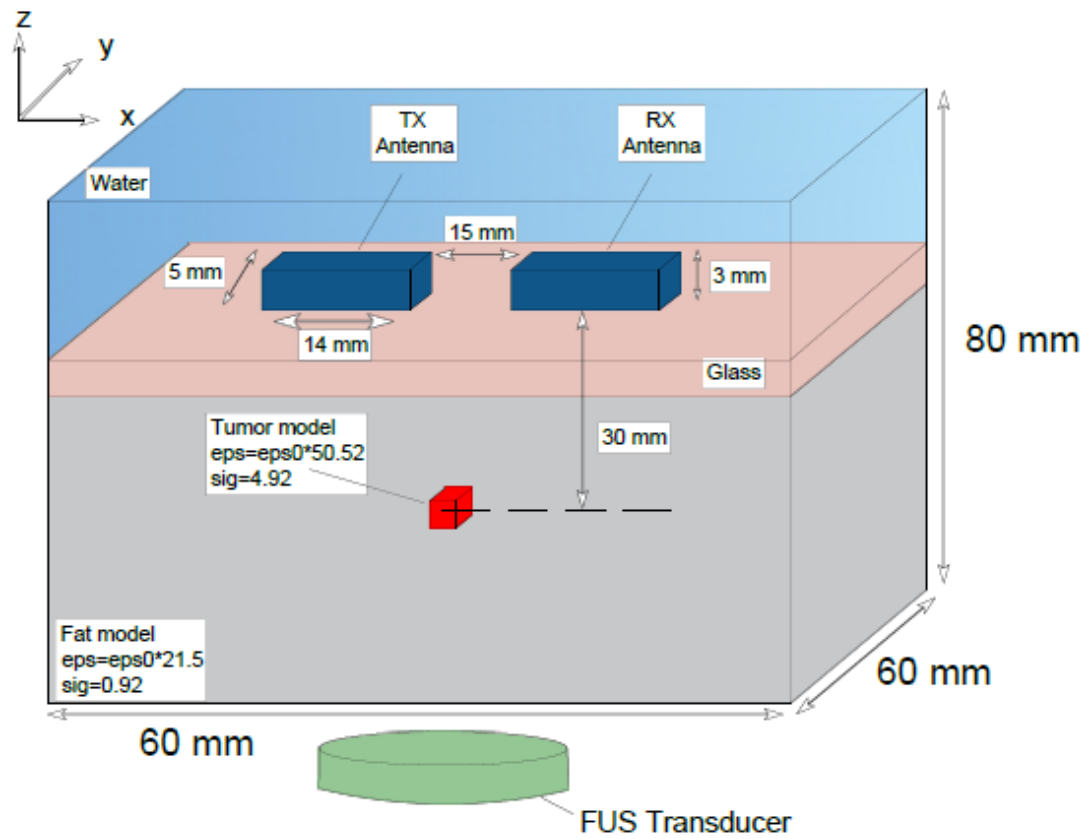


Figure 4.3. Simulation geometry of tumor model inside homogenous fat model. Polarization of antennas is different from Figure 4.1. The antennas are oil filled and settled into the water. 2 mm glass layer exists under the antennas. Tissue is fat and tumor is in 30 mm depth.

Firstly, mechanical simulation is made using the simulation parameters shown in Table 4.2. Acoustic intensity values in the tissue are obtained by using HIFU simulator [32]. Then, force values are calculated according to equation 2-1. Force distribution as a function of the depth is shown in Figure 4.4.

Table 4.2. Mechanical simulation parameters of second simulation

Outer radius of transducer	2.1 cm
Inner radius of transducer	1 cm
Speed of ultrasound in fat	1450 m/s
Focal length of the transducer	0.03 m
Frequency of the ultrasound	3.3 MHz
Source frequency	35 Hz
Radius of the transducer	0.01 m
Young's Constant in breast tissue	5 kPa
Young's Constant in tumor	20 kPa

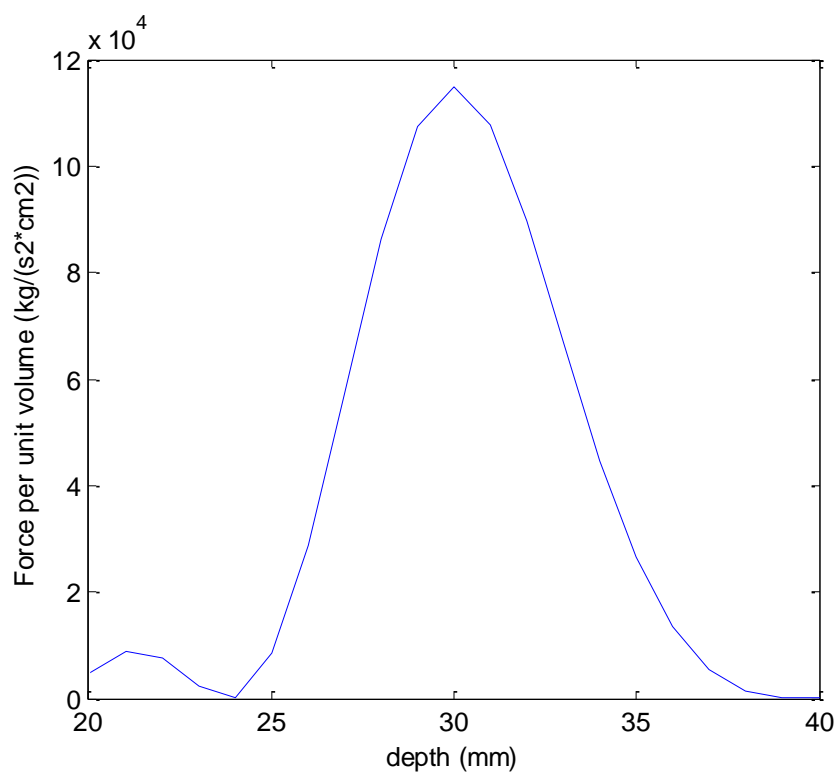


Figure 4.4. Force distribution of the transducer for tumor model in homogenous tissue model case

For this simulation geometry, y and z axis ultrasound scanning are performed. Firstly, $\pm 16\text{ mm}$ scanning is applied in y axis. The displacement values are recorded at the time when the displacement is maximum and minimum in the first period of displacement data. These values are recorded at all ultrasound coordinates in y axis. Figure 4.5 shows the maximum displacement values in each y coordinate. The displacement values are decreasing in the tumor region because tumor is stiffer than the fat tissue.

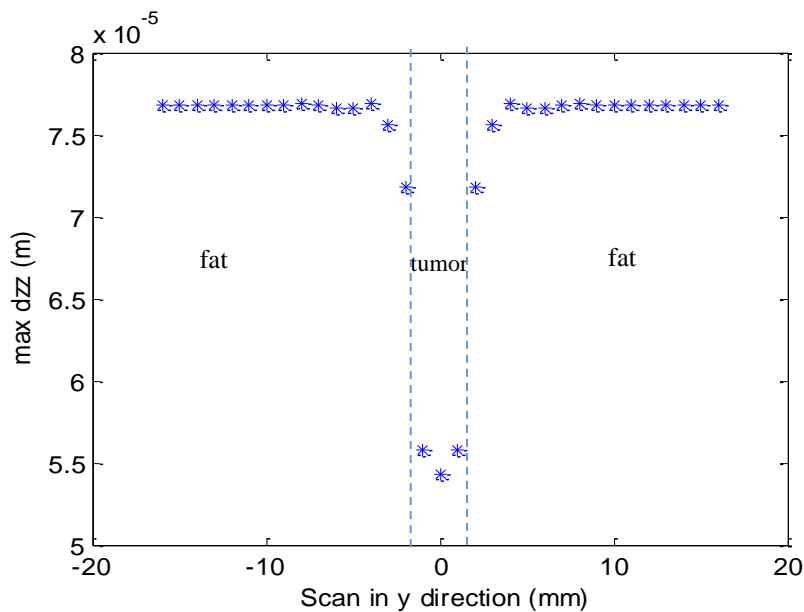


Figure 4.5. Mechanical simulation results obtained by the developed FDTD code. Figure 4.3 shows the simulation geometry. Modulation frequency is 35 Hz. Maximum displacement values at the focal point of the FUS are plotted for scan points in y direction between -16 mm and 16 mm.

After saving the displacement values, electromagnetic simulation is conducted. Received Doppler signal amplitude in each y coordinate is shown in Figure 4.6. It is seen that the signal level increases in the tumor region since the tumor is in the middle of the y axis. As expected, the signal changes symmetrically around the tumor position.

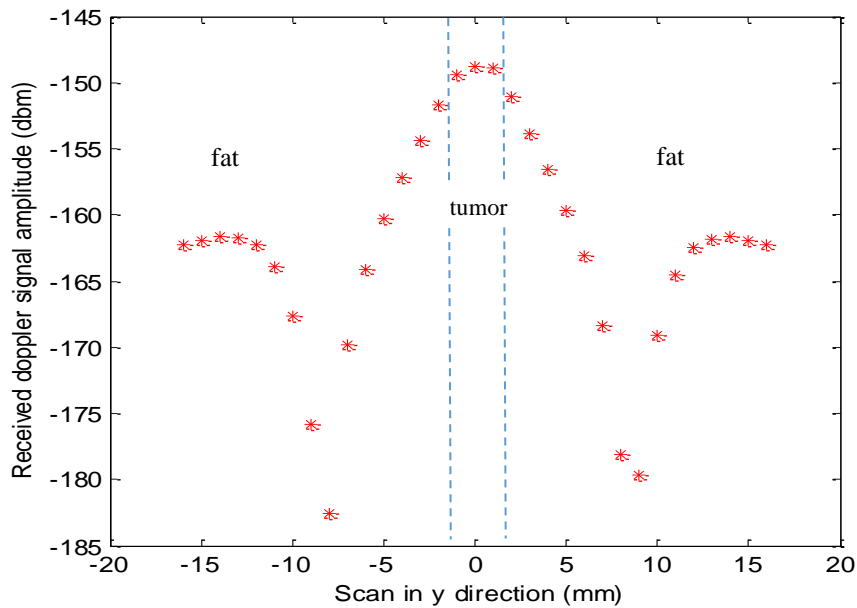


Figure 4.6. Electromagnetic simulation results obtained by the developed FDTD code for tumor inside homogenous fat model. Figure 4.3 shows the simulation geometry. Received Doppler signal amplitude values are plotted according to the scan points in y direction between -16 mm and 16 mm.

Next, the simulation results are recorded by scanning the z axis. In each case, the received Doppler amplitude is calculated as a function of the distance between the ultrasound focus and skin boundary in the range of 10 mm to 55 mm. The tumor center is at $z=30$ mm. The received signal amplitude according to distance in z direction is shown in Figure 4.7. It is observed that as the focus point approaches to the tumor, the signal level increases. It decreases as the distance to the tumor center increases.

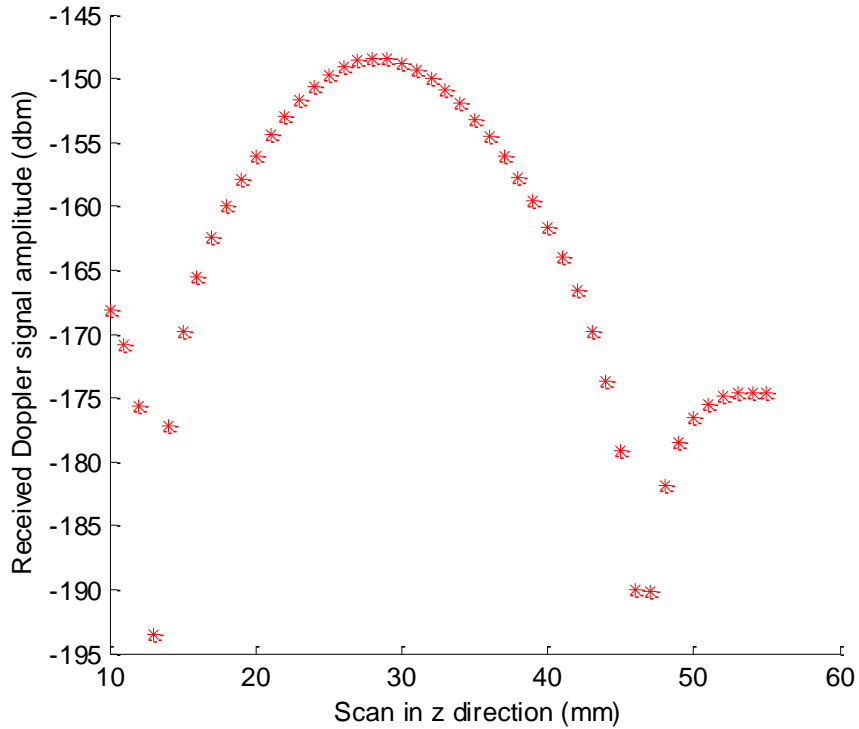


Figure 4.7. Received Doppler signal amplitude as a function of the distance between the ultrasound focus and tumor center ($z=30$ mm).

4.2. Tumor Inside Homogeneous Fibro Glandular Tissue in Fat

In this part of the thesis study, the performance of the HMMDI method is tested using simulations when the tumor model is located in the fibro glandular tissue model. Note that electrical parameters of the fibro glandular tissue are the same with the tumor's electrical parameters, however their mechanical properties are different. The simulation geometry is shown in Figure 4.8. Tumor model is located in the fibro glandular tissue model. Upper face of the fibro glandular tissue model is at 25 mm depth. The size of the fibro glandular is 27 mm \times 27 mm \times 12 mm. Tumor model exists at the top surface of the fibro glandular tissue model. The size of the tumor model is 3 mm \times 3 mm \times 3 mm. Electrical properties of the mediums are shown in Table 4.3.

Table 4.3. Electrical properties of the mediums used in the simulation geometry (Figure 4.8) [10].

Material Type	Relative permittivity	Conductivity (S/m)
Fat phantom	10	0.41
Tumor	50.52	4.92
Fibro glandular tissue	50.52	4.92
Glass	5.5	0
Antennas (Oil)	2.6	0.083
Water	77.15	4.406

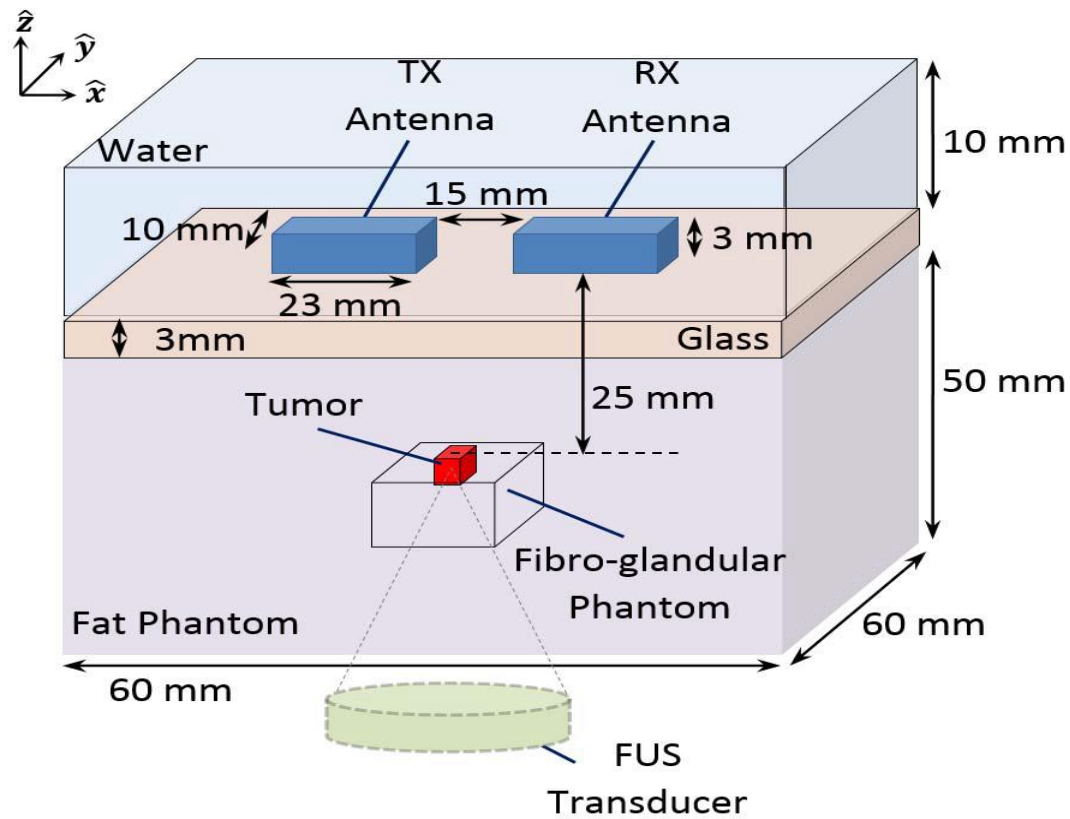


Figure 4.8. Tumor in fibro glandular tissue simulation geometry [16].

Since the same FUS transducer is used, the force distribution calculated for the homogeneous breast model is used in this simulation. Mechanical properties are also

the same except Young's Modulus constants and the ultrasound modulation frequency. The elasticity parameters are shown in Table 4.4.

Table 4.4. *Elasticity parameters of tumor in fibro glandular tissue simulation*

Poisson constant	0.495
Frequency	3.3 MHz
Modulation frequency	15 Hz
Young's Constant in breast tissue	4320 Pa
Young's Constant in fibro glandular tissue	16720 Pa
Young's Constant in tumor	76960 Pa

FUS transducer scans in the y direction around ± 16 mm from the tumor center with 2 mm steps. Maximum and minimum displacements in the first period of the displacement are calculated at each y coordinate and shown in Figure 4.9. Maximum displacement values decrease from fat to fibro glandular tissue since Young Modulus of the fibro glandular tissue is greater than fat's modulus. Furthermore, maximum displacement values decrease as the FUS transducer moves from fibro glandular to tumor region, because tumor's Young's Modulus is approximately 6 times greater than fibro glandular's Young's Modulus.

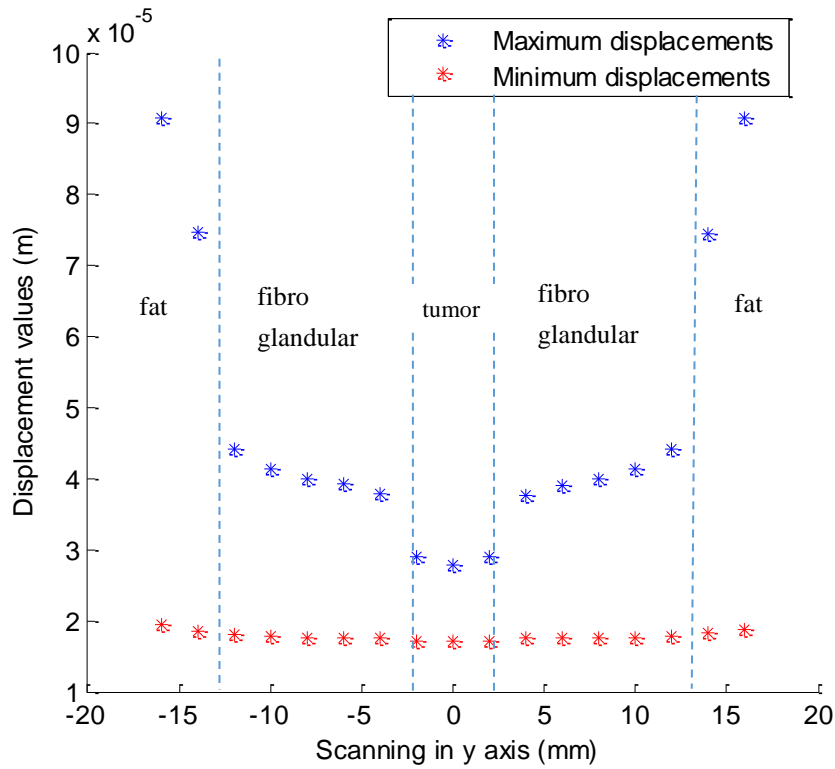


Figure 4.9. Mechanical simulation results for tumor inside fibro glandular tissue in fat. Figure 4.8 shows the simulation geometry. Modulation frequency is 15 Hz. Maximum and minimum displacement values at the focal point of the FUS are plotted for scan points in y direction between -16 mm and 16 mm.

Electromagnetic simulation is made by using this mechanical data. The results are shown in Figure 4.10. According to the electromagnetic simulations, tumor can be distinguished from the fibro glandular tissue. The signal value decreases as the focus point moves from fat to fibro glandular and fibro glandular to tumor. 15 dB difference occurs when focus point passes from fibro glandular tissue to tumor region.

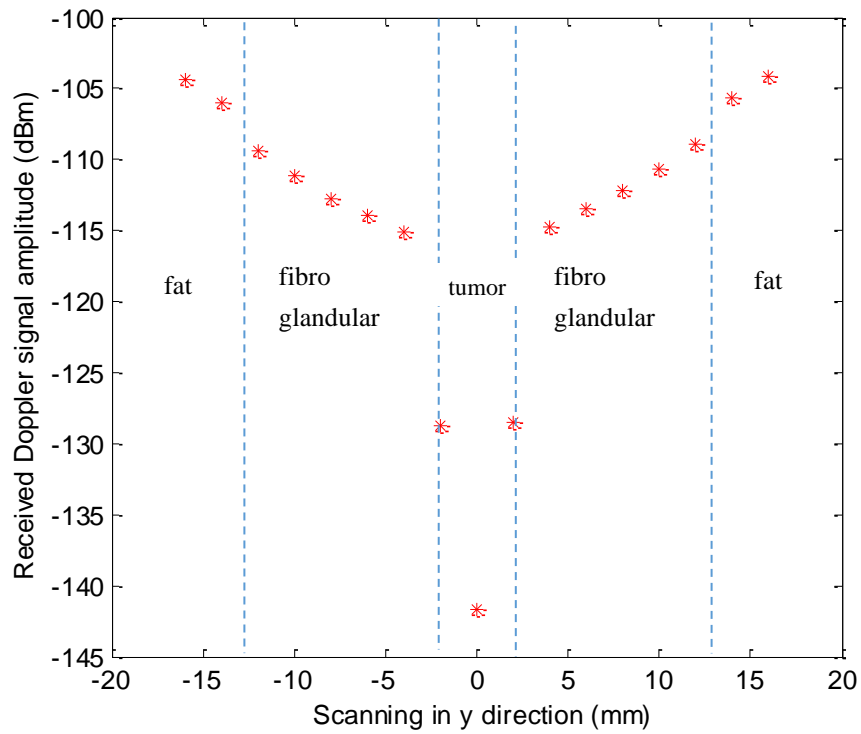


Figure 4.10. The received Doppler signal versus scan position in y direction. Electromagnetic simulation results when a tumor is in the fibro glandular tissue (Figure 4.8). The modulation frequency is 15 Hz.

Another simulation is made to understand the effects of tumor location. The Doppler signal pattern is analyzed when the tumor is displaced by 4 mm in the $-y$ axis direction. Firstly, a mechanical simulation is made. Figure 4.11 shows that the signal pattern shifts by 4 mm compared to the signal pattern presented in Figure 4.9.

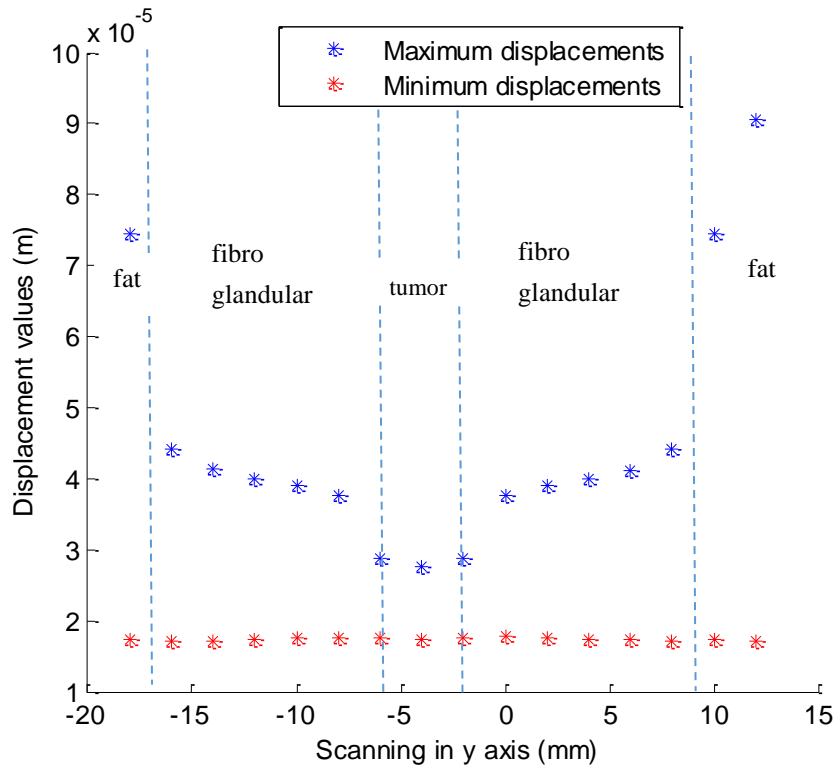


Figure 4.11. Mechanical simulation results for tumor inside fibro glandular tissue in fat. Figure 4.8 shows the simulation geometry but the tumor is shifted by 4 mm in $-y$ direction. Modulation frequency is 15 Hz. Maximum and minimum displacement values at the focal point of the FUS are plotted for scan points in y direction between -16 mm and 16 mm.

Figure 4.12 shows the results when the electromagnetic simulation is run according to this mechanical data. The plot is shifted by 4 mm in y axis compared to Figure 4.10 but there is an asymmetry between right and left side of the plot. The asymmetry can be explained as follows: The distance of the tumor from the transmitter antenna is different from the distance from receiver antenna, so the losses of the receive and transmit paths are different from each other. This difference leads to nonequal Doppler signal amplitude on the right and left side of the tumor.

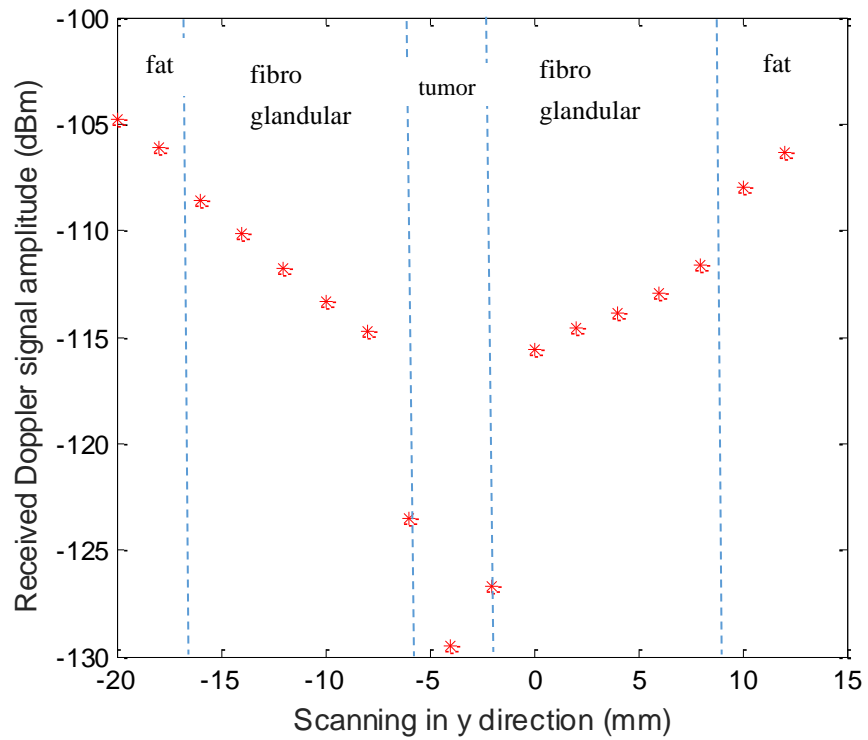


Figure 4.12. Electromagnetic simulation results for tumor inside fibro glandular tissue in fat. Figure 4.8 shows the simulation geometry but the tumor is shifted by 4 mm in $-y$ direction. Modulation frequency is 15 Hz. Received Doppler signal amplitude values are plotted for scan points in y direction between -16 mm and 16 mm.

To restore symmetry, antennas are also displaced according to center of the shifted tumor and electromagnetic simulation is repeated. The symmetry is restored when there is symmetry between antennas and the tumor (Figure 4.13).

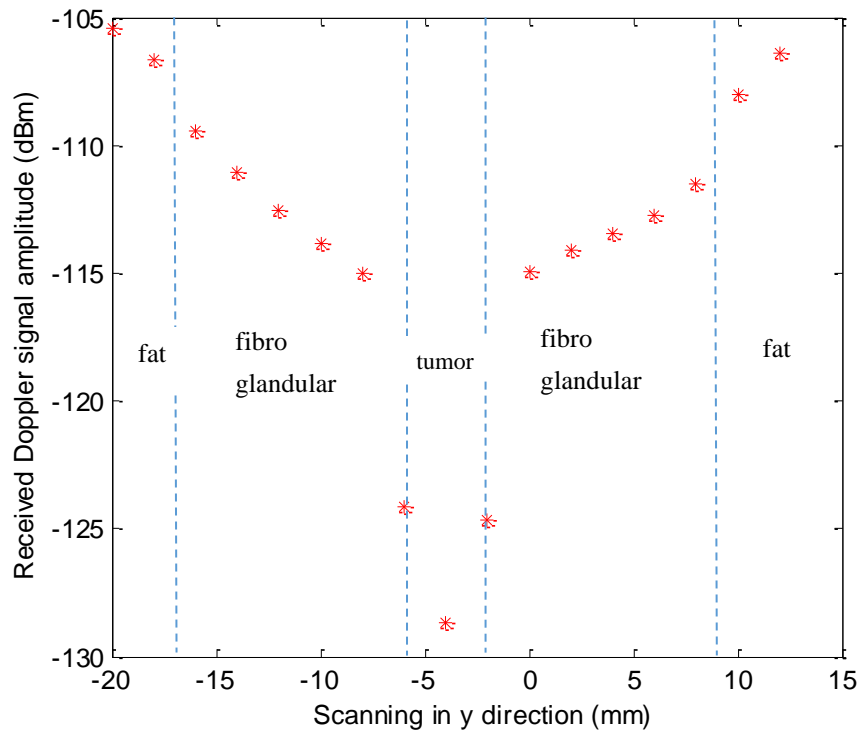


Figure 4.13. Received Doppler signal amplitude when the tumor is displaced by 4 mm in the $-y$ axis. The antennas are shifted to restore the symmetry.

The tumor is shifted by 10 mm in the $-y$ axis in the next simulation. The mechanical results are shown in Figure 4.14. It is observed that center of the tumor is displaced by 10 mm as expected.

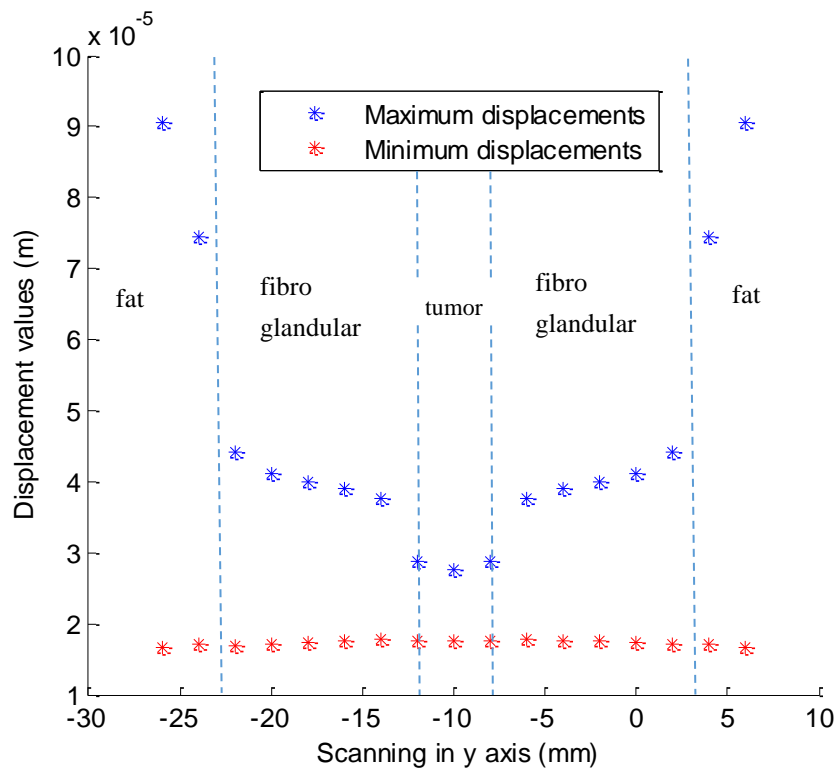


Figure 4.14. Displacement values when the tumor is displaced by 10 mm in the $-y$ axis.

Electromagnetic simulation of this experiment is also made and this time antennas are directly shifted according to tumor's center position to satisfy the symmetry according to previous experience. Figure 4.15 shows the Doppler signal levels as a function of scanning in y direction. Since the antennas are also shifted the plot is symmetric.

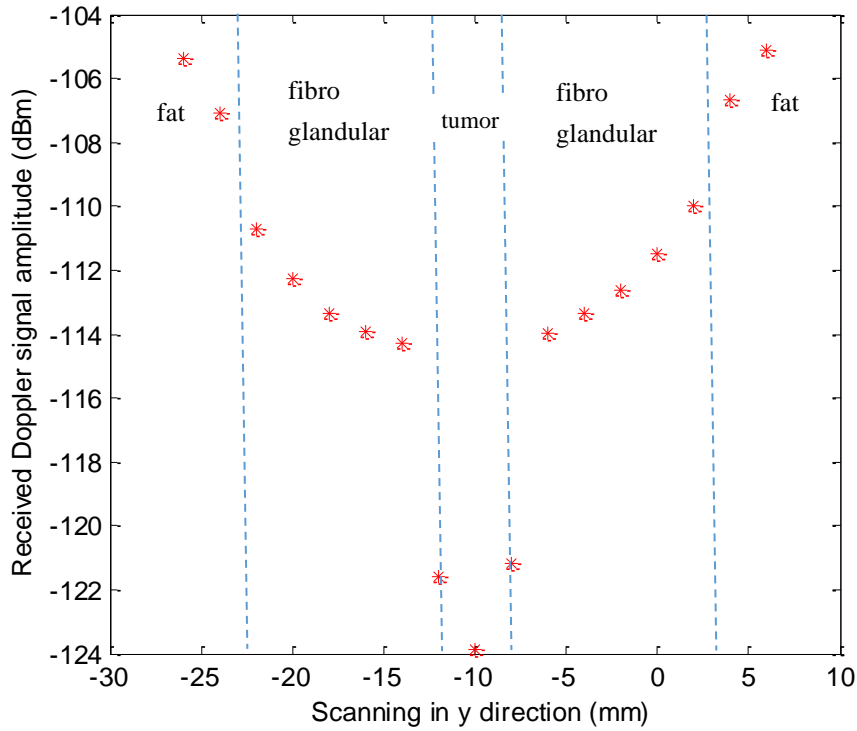


Figure 4.15. Electromagnetic simulation of tumor displaced by 10 mm in the $-y$ axis and antennas are shifted.

4.3. Tumor Inside Realistic Tissue Model

Previous studies are made with a homogenous background tissue, but breast tissues are not homogenous. Breast contains lobules and connective tissues which make it inhomogeneous. University of Wisconsin Cross-Disciplinary Electromagnetics Laboratory (UWCEM) has a 3-D breast phantom electromagnetic data repository [33]. There are different types of phantom examples in this repository. Mainly, breast phantoms are classified according to ACR (American College of Radiology). These categories are created according to content of the fibro glandular density within breasts [34]. The properties of these phantoms are presented in Table 4.5.

Table 4.5. Breast phantom types according to ACR

Phantom Type	Definition
Class I	Entirely fat
Class II	Includes scattered fibro glandular densities
Class III	Heterogeneously dense
Class IV	Extremely dense

In this study, Class III type breast phantom data is used. This type of breast includes fibro connective/glandular, fatty and glandular tissues. Fibro glandular areas are heterogeneously dense in this type of tissue which may obscure small tumors. The simulation geometry is shown in Figure 4.16.

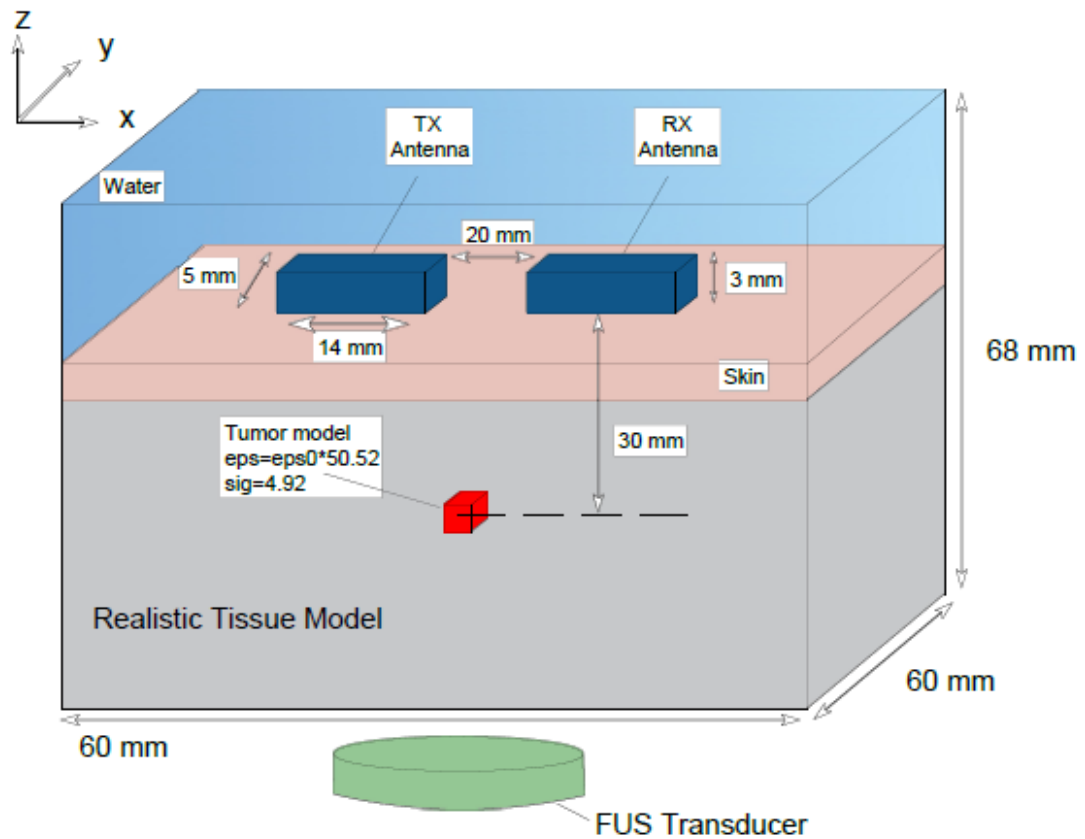


Figure 4.16. Realistic tissue simulation model based on Class III type of phantom data according to ACR.

Then mechanical simulations are made for modulation frequencies of $f=15$ Hz, $f=20$ Hz and $f=30$ Hz. The same transducer is used as in the homogenous tissue example. There is a tumor model at 30 mm depth. Tumor model is represented as a 3 mm x 3 mm x 3 mm cube. Young Modulus of the tumor and realistic tissue are assumed 20000 Pa and 5000 Pa, respectively. Cell sizes are assumed 1 mm in all directions. The results are shown in Figure 4.17, Figure 4.18 and Figure 4.19. When the tumor is absent, there is no change in the displacement. Tumor's existence decreases the displacement values as expected. In addition, displacement values decrease with increasing modulation frequency.

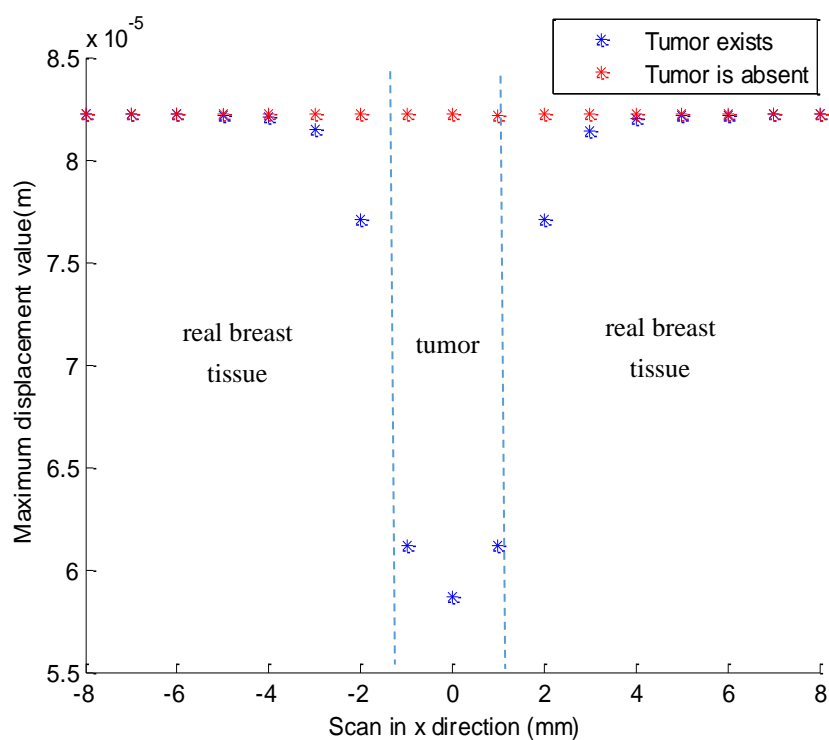


Figure 4.17. Maximum displacement values calculated when there is no tumor in the breast model. Maximum displacement values are also calculated when there is tumor in the middle (Modulation frequency $f=15$ Hz).

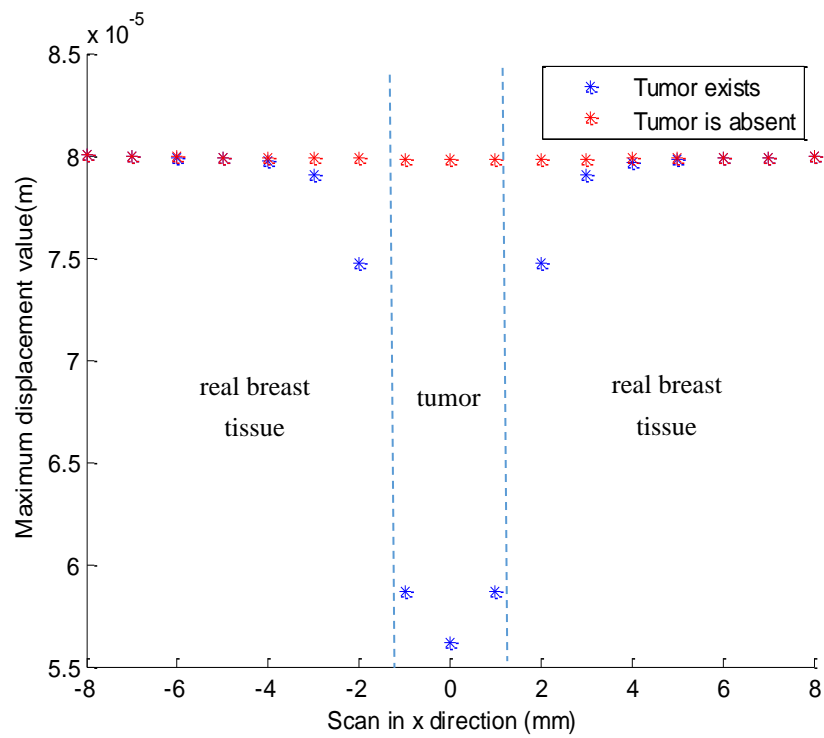


Figure 4.18. Maximum displacement values calculated when there is no tumor in the breast model. Maximum displacement values are also calculated when there is tumor in the middle (Modulation frequency $f=20$ Hz).

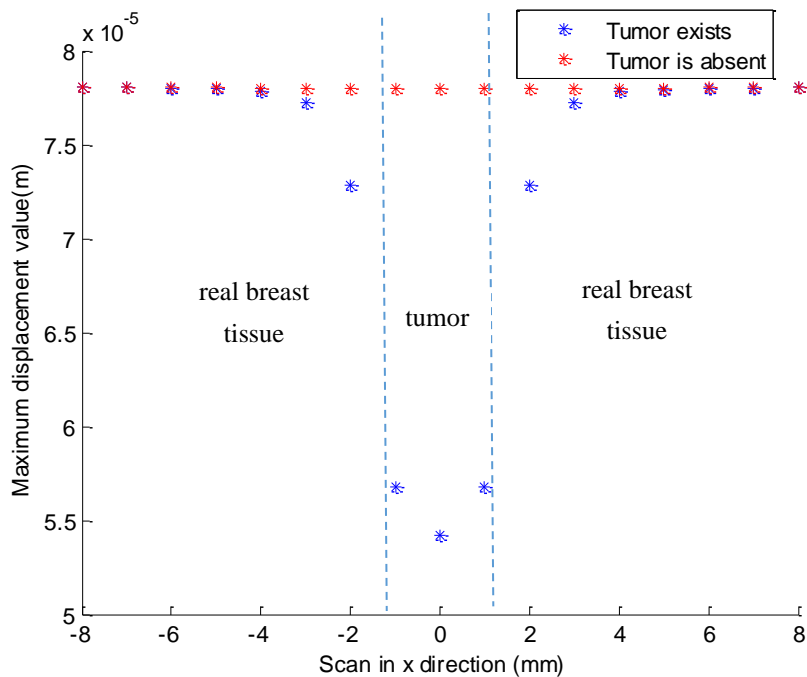


Figure 4.19. Maximum displacement values calculated when there is no tumor in the breast model. Maximum displacement values are also calculated when there is tumor in the middle (Modulation frequency $f=30$ Hz).

After the mechanical simulations, electromagnetic simulations are run with these mechanical outputs. Electrical parameters of Class III breast tissue model are used in the simulation. Reduced portion of the model is used in these simulations. In Figure 4.20, Figure 4.21 and Figure 4.22 x, y and z cross sectional views of the model are shown. The model employed in the simulations are shown in the corresponding rectangular regions. Tumor is shown as a small rectangle in the figures. In these simulations, dimensions of the breast model are 60 mm x 60 mm x 68 mm. 10 cells PML exists in each direction. The microwave operation frequency is 5 GHz. The other details are shown in Figure 4.16.

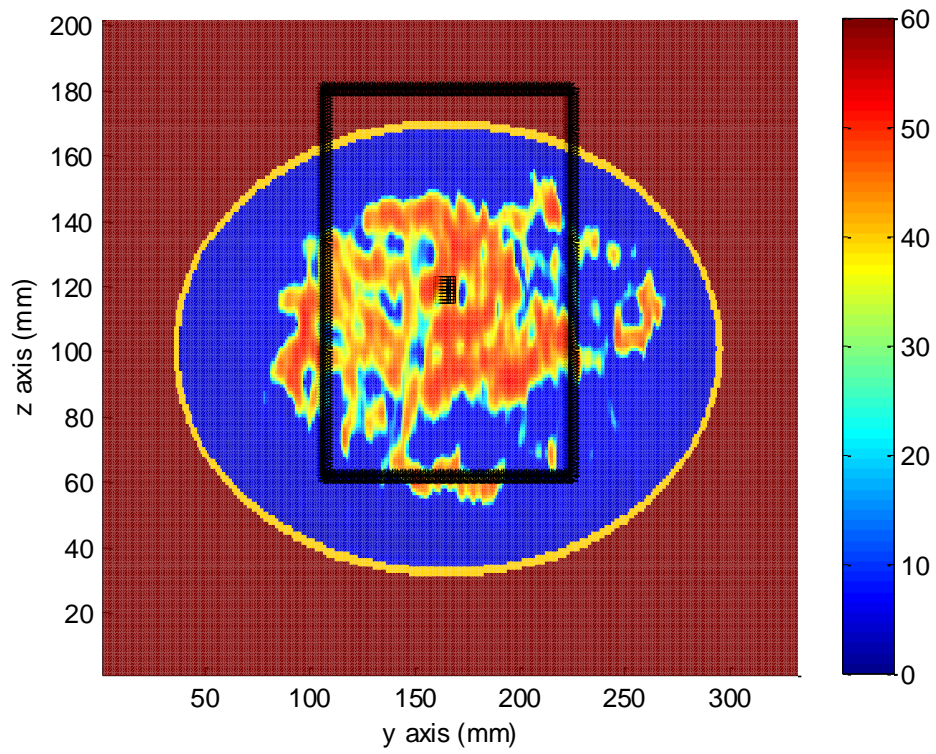


Figure 4.20. The relative permittivity distribution in the $x=75$ mm cross section of the Class III realistic breast tissue model [20]. The portion of the model used in the simulations is shown in the rectangular region. Tumor is shown as dark square region in the middle.

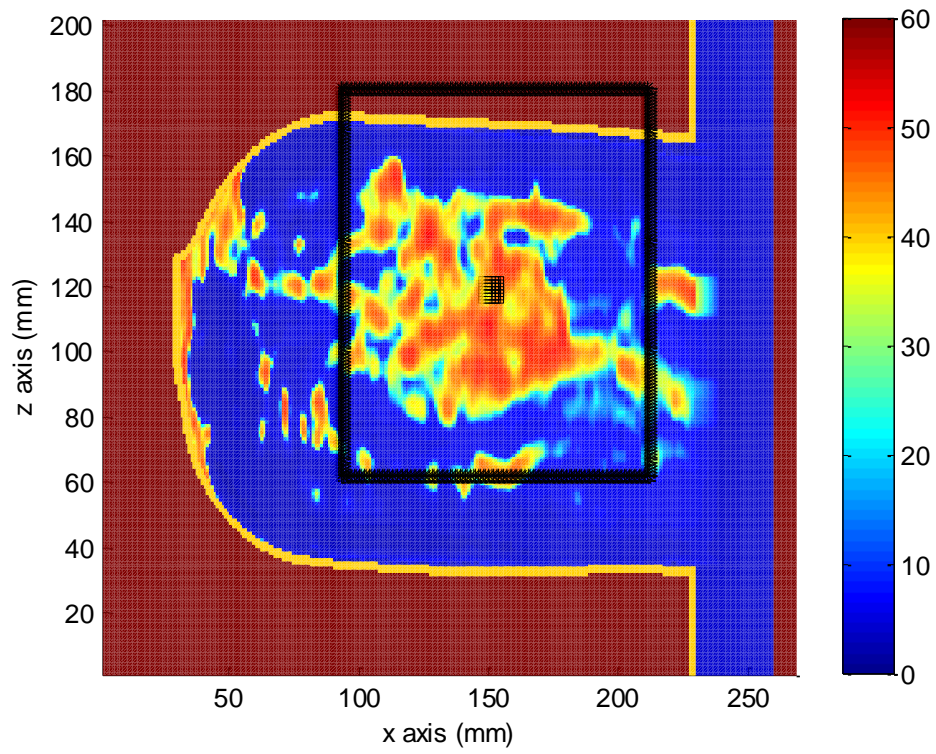


Figure 4.21. The relative permittivity distribution in the $y=81.5$ mm cross section of the Class III realistic breast tissue model [20]. The portion of the model used in the simulations is shown in the rectangular region. Tumor is shown as dark square region in the middle.

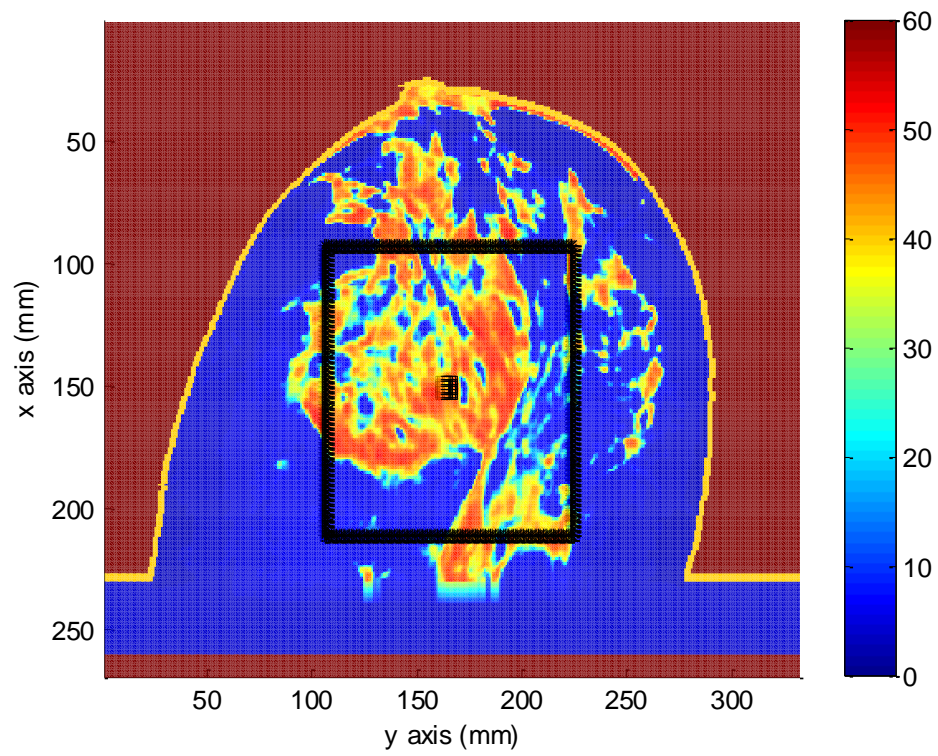


Figure 4.22. The relative permittivity distribution in the $z=59$ mm cross section of the Class III realistic breast tissue model [20]. The portion of the model used in the simulations is shown in the rectangular region. Tumor is shown as dark square region in the middle.

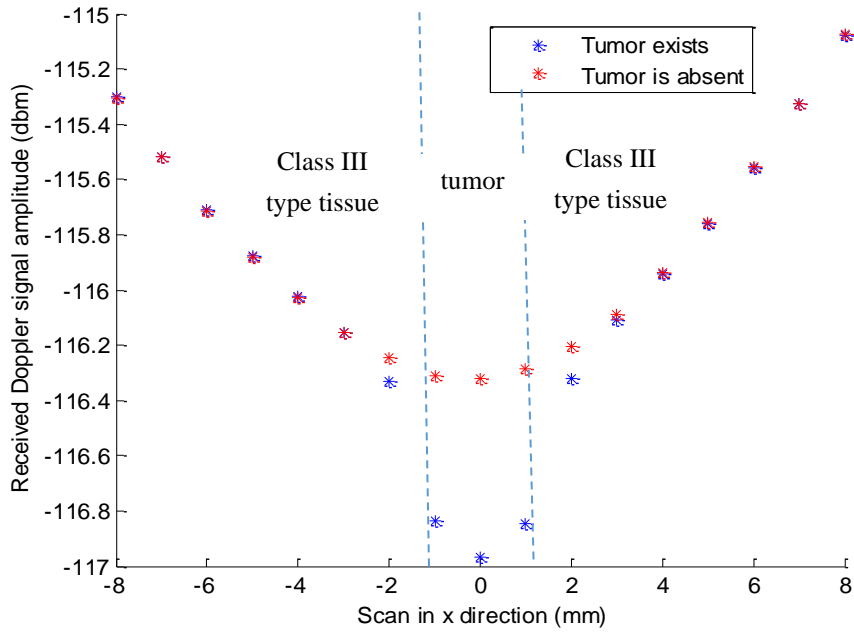


Figure 4.23. Electromagnetic simulation results for tumor inside real breast tissue for Class III. Figure 4.16 shows the simulation geometry. Modulation frequency is 15 Hz. Received Doppler signal amplitude values are plotted for scan points in x direction between -8 mm and 8 mm.

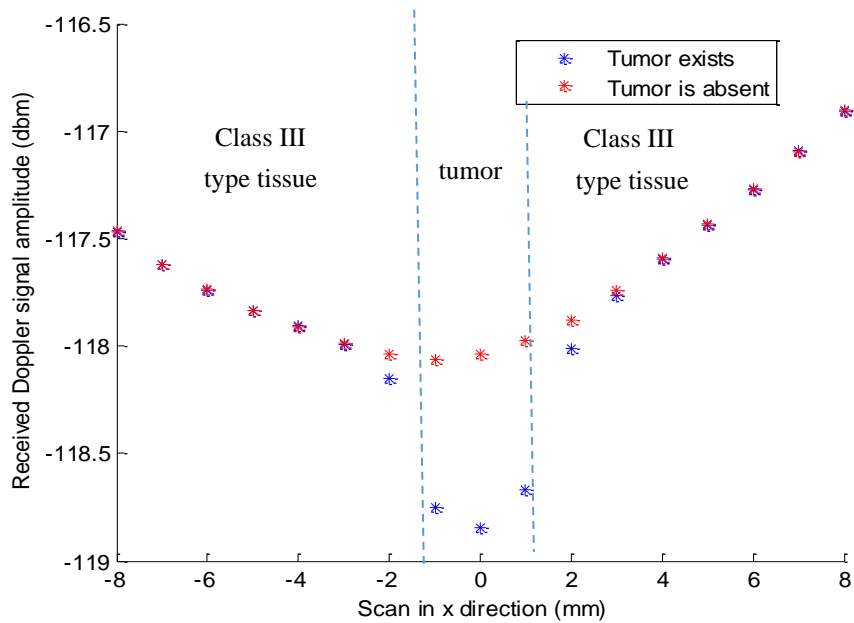


Figure 4.24. Electromagnetic simulation results for tumor inside real breast tissue for Class III. Figure 4.16 shows the simulation geometry. Modulation frequency is 20 Hz. Received Doppler signal amplitude values are plotted for scan points in x direction between -8 mm and 8 mm.

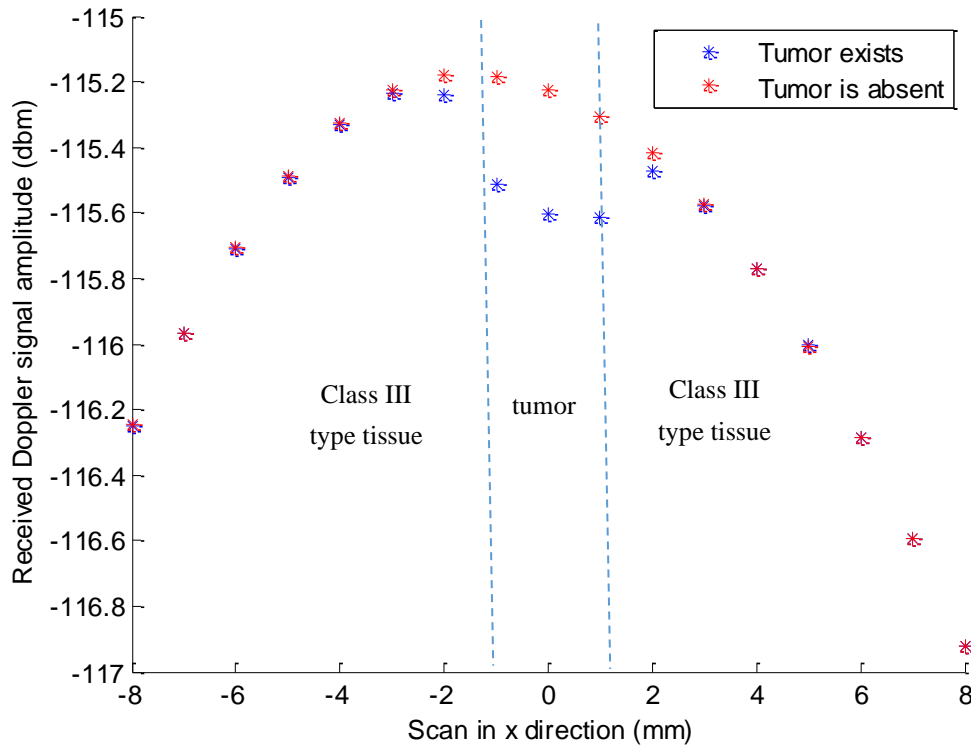


Figure 4.25. Electromagnetic simulation results for tumor inside real breast tissue for Class III. Figure 4.16 shows the simulation geometry. Modulation frequency is 30 Hz. Received Doppler signal amplitude values are plotted for scan points in x direction between -8 mm and 8 mm.

In these electromagnetic simulations, different modulation frequencies are applied. Simulation results are obtained for two cases, namely, when there is no tumor and when there is a tumor region in the breast model. The Doppler signal amplitudes are drawn together and difference between them is analyzed. Tumor exists in -1, 0, +1 region in the x axis. The simulation results are shown in Figure 4.23, Figure 4.24 and Figure 4.25. In these results, Doppler signal changes in the tumor region. Existence of the tumor reduces the received Doppler signal amplitude maximum 0.7 dB. For all modulation frequencies, tumor can be detected in the realistic simulation domain. The graphics are not symmetric because dielectric distribution of the geometry is not homogenous. Doppler signals are affected from this distribution.

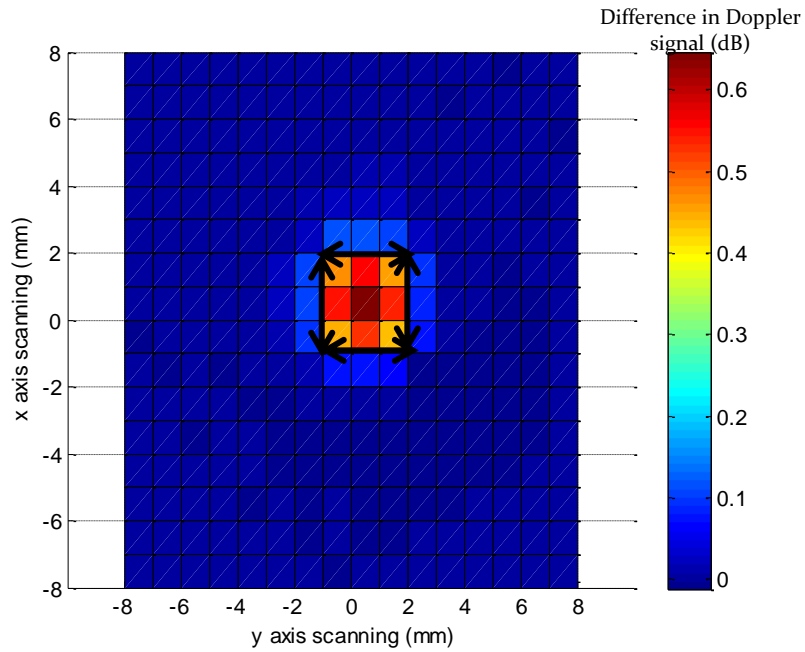


Figure 4.26. Electromagnetic simulation results for tumor inside real breast tissue for Class III. Modulation frequency is 15 Hz. Tumor region is shown with arrows. Doppler signal difference between tumor is absent and tumor is present are plotted for scan points in x direction between -8 mm and 8 mm together with y direction between -8 mm and 8 mm.

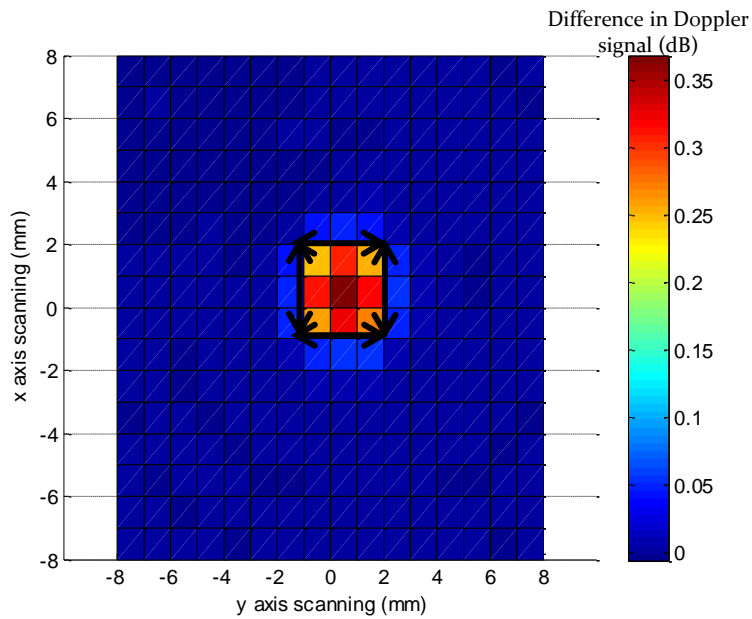


Figure 4.27. Electromagnetic simulation results for tumor inside real breast tissue for Class III. Modulation frequency is 30 Hz. Tumor region is shown with arrows. Doppler signal difference between tumor is absent and tumor is present are plotted for scan points in x direction between -8 mm and 8 mm together with y direction between -8 mm and 8 mm.

In addition to 1 dimensional scanning, 2 dimensional scanning is performed for Class III type example. The simulation results are shown in Figure 4.26 and Figure 4.27. Difference in received Doppler signal amplitude between tumor is absent and tumor is present is analyzed. Tumor exists in -1, 0, +1 region in the x axis and -1, 0, +1 region in y axis. The maximum Doppler signal difference is seen in the tumor region for modulation frequencies $f=15$ Hz and $f=30$ Hz.

In next example, Class IV type breast phantom data is used. This type of breast includes fibro connective/glandular, fatty and glandular tissues as Class III but fibro glandular areas are extremely dense in this type of tissue. The same simulation geometry (Figure 4.16) is used in this simulation. The mechanical simulations are made for modulation frequencies of $f=15$ Hz. and $f=30$ Hz. Elastic properties of the medium are same with Class III so the mechanical results (Figure 4.17 and Figure 4.19) do not change according to Class III. In electromagnetic simulations, reduced portion of the class IV model is used. In Figure 4.28, Figure 4.29 and Figure 4.30 x, y and z cross sectional views of the model are shown. The model employed in the simulations are shown in the corresponding rectangular regions. Tumor is shown as a small rectangle in the figures.

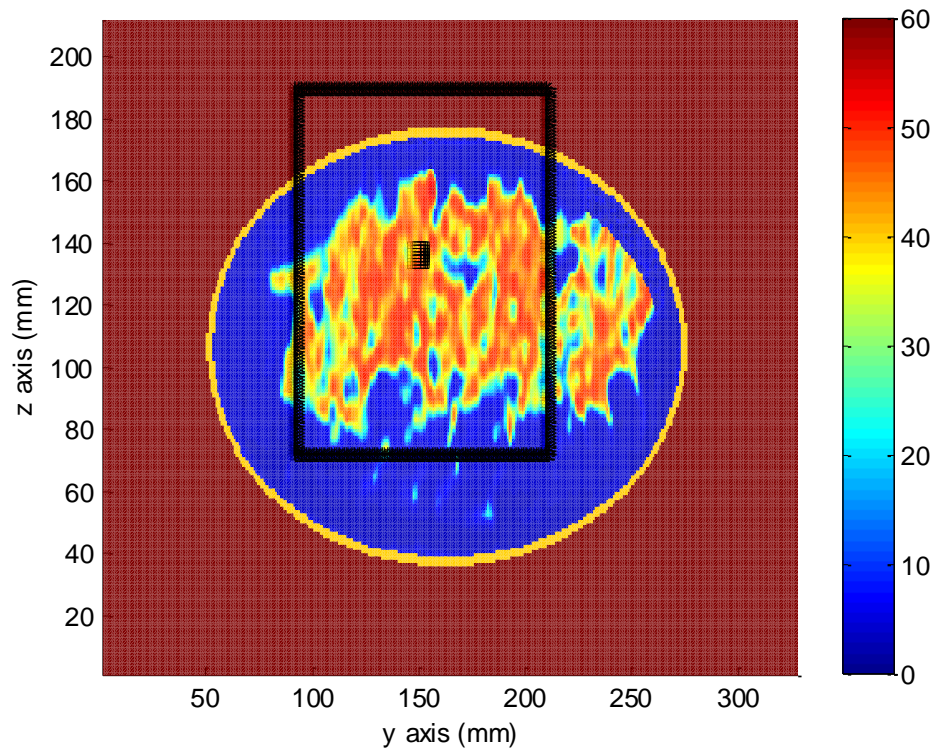


Figure 4.28. The relative permittivity distribution in the $x=54.5$ mm cross section of the Class IV realistic breast tissue model [20]. The portion of the model used in the simulations is shown in the rectangular region. Tumor is shown as dark square region in the middle.

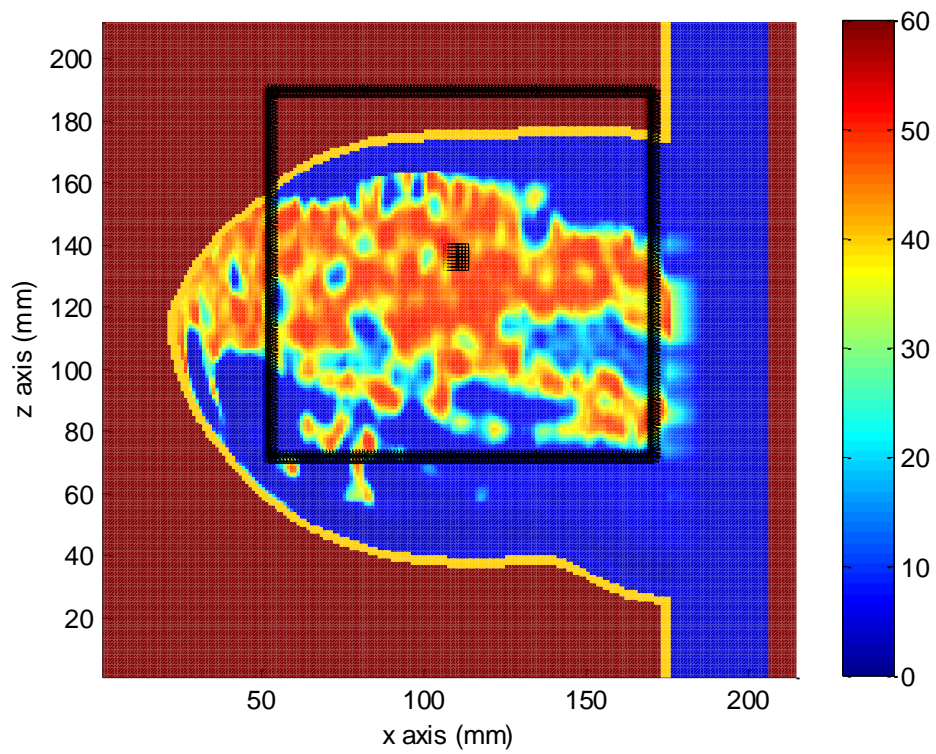


Figure 4.29. The relative permittivity distribution in the $y=74.5$ mm cross section of the Class IV realistic breast tissue model [20]. The portion of the model used in the simulations is shown in the rectangular region. Tumor is shown as dark square region in the middle.

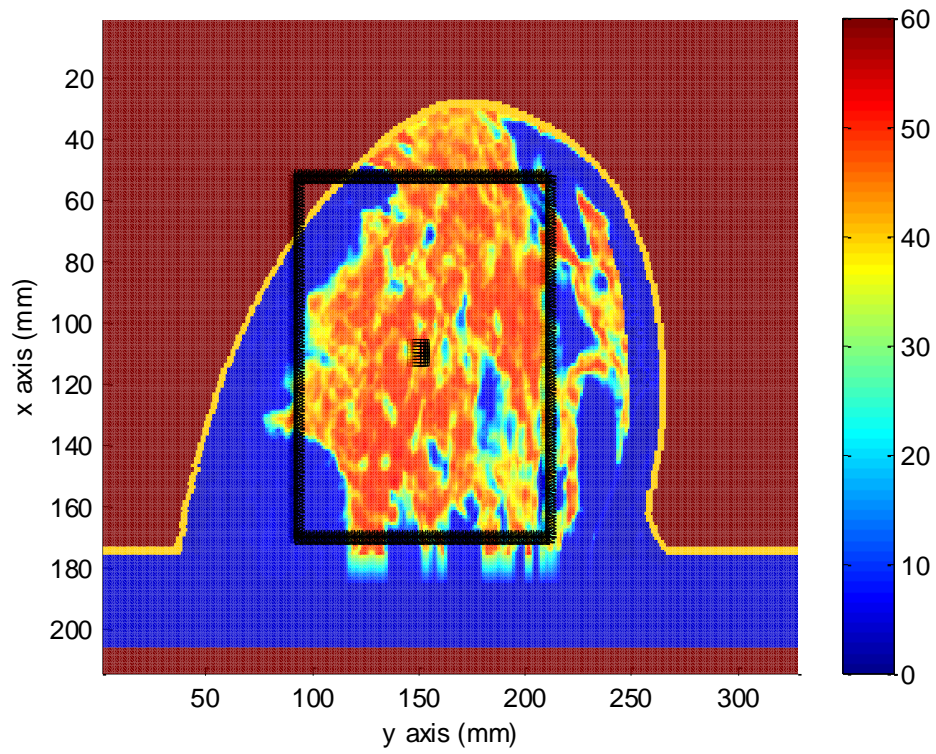


Figure 4.30. The relative permittivity distribution in the $z=67.5$ mm cross section of the Class IV realistic breast tissue model [20]. The portion of the model used in the simulations is shown in the rectangular region. Tumor is shown as dark square region in the middle.

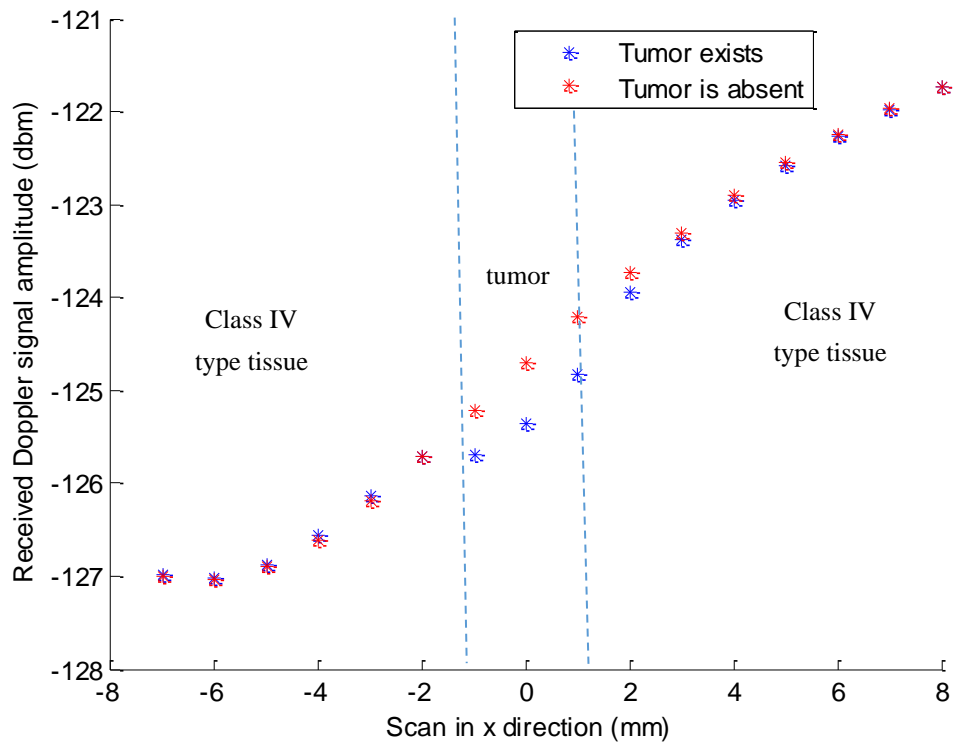


Figure 4.31. Electromagnetic simulation results for tumor inside real breast tissue for Class IV. Figure 4.16 shows the simulation geometry. Modulation frequency is 15 Hz. Received Doppler signal amplitude values are plotted for scan points in x direction between -8 mm and 8 mm.

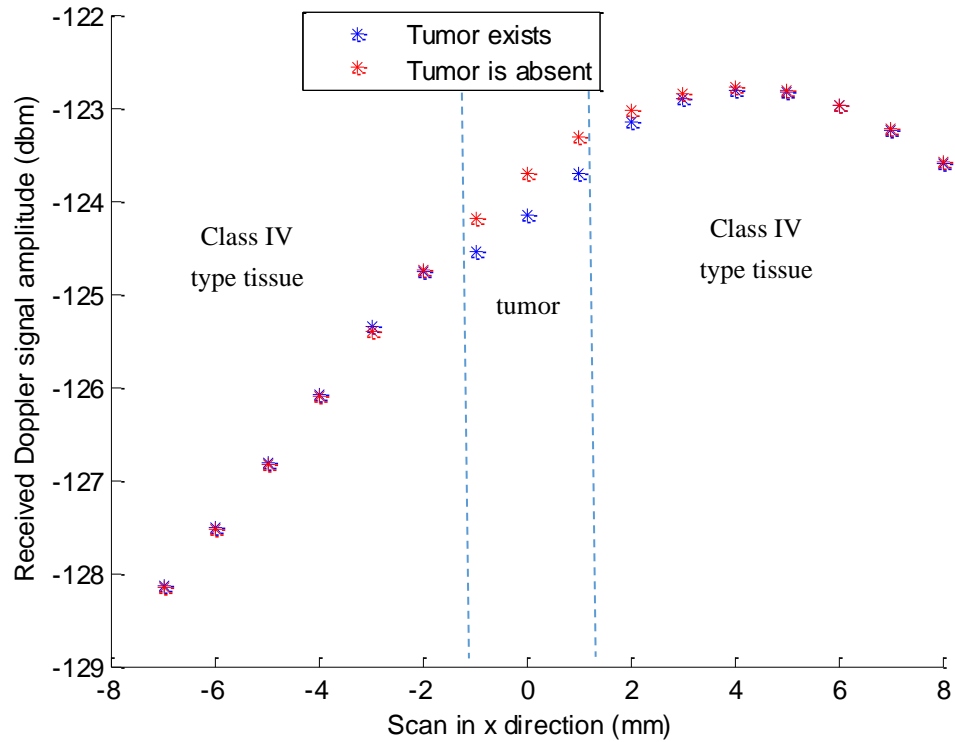


Figure 4.32. Electromagnetic simulation results for tumor inside real breast tissue for Class IV. Figure 4.16 shows the simulation geometry. Modulation frequency is 30 Hz. Received Doppler signal amplitude values are plotted for scan points in x direction between -8 mm and 8 mm.

The electromagnetic simulation results for Class IV real breast tissue model are shown in Figure 4.31 and Figure 4.32. 15 Hz and 30 Hz modulation frequencies are used. The microwave operation frequency is 5 GHz. The received Doppler signal amplitudes in the presence and absence of tumor are plotted together. Doppler signal with and without the tumor is different in [-1, +1] region on x axis. Existence of the tumor reduces the received Doppler signal amplitude maximum 0.7 dB for Class IV type. Difference between Doppler signals decreases with increasing modulation frequency. Although fibro glandular areas are extremely dense in Class IV type tissue, tumor region can be distinguished for all modulation frequencies.

In final example, Class II type breast phantom data is used. This type of breast includes scattered fibro glandular tissues but fibro glandular areas are not dense as Class III and Class IV type of tissue. The same simulation geometry (Figure 4.16) is used in this simulation. The mechanical simulations are made for modulation frequencies of $f=15\text{Hz}$. and $f=30\text{ Hz}$. Elastic properties of the medium are same with Class III and Class IV, then mechanical results (Figure 4.17 and Figure 4.19) do not change. In electromagnetic simulations, reduced portion of the class II model is used. In Figure 4.33, Figure 4.34 and Figure 4.35 x, y and z cross sectional views of the model are shown. The model employed in the simulations are shown in the corresponding rectangular regions. Tumor is shown as a small rectangle in the figures.

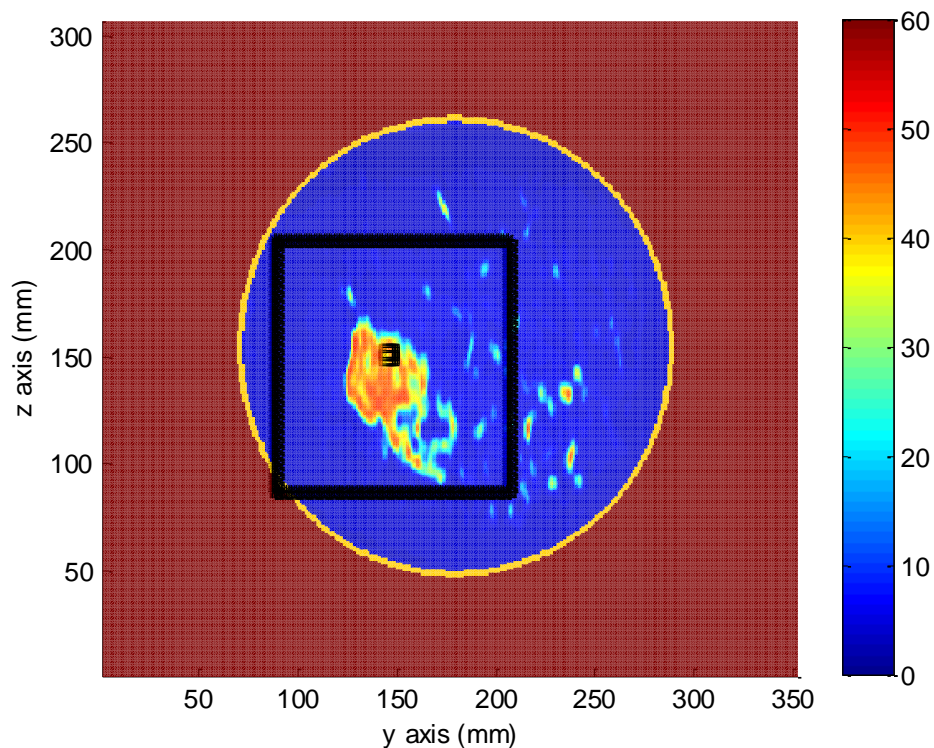


Figure 4.33. The relative permittivity distribution in the $x=69.5\text{ mm}$ cross section of the Class II realistic breast tissue model [20]. The portion of the model used in the simulations is shown in the rectangular region. Tumor is shown as dark square region in the middle.

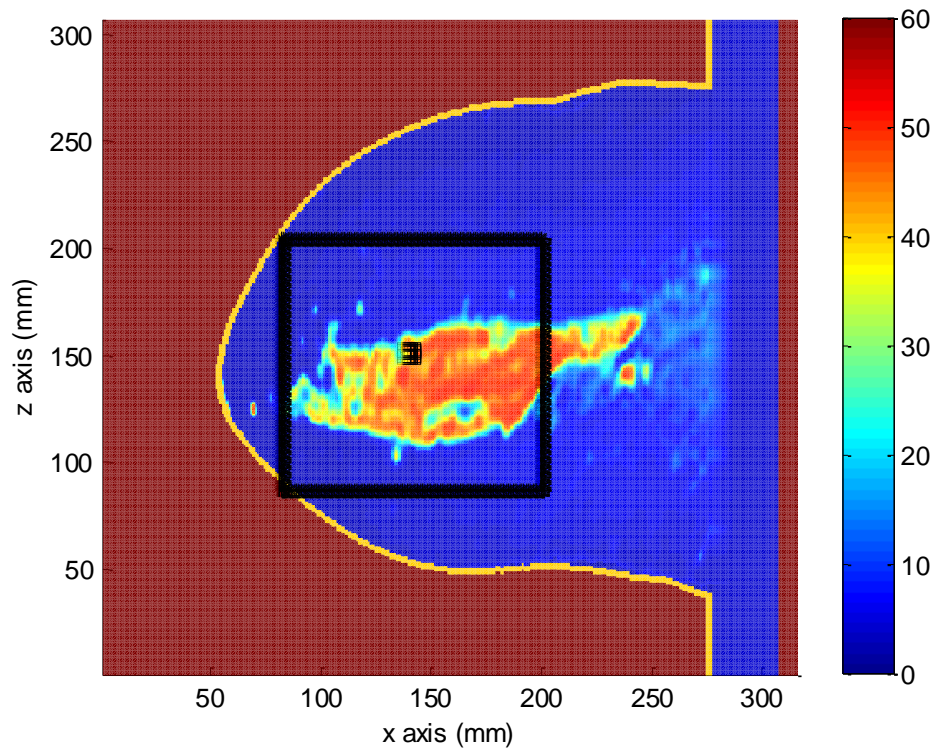


Figure 4.34. The relative permittivity distribution in the $y=72.5$ mm cross section of the Class II realistic breast tissue model [20]. The portion of the model used in the simulations is shown in the rectangular region. Tumor is shown as dark square region in the middle.

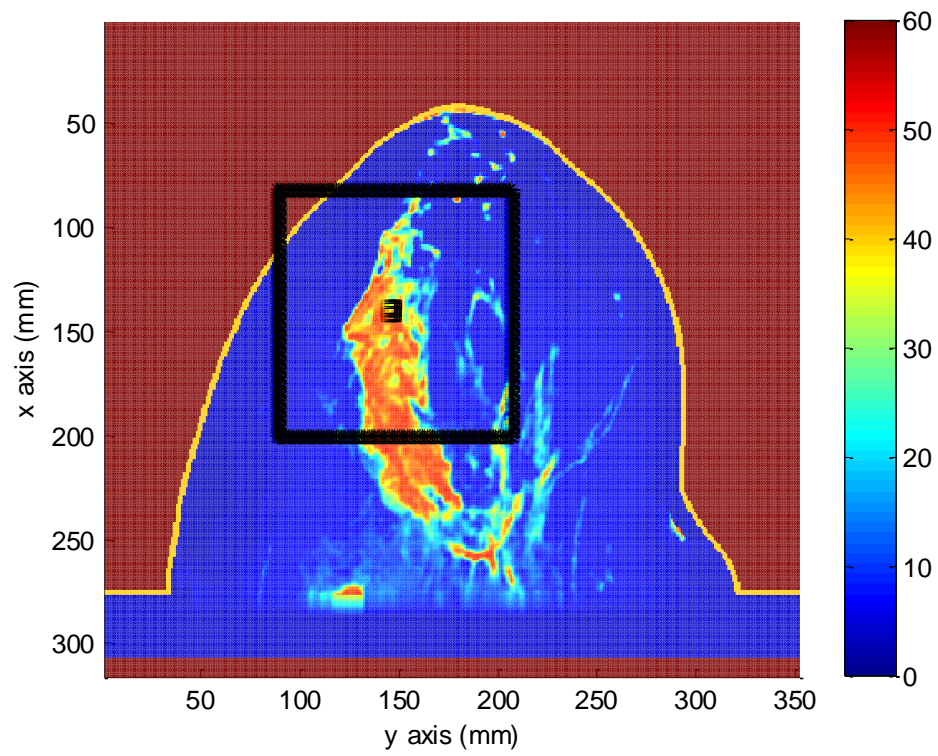


Figure 4.35. The relative permittivity distribution in the $z=75.5$ mm cross section of the Class II realistic breast tissue model [20]. The portion of the model used in the simulations is shown in the rectangular region. Tumor is shown as dark square region in the middle.

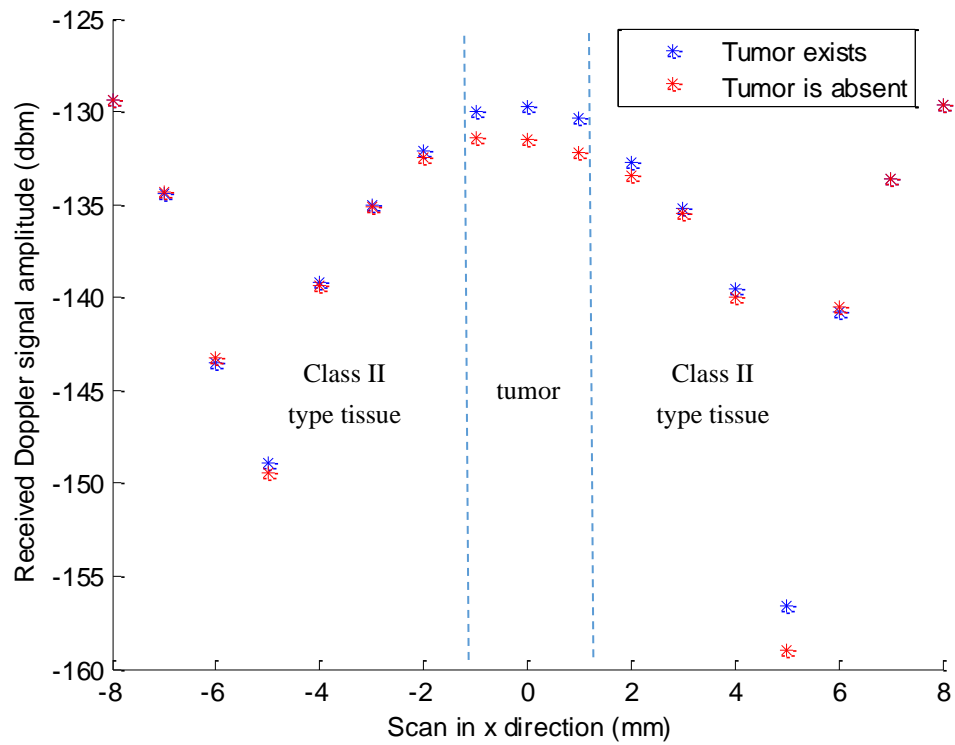


Figure 4.36. Electromagnetic simulation results for tumor inside real breast tissue for Class II. Figure 4.16 shows the simulation geometry. Modulation frequency is 15 Hz. Received Doppler signal amplitude values are plotted for scan points in x direction between -8 mm and 8 mm.

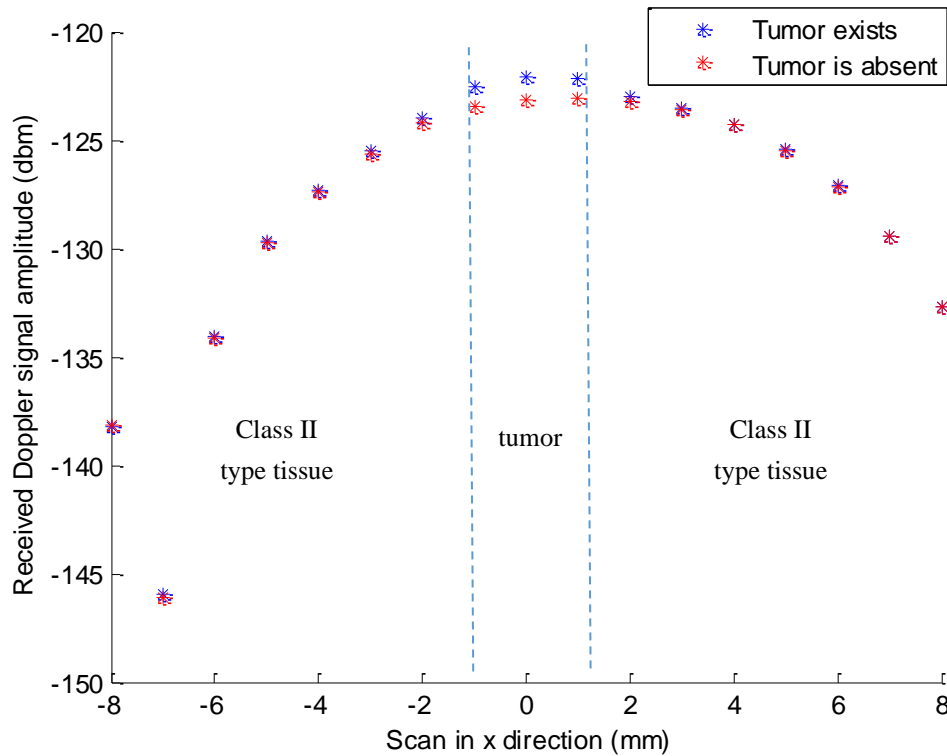


Figure 4.37. Electromagnetic simulation results for tumor inside real breast tissue for Class II. Figure 4.16 shows the simulation geometry. Modulation frequency is 30 Hz. Received Doppler signal amplitude values are plotted for scan points in x direction between -8 mm and 8 mm.

In these electromagnetic simulations, $f=15$ Hz and $f=30$ Hz modulation frequencies are applied. The microwave operation frequency is 5 GHz. The results are shown in Figure 4.36 and Figure 4.37. Simulations are run with and without the tumor in the breast model. Doppler signal changes again in the tumor region as in Class III and Class IV models but this time, the signal when tumor exists is higher than the signal when tumor does not exist. Since the region has low densities, Doppler signal increases in the tumor region as in the homogenous breast tissue model. Tumor is detected for two modulation frequencies.

4.4. Conclusions

In this chapter, different scenarios are solved for the HMMDI problem. Three types of tissue models are introduced. Initially tumor inside a homogenous tissue is modelled. In this problem, Doppler signal increases in the tumor region. Secondly, tumor in the fibro glandular region is modelled. Tumor and fibro glandular tissue has the same electrical properties but their mechanical properties are different. Doppler signal level decreases in the tumor region compared to the fibro glandular region and the tumor is detected. Finally, tumor in a realistic breast tissue model problem is solved. Class II, III and IV type real breast models are used for simulations. According to these simulations, Doppler signal level changes when tumor exists and by the help of this difference in signal level, tumor can be detected. Simulations are repeated for different vibration frequencies between 15 Hz and 30 Hz.

CHAPTER 5

CONCLUSIONS AND FUTURE WORK

In this thesis, simulation studies about the Harmonic Motion Microwave Doppler Imaging (HMMDI) method are performed. According to the HMMDI method, tumor in breast tissue can be found by using both electrical and mechanical properties of the tissues. By using this idea, a setup is introduced. The setup includes two waveguide antennas, focused ultrasound and a tissue model. Transmitter antenna applies electromagnetic waves and at the same time focused ultrasound induces vibration in the tissue. Vibration changes the phase and amplitude of the signal received from the receiver antenna. The data is analyzed to detect the presence and location of a tumor in the tissue.

For simulations, electrical and mechanical 3-D FDTD algorithms were used. Initially, a mechanical FDTD code was implemented in Matlab. A simulation domain was defined and the displacement values at the center of the tumor were calculated. The same simulations were also made using COMSOL Multiphysics program. The solution of the developed code was verified by comparing its results with the COMSOL results. The simulation results showed that in the tumor region displacement values decrease compared to the normal tissue because tumor is stiffer than the breast tissue (i.e., the Young Modulus of the tumor is greater than that of the normal breast tissue). Furthermore, different source frequencies between 15 Hz and 30 Hz were used in the mechanical simulations. According to these simulations, increasing frequency decreases the displacement values, as expected.

Secondly, electromagnetic problem was studied. Electromagnetic 3-D FDTD equations were implemented. To prevent the reflections at the boundaries, the CPML method was implemented to the 3-D FDTD equations. Then, in order to show the

effect of vibrations around tumor cells, sub-cell method was implemented to the same equations. To conclude, the solution method for the forward problem of the HMMDI method was introduced. This method was solved with combination of the electromagnetic and mechanical solutions.

One important problem of the simulation for the HMMDI method is the computation time since the electromagnetic and mechanical simulations works with thousands of iterations. In this thesis, some acceleration methods were implemented. These methods need software and hardware implementations. GPU card with workstation shows the fastest result as the hardware. By the help of *arrayfun* and *parfor* command in Matlab, effective accelerations were provided. Matlab programming language was preferred because mathematical simulations for HMMDI method are easy to implement with this language. On the other hand, better accelerations can be achieved with other programming languages.

Tests were performed on different tissue types to understand the effectiveness of the method. Firstly, tumor in homogenous breast fat was studied. Tumor was detected in y axis and z axis scanning. Doppler signal amplitude increases at the tumor region. Secondly, tumor was placed in the fibro-glandular tissue. Fibro-glandular tissue and tumor have similar electrical properties, therefore it is difficult problem to detect the tumor when it is in the fibro glandular tissue. Because of the fact that tumor is stiffer than fibro glandular, the received Doppler signal varies between tumor and fibro-glandular tissue. At the tumor region, Doppler signal level decreased compared to the fibro glandular region and tumor was detected. Finally, realistic tissue models were used. Tissue models were taken from the UWCEM phantom library. The simulations were done by analyzing two cases; when tumor is absent, and when a tumor exists in the breast model. When tumor exists, Doppler signal level change in the tumor region and the tumor can be detected for different frequencies. All these examples show the effectiveness of the HMMDI method.

In this thesis, implementation of the HMMDI was tested for various type of tissues and acceleration methods for the computation were suggested. To improve the capability of the method, following points should be investigated in the future. The work list is as follows:

- Make 3-D scanning of the tissue models
- To understand the effects of dielectric changes on the Doppler signals
- Developing reconstruction algorithms to precisely define the location and shape of the tumor
- Implementation of the parallel programming algorithms in other programming languages.

REFERENCES

- [1] (2019), Worldwide Cancer Data. Available online.
<https://www.wcrf.org/dietandcancer/cancer-trends/worldwide-cancer-data>
- [2] (2019), Anatomy of the Breasts. Available online.
<https://www.stanfordchildrens.org/en/topic/default?id=anatomy-of-the-breasts-85-P00132>
- [3] E. J. Son, K. K. Oh, E. K. Kim, " Pregnancy-Associated Breast Disease: Radiologic Features and Diagnostic Dilemmas," *Yonsei Medical Journal*, vol. 47, no. 1, pp. 34-42, 2006.
- [4] P. M. Meaney, M. W. Fanning, D. Li, S. P. Poplack and K. D. Paulsen, "A Clinical Prototype for Active Microwave Imaging of the Breast," *IEEE Transactions on Microwave Theory and Techniques*, vol. 49, no. 11, pp. 1842-1853, November 2000.
- [5] Mojtaba Fallahpour, "Synthetic Aperture Radar-Based Techniques and Reconfigurable Antenna Design for Microwave Imaging of Layered Structures," PhD. Thesis, Dept. of Electrical Engineering, Missouri University of Science and Technology, 2013.
- [6] M. Lazebnik, D. Popovic, L. McCarthey, C. b Watkins, M. J Lindstrom, J. Harter, S. Sewall, T. Ogilvie, A. Magliocco, T. M. Breslin, W. Temple, D. Mew, J. H Booske, M. Okoniewski and S. C Hagness, "A large-scale study of the ultrawideband microwave dielectric properties of normal, benign and malignant breast tissues obtained from cancer surgeries," *Physics in Medicine and Biology*, 52, pp. 6093-6115, October 2007.
- [7] M. Fatemi, A. Manduca, J. F. Greenleaf, "Imaging Elastic Properties of Biological Tissues by Low-Frequency Harmonic Motion," *Proceedings of the IEEE*, vol. 91, no. 10, October 2003.
- [8] Kathryn R. Nightingale, Mark L. Palmeri, Roger W. Nightingale, and Gregg E. Trahey , "On The Feasibility of Remote Palpation Using Acoustic Radiation Force," *The Journal of the Acoustical Society of America*, pp. 625-634, July 2001.
- [9] A. Samani, J. Zubovits, and D. Plewes, "Elastic Moduli Of Normal And Pathological Human Breast Tissues: An Inversion-Technique-Based Investigation Of 169 Samples," *Physics in Medicine and Biology*, pp. 1565-1576, 2007.
- [10] C. B. Top, "Harmonic Motion Microwave Doppler Imaging Method," *PhD. Thesis*, Dept. of Electrical and Electronics Engineering, Middle East Technical University, 2013.

- [11] C. B. Top, N. G. Gençer, "Simulation of the Scattered Field From a Vibrating Tumor Inside the Tissue Using 3D-FDTD Method," *IEEE Microwave and Wireless Components Letters*, vol. 23, no. 6, pp. 273-275, June 2013.
- [12] Linda Woodard, "Introduction to Parallel Programming," *Lecture Notes*, Center for Advance Computing, Cornell University, 2013.
- [13] (2019), What's the Difference Between CPU and GPU. Available online. <https://blogs.nvidia.com/blog/2009/12/16/whats-the-difference-between-a-cpu-and-a-gpu/>
- [14] Top, C.B., Gençer, N.G, Hybrid Mechanical-Electromagnetic Imaging Method and the system Thereof, 2012.
- [15] A. K. Tafreshi, "Design and Realization of a Hybrid Medical imaging System: Harmonic Motion Microwave Doppler Imaging," PhD. Thesis, Dept. of Electrical and Electronics Engineering, Middle East Technical University, February 2016.
- [16] C. B. Top, A. K. Tafreshi, N. G. Gençer, "Microwave Sensing of Acoustically Induced Local Harmonic Motion: Experimental and Simulation Studies on Breast Tumor Detection," *IEEE Transactions on Microwave Theory and Techniques*, vol. 64, no. 11, November 2016.
- [17] Fatemi, M. and J.F. Greenleaf, "Vibro-Acoustography: An Imaging Modality Based On Ultrasound-Stimulated Acoustic Emission," *Proceedings of the National Academy of Sciences of the United States of America*, vol. 96, pp. 6603-6608, June 1999.
- [18] E. E. Konofagou, M. Ottensmeyer, S. Agabian, S. L. Dawson, K. Hynynen, "Estimating Localized Oscillatory Tissue Motion for Assessment of the Underlying Mechanical Modulus," *Ultrasonics*, pp. 951-956, 2004.
- [19] L. Tsang, , J.A. Kong, K.H. Ding, C. O. Ao, "Scattering Of Electromagnetic Waves:Theories and Applications," John Wiley & Sons, Inc., 2000.
- [20] K. Yomogida, J. T. Etgen, "3-D Wave Propagation in the Los Angeles Basin for the Whittier-Narrows Earthquake", *Bulletin Seismological Society of America*, vol. 83, no. 5, pp.1325-1344., Oct. 1993.
- [21] J. Virieux, "P-SV wave propagation in heterogeneous media: Velocity-stress finite-difference method," *Geophysics*, vol. 51, no. 4, pp. 889-901, April 1986.
- [22] "The Finite Difference Time Domain Method," *Lecture Notes*, Dept. of Electrical and Computer Engineering, Utah University, 2014.
- [23] D. M. Sullivan, "Electromagnetic Simulation Using the FDTD Method," *IEEE Press*, QC760. S92, pp.79-80, 2000.

- [24] J. A. Roden, S. D. Gedney, "Convolutional PML (CPML): An Efficient FDTD Implementation of the CFS-PML for Arbitrary Media," *Microwave Optical Tech. Lett.*, vol. 27, pp. 334–339, 2000.
- [25] Branko Gvodzic, Dusan Durdevic, Nebojsa Raicevic, " CPML Parameter Optimization in FDTD Modeling of Impulsive Source," *Automatic Control and Robotics*, vol. 16, no. 3, pp. 229-240, July 2017.
- [26] (2019), Finite Difference Time Domain Modeller. Available online. <http://fab.cba.mit.edu/classes/862.06/students/kwan/existing.html>
- [27] J. G. Maloney and G. S. Smith, "The Efficient Modeling of Thin Material Sheets in The Finite-Difference Time-Domain (FDTD) Method," *IEEE Transactions on Antennas and Propagation*, AP- 40, 3, pp. 323-330, 1990.
- [28] B. Barney, "Introduction to Parallel Programming," *Tutorials*, Lawrence Livermore National Laboratory.
- [29] (2019), Vectorization. Available online. http://www.mathworks.com/help/matlab/matlab_prog/vectorization.html
- [30] (2019), Nvidia Tesla K20 Datasheet. Available online. <https://media.dustin.eu/media/114620/nvidia-tesla-k20-grafikkort.pdf>
- [31] (2019), arrayfun. Available online. <http://www.mathworks.com/help/parallel-computing/gpuarray.arrayfun.html>
- [32] (2013), Food and Drug Administration, "HIFU Simulator," <http://www.fda.gov/aboutfda/centersoffices/officeofmedicalproductsandtobacco/cdrh/cdrhoffices/ucm301529.htm>
- [33] (2019), Phantom Repository. Available online. <http://uwcem.ece.wisc.edu/phantomRepository.html>
- [34] American College of Radiology, "Illustrated Breast Imaging Reporting and Data System (BI-RADS)," *American College of Radiology*, third edition, 1998.

APPENDICES

A. Equations of Electromagnetic 3-D FDTD

Maxwell equations are as follows:

$$-\mu \frac{\partial H}{\partial t} = \nabla \times E = \begin{vmatrix} \widehat{a}_x & \widehat{a}_y & \widehat{a}_z \\ \frac{\partial}{\partial x} & \frac{\partial}{\partial y} & \frac{\partial}{\partial z} \\ E_x & E_y & E_z \end{vmatrix} \quad 6-1$$

$$\sigma E + \epsilon \frac{\partial E}{\partial t} = \nabla \times H = \begin{vmatrix} \widehat{a}_x & \widehat{a}_y & \widehat{a}_z \\ \frac{\partial}{\partial x} & \frac{\partial}{\partial y} & \frac{\partial}{\partial z} \\ H_x & H_y & H_z \end{vmatrix} \quad 6-2$$

The parameters used in the Maxwell equations are given in Table 6.1.

Table 6.1. *Parameters of the Maxwell equations*

H	Magnetic field
E	Electric field
ϵ	Permittivity
μ	Permeability
σ	Conductivity

After the cross product is applied to E and H fields, the equations are calculated at the evaluation points in Yee grid (Figure 2.5) as follows:

$$-\mu \frac{\partial H_x}{\partial t} = \frac{\partial E_z}{\partial y} - \frac{\partial E_y}{\partial z} \Bigg|_{x=m\Delta_x, y=(n+1/2)\Delta_y, z=(p+1/2)\Delta_z, t=q\Delta_t} \quad 6-3$$

$$-\mu \frac{\partial H_y}{\partial t} = \frac{\partial E_x}{\partial z} - \frac{\partial E_z}{\partial x} \Bigg|_{x=(m+1/2)\Delta_x, y=n\Delta_y, z=(p+1/2)\Delta_z, t=q\Delta_t} \quad 6-4$$

$$-\mu \frac{\partial H_z}{\partial t} = \frac{\partial E_y}{\partial x} - \frac{\partial E_x}{\partial y} \Bigg|_{x=(m+1/2)\Delta_x, y=(n+1/2)\Delta_y, z=p\Delta_z, t=q\Delta_t} \quad 6-5$$

$$\sigma E_x + \frac{\partial E_x}{\partial t} = \frac{\partial H_z}{\partial y} - \frac{\partial H_y}{\partial z} \Big|_{x=(m+1/2)\Delta_x, y=n\Delta_y, z=p\Delta_z, t=(q+1/2)\Delta_t} \quad 6-6$$

$$\sigma E_y + \frac{\partial E_y}{\partial t} = \frac{\partial H_x}{\partial z} - \frac{\partial H_z}{\partial x} \Big|_{x=m\Delta_x, y=(n+1/2)\Delta_y, z=p\Delta_z, t=(q+1/2)\Delta_t} \quad 6-7$$

$$\sigma E_z + \frac{\partial E_z}{\partial t} = \frac{\partial H_y}{\partial x} - \frac{\partial H_x}{\partial y} \Big|_{x=m\Delta_x, y=n\Delta_y, z=(p+1/2)\Delta_z, t=(q+1/2)\Delta_t} \quad 6-8$$

These equations can be written in discrete form as follows:

$$\begin{aligned} H_x^{q+\frac{1}{2}} \left[m, n + \frac{1}{2}, p + \frac{1}{2} \right] &= \frac{1 - \frac{\sigma\Delta t}{2\mu}}{1 + \frac{\sigma\Delta t}{2\mu}} H_x^{q-\frac{1}{2}} \left[m, n + \frac{1}{2}, p + \frac{1}{2} \right] \\ &+ \frac{1}{1 + \frac{\sigma\Delta t}{2\mu}} \left\{ \frac{\Delta t}{\mu\Delta z} \left\{ E_y^q \left[m, n + \frac{1}{2}, p + 1 \right] \right. \right. \\ &\quad \left. \left. - E_y^q \left[m, n + \frac{1}{2}, p \right] \right\} \right. \\ &\quad \left. - \frac{\Delta t}{\mu\Delta y} \left\{ E_z^q \left[m, n + 1, p + \frac{1}{2} \right] - E_z^q \left[m, n, p + \frac{1}{2} \right] \right\} \right\} \end{aligned} \quad 6-9$$

$$\begin{aligned} H_y^{q+\frac{1}{2}} \left[m + \frac{1}{2}, n, p + \frac{1}{2} \right] &= \frac{1 - \frac{\sigma\Delta t}{2\mu}}{1 + \frac{\sigma\Delta t}{2\mu}} H_y^{q-\frac{1}{2}} \left[m + \frac{1}{2}, n, p + \frac{1}{2} \right] \\ &+ \frac{1}{1 + \frac{\sigma\Delta t}{2\mu}} \left\{ \frac{\Delta t}{\mu\Delta x} \left\{ E_z^q \left[m + 1, n, p + \frac{1}{2} \right] \right. \right. \\ &\quad \left. \left. - E_z^q \left[m, n, p + \frac{1}{2} \right] \right\} \right. \\ &\quad \left. - \frac{\Delta t}{\mu\Delta z} \left\{ E_x^q \left[m + \frac{1}{2}, n, p + 1 \right] - E_x^q \left[m + \frac{1}{2}, n, p \right] \right\} \right\} \end{aligned} \quad 6-10$$

$$\begin{aligned}
& H_z^{q+\frac{1}{2}} \left[m + \frac{1}{2}, n + \frac{1}{2}, p \right] \\
&= \frac{1 - \frac{\sigma\Delta t}{2\mu}}{1 + \frac{\sigma\Delta t}{2\mu}} H_z^{q-\frac{1}{2}} \left[m + \frac{1}{2}, n + \frac{1}{2}, p \right] \\
&+ \frac{1}{1 + \frac{\sigma\Delta t}{2\mu}} \left\{ \frac{\Delta t}{\mu\Delta y} \left\{ E_x^q \left[m + \frac{1}{2}, n + 1, p \right] \right. \right. \\
&- E_x^q \left[m + \frac{1}{2}, n, p \right] \left. \right\} \\
&- \frac{\Delta t}{\mu\Delta x} \left\{ E_y^q \left[m + 1, n + \frac{1}{2}, p \right] - E_y^q \left[m, n + \frac{1}{2}, p \right] \right\} \Big\}
\end{aligned} \tag{6-11}$$

$$\begin{aligned}
& E_x^{q+1} \left[m + \frac{1}{2}, n, p \right] \\
&= \frac{1 - \frac{\sigma\Delta t}{2\epsilon}}{1 + \frac{\sigma\Delta t}{2\epsilon}} E_x^q \left[m + \frac{1}{2}, n, p \right] \\
&+ \frac{1}{1 + \frac{\sigma\Delta t}{2\epsilon}} \left\{ \frac{\Delta t}{\epsilon\Delta y} \left\{ H_z^{q+\frac{1}{2}} \left[m + \frac{1}{2}, n + \frac{1}{2}, p \right] \right. \right. \\
&- H_z^{q+\frac{1}{2}} \left[m + \frac{1}{2}, n - \frac{1}{2}, p \right] \left. \right\} \\
&- \frac{\Delta t}{\epsilon\Delta z} \left\{ H_y^{q+\frac{1}{2}} \left[m + \frac{1}{2}, n, p + \frac{1}{2} \right] \right. \\
&- H_y^{q+\frac{1}{2}} \left[m + \frac{1}{2}, n, p - \frac{1}{2} \right] \left. \right\} \Big\}
\end{aligned} \tag{6-12}$$

$$\begin{aligned}
& E_y^{q+1} \left[m, n + \frac{1}{2}, p \right] \\
&= \frac{1 - \frac{\sigma\Delta t}{2\epsilon}}{1 + \frac{\sigma\Delta t}{2\epsilon}} E_y^q \left[m, n + \frac{1}{2}, p \right] \\
&+ \frac{1}{1 + \frac{\sigma\Delta t}{2\epsilon}} \left\{ \frac{\Delta t}{\epsilon\Delta z} \left\{ H_x^{q+\frac{1}{2}} \left[m, n + \frac{1}{2}, p - \frac{1}{2} \right] \right. \right. \\
&- H_x^{q+\frac{1}{2}} \left[m, n + \frac{1}{2}, p + \frac{1}{2} \right] \left. \right\} \\
&- \frac{\Delta t}{\epsilon\Delta x} \left\{ H_z^{q+\frac{1}{2}} \left[m + \frac{1}{2}, n + \frac{1}{2}, p \right] \right. \\
&- H_z^{q+\frac{1}{2}} \left[m - \frac{1}{2}, n + \frac{1}{2}, p \right] \left. \right\} \Big\}
\end{aligned} \tag{6-13}$$

$$\begin{aligned}
E_z^{q+1} \left[m, n, p + \frac{1}{2} \right] &= \frac{1 - \frac{\sigma \Delta t}{2\epsilon}}{1 + \frac{\sigma \Delta t}{2\epsilon}} E_z^q \left[m, n, p + \frac{1}{2} \right] \\
&+ \frac{1}{1 + \frac{\sigma \Delta t}{2\epsilon}} \left\{ \frac{\Delta t}{\epsilon \Delta x} \left(H_y^{q+\frac{1}{2}} \left[m + \frac{1}{2}, n, p + \frac{1}{2} \right] \right. \right. \\
&- \left. \left. H_y^{q+\frac{1}{2}} \left[m - \frac{1}{2}, n, p + \frac{1}{2} \right] \right) \right. \\
&- \frac{\Delta t}{\epsilon \Delta y} \left(H_x^{q+\frac{1}{2}} \left[m, n + \frac{1}{2}, p + \frac{1}{2} \right] \right. \\
&- \left. \left. H_x^{q+\frac{1}{2}} \left[m, n - \frac{1}{2}, p + \frac{1}{2} \right] \right) \right\}
\end{aligned} \tag{6-14}$$

The parameters used in the 3-D FDTD discrete form equations are given in Table 6.2.

Table 6.2. Parameters of discrete form of the 3-D FDTD equations

H_x, H_y, H_z	Magnetic fields in x, y, z planes
E	Electric fields in x, y, z planes
m, n, p	Numbers of the subspace parts in the x, y, z planes
q	Time parameter
$\Delta x, \Delta y, \Delta z$	Displacement in x, y, z planes
Δt	Change in time
ϵ	Permittivity
μ	Permeability
σ	Conductivity

B. CPML Equations

CPML method equations are as follows:

$$\begin{aligned}
 \psi_{y,z}^{E^{q+\frac{1}{2}}}\left(m, n + \frac{1}{2}, p + \frac{1}{2}\right) & \\
 &= b_y \psi_{y,z}^{E^{q-\frac{1}{2}}}\left(m, n + \frac{1}{2}, p + \frac{1}{2}\right) \\
 &\quad - c_y \left(\frac{E_z^{q+\frac{1}{2}}\left(m, n + 1, k + \frac{1}{2}\right) - E_z^{q+\frac{1}{2}}\left(m, n, k + \frac{1}{2}\right)}{\Delta y} \right)
 \end{aligned} \tag{6-15}$$

$$\begin{aligned}
 \psi_{z,y}^{E^{q+\frac{1}{2}}}\left(m, n + \frac{1}{2}, p + \frac{1}{2}\right) & \\
 &= b_z \psi_{y,z}^{E^{q-\frac{1}{2}}}\left(m, n + \frac{1}{2}, p + \frac{1}{2}\right) \\
 &\quad - c_z \left(\frac{E_y^{q+\frac{1}{2}}\left(m, n + \frac{1}{2}, k + 1\right) - E_y^{q+\frac{1}{2}}\left(m, n + \frac{1}{2}, k\right)}{\Delta z} \right)
 \end{aligned} \tag{6-16}$$

$$\begin{aligned}
 \psi_{z,x}^{E^{q+\frac{1}{2}}}\left(m + \frac{1}{2}, n, p + \frac{1}{2}\right) & \\
 &= b_z \psi_{z,x}^{E^{q-\frac{1}{2}}}\left(m + \frac{1}{2}, n, p + \frac{1}{2}\right) \\
 &\quad - c_z \left(\frac{E_x^{q+\frac{1}{2}}\left(m + \frac{1}{2}, n, p + 1\right) - E_x^{q+\frac{1}{2}}\left(m + \frac{1}{2}, n, p\right)}{\Delta z} \right)
 \end{aligned} \tag{6-17}$$

$$\begin{aligned}
 \psi_{x,z}^{E^{q+\frac{1}{2}}}\left(m + \frac{1}{2}, n, p + \frac{1}{2}\right) & \\
 &= b_x \psi_{x,z}^{E^{q-\frac{1}{2}}}\left(m + \frac{1}{2}, n, p + \frac{1}{2}\right) \\
 &\quad - c_x \left(\frac{E_z^{q+\frac{1}{2}}\left(m + 1, n, p + \frac{1}{2}\right) - E_z^{q+\frac{1}{2}}\left(m, n, p + \frac{1}{2}\right)}{\Delta x} \right)
 \end{aligned} \tag{6-18}$$

$$\begin{aligned}
\psi_{x,y}^{E^{q+\frac{1}{2}}}\left(m+\frac{1}{2},n+\frac{1}{2},p\right) & \quad 6-19 \\
&= b_x \psi_{x,y}^{E^{q-\frac{1}{2}}}\left(m+\frac{1}{2},n+\frac{1}{2},p\right) \\
&\quad - c_x \left(\frac{E_y^{q+\frac{1}{2}}\left(m+1,n+\frac{1}{2},p\right) - E_y^{q+\frac{1}{2}}\left(m,n+\frac{1}{2},p\right)}{\Delta x} \right)
\end{aligned}$$

$$\begin{aligned}
\psi_{y,x}^{E^{q+\frac{1}{2}}}\left(m+\frac{1}{2},n+\frac{1}{2},p\right) & \quad 6-20 \\
&= b_y \psi_{y,x}^{E^{q-\frac{1}{2}}}\left(m+\frac{1}{2},n+\frac{1}{2},p\right) \\
&\quad - c_y \left(\frac{E_x^{q+\frac{1}{2}}\left(m+\frac{1}{2},n+1,p\right) - E_x^{q+\frac{1}{2}}\left(m+\frac{1}{2},n,p\right)}{\Delta y} \right)
\end{aligned}$$

$$\begin{aligned}
\psi_{y,z}^{H^q}\left(m+\frac{1}{2},n,p\right) & \quad 6-21 \\
&= b_y \psi_{y,z}^{H^{q-1}}\left(m+\frac{1}{2},n,p\right) \\
&\quad - c_y \left(\frac{H_z^q\left(m+\frac{1}{2},n+\frac{1}{2},p\right) - H_z^q\left(m+\frac{1}{2},n-\frac{1}{2},p\right)}{\Delta y} \right)
\end{aligned}$$

$$\begin{aligned}
\psi_{z,y}^{H^q}\left(m+\frac{1}{2},n,p\right) & \quad 6-22 \\
&= b_y \psi_{z,y}^{H^{q-1}}\left(m+\frac{1}{2},n,p\right) \\
&\quad - c_z \left(\frac{H_y^q\left(m+\frac{1}{2},n,p+\frac{1}{2}\right) - H_y^q\left(m+\frac{1}{2},n,p-\frac{1}{2}\right)}{\Delta z} \right)
\end{aligned}$$

$$\begin{aligned}
\psi_{z,x}^{H^q}\left(m,n+\frac{1}{2},p\right) & \quad 6-23 \\
&= b_z \psi_{z,x}^{H^{q-1}}\left(m,n+\frac{1}{2},p\right) \\
&\quad - c_z \left(\frac{H_x^q\left(m,n+\frac{1}{2},p+\frac{1}{2}\right) - H_x^q\left(m,n+\frac{1}{2},p-\frac{1}{2}\right)}{\Delta z} \right)
\end{aligned}$$

$$\begin{aligned}
\psi_{x,z}^{H^q} \left(m, n + \frac{1}{2}, p \right) &= b_x \psi_{x,z}^{H^{q-1}} \left(m, n + \frac{1}{2}, p \right) \\
&\quad - c_x \left(\frac{H_z^q \left(m + \frac{1}{2}, n + \frac{1}{2}, p \right) - H_z^q \left(m - \frac{1}{2}, n + \frac{1}{2}, p \right)}{\Delta x} \right)
\end{aligned} \tag{6-24}$$

$$\begin{aligned}
\psi_{x,y}^{H^q} \left(m, n, p + \frac{1}{2} \right) &= b_x \psi_{x,y}^{H^{q-1}} \left(m, n, p + \frac{1}{2} \right) \\
&\quad - c_x \left(\frac{H_y^q \left(m + \frac{1}{2}, n, p + \frac{1}{2} \right) - H_y^q \left(m - \frac{1}{2}, n, p + \frac{1}{2} \right)}{\Delta x} \right)
\end{aligned} \tag{6-25}$$

$$\begin{aligned}
\psi_{y,x}^{H^q} \left(m, n, p + \frac{1}{2} \right) &= b_y \psi_{y,x}^{H^{q-1}} \left(m, n, p + \frac{1}{2} \right) \\
&\quad - c_x \left(\frac{H_y^q \left(m, n + \frac{1}{2}, p + \frac{1}{2} \right) - H_y^q \left(m, n - \frac{1}{2}, p + \frac{1}{2} \right)}{\Delta y} \right)
\end{aligned} \tag{6-26}$$

where $b = e^{-\frac{\Delta t}{\tau}}$ and $c = \frac{\sigma_y}{K_y} \frac{1}{(K_y a_y + \sigma_y)} (1 - e^{-\frac{\Delta t}{\tau}})$

$$E(m, n, p) = E(m, n, p) + \frac{\Delta t}{\epsilon} \psi^E(m, n, p) \tag{6-27}$$

$$H(m, n, p) = H(m, n, p) + \frac{\Delta t}{\mu} \psi^H(m, n, p) \tag{6-28}$$

The parameters used in the CPML equations are given in Table 6.3.

Table 6.3. *Parameters of the CPML equations*

ψ	Auxiliary expression
H	Magnetic field
E	Electric field
m, n, p	Numbers of the subspace parts in the x, y, z planes
q	Time parameter
$\Delta x, \Delta y, \Delta z$	Displacement in x, y, z planes
Δt	Change in time
ϵ	Permittivity
μ	Permeability
σ, K, a	Stretching variable parameters